

ANALYSIS OF TITAN'S NEUTRAL UPPER ATMOSPHERE
FROM CASSINI ION NEUTRAL MASS SPECTROMETER
MEASUREMENTS IN THE CLOSED SOURCE NEUTRAL MODE

by

Jun Cui

A Dissertation Submitted to the Faculty of the

DEPARTMENT OF ASTRONOMY

In Partial Fulfillment of the Requirements
For the Degree of

DOCTOR OF PHILOSOPHY

In the Graduate College

THE UNIVERSITY OF ARIZONA

2 0 0 8

THE UNIVERSITY OF ARIZONA
GRADUATE COLLEGE

As members of the Final Examination Committee, we certify that we have read the dissertation prepared by Jun Cui entitled Analysis of Titan's Neutral Upper Atmosphere from Cassini Ion Neutral Mass Spectrometer Measurements in the Closed Source Neutral Mode and recommend that it be accepted as fulfilling the dissertation requirement for the Degree of Doctor of Philosophy.

Roger V. Yelle

Date: 21 April 2008

Alex Pavolov

Date: 21 April 2008

Robert H. Brown

Date: 21 April 2008

Lucy Ziurys

Date: 21 April 2008

John Biegging

Date: 21 April 2008

Final approval and acceptance of this dissertation is contingent upon the candidate's submission of the final copies of the dissertation to the Graduate College.

I hereby certify that I have read this dissertation prepared under my direction and recommend that it be accepted as fulfilling the dissertation requirement.

Dissertation Director: Roger V. Yelle

Date: 21 April 2008

STATEMENT BY AUTHOR

This dissertation has been submitted in partial fulfillment of requirements for an advanced degree at The University of Arizona and is deposited in the University Library to be made available to borrowers under rules of the Library.

Brief quotations from this dissertation are allowable without special permission, provided that accurate acknowledgment of source is made. Requests for permission for extended quotation from or reproduction of this manuscript in whole or in part may be granted by the head of the major department or the Dean of the Graduate College when in his or her judgment the proposed use of the material is in the interests of scholarship. In all other instances, however, permission must be obtained from the author.

SIGNED: _____ Jun Cui

ACKNOWLEDGEMENTS

There are lots of people I would like to thank for a huge variety of reasons.

It is difficult to overstate my gratitude to my Ph.D. supervisor, Dr. Roger V. Yelle, Professor of Planetary Sciences at the Lunar and Planetary Laboratory of University of Arizona. With his enthusiasm, his creativity and inspiration, and his great efforts to explain things clearly and simply, he helped to make scientific research fun for me. I would certainly have been lost without him.

I would like to thank those people with whom I have maintained a long-term collaboration, especially Veronique Vuitton, who is a postdoc research scientist at the Lunar and Planetary Laboratory of University of Arizona, and Ingo C.F. Müller-Wodarg, who is a faculty at the Space and Atmospheric Physics Group at Imperial College London. During the past two years of my PhD research, I benefit greatly from their expertise of photochemistry and dynamics in planetary upper atmospheres. I am also indebted to other members of my research group, including Sarah Hörst, Panayotis Lavvas and Nikole Lewis.

I wish to thank many people at the Southwest Research Institute and Goddard Space Flight Center, including J. H. Waite, Jr., W. T. Kasprzak, H. B. Niemann, D. Gell, E. L. Patrick, E. Raaen, G. Fletcher and B. Magee. Without their efforts in the post-launch instrument calibration as well as helps with data analysis, it is not possible for me to complete this thesis. I am also indebted to Dr. Darrel Strobel at the Dept. of Earth & Planetary Sciences of Johns Hopkins University and Dr. Roland Thissen at the Laboratoire de Planetologie de Grenoble at Université Joseph Fourier for useful discussions on planetary aeronomy and mass spectrometry.

I am grateful to Dr. Xiaohui Fan, Dr. Ann Zabludoff, Dr. Robert C. Kennicutt, Jr., and the secretaries at both Steward Observatory and Lunar & Planetary Laboratory, for helping me get through the difficult times. I also wish to thank many graduate students at these two departments for all their emotional supports, including Yong Shi, Lei Bai, Amelia M. Stutz, Janice C. Lee, Linhua Jiang, Katherine Volk, Martin Pessah, Andrew R. Marble, Yuan Lian and many others.

Lastly, I wish to thank my parents, J.-W. Cui and Z.-Q. Xu, my wife, Lynn Hsia, and my son, Matthew Y. Cui. They have lost a lot due to my research abroad. Without their encouragement and understanding it would have been impossible for me to finish my PhD thesis.

DEDICATION

*For my family, who offered me unconditional love and support throughout the
course of this thesis.*

TABLE OF CONTENTS

LIST OF FIGURES	8
LIST OF TABLES	18
ABSTRACT	20
CHAPTER 1 INTRODUCTION	22
CHAPTER 2 INSTRUMENTATION AND OBSERVATION	25
CHAPTER 3 DATA CALIBRATION	29
3.1 Sensitivities	29
3.1.1 Corrections for terrestrial isotope ratios	30
3.1.2 Calibrations of peak sensitivities between flight unit (FU) and refurbished engineering unit (REU)	32
3.1.3 Cracking patterns	37
3.2 Ram pressure enhancement	40
3.3 Saturations	41
3.4 Thruster firings	44
3.5 Subtraction of background counts	45
3.5.1 Empirical background model	45
3.5.2 Residual gas in the INMS chamber	50
3.6 Channel crosstalk	51
CHAPTER 4 SINGULAR VALUE DECOMPOSITION OF THE NEUTRAL MASS SPECTRA	54
4.1 Basic algorithm	54
4.2 Corrections for negative densities	58
4.3 Major neutral species and their isotopes	60
4.3.1 Nitrogen	60
4.3.2 Methane	61
4.4 Identification of neutral constituents	64
4.5 Error analysis	67

TABLE OF CONTENTS – *Continued*

CHAPTER 5	NEUTRAL GAS DISTRIBUTION IN TITAN'S THERMO- SPHERE	69
5.1	Wall effects	70
5.2	Globally averaged vertical distribution	84
5.2.1	Nitrogen, methane and hydrogen	84
5.2.2	Isotope ratios	89
5.2.3	Minor species	94
5.2.4	Comparison with previous results	102
5.3	Horizontal and diurnal variations	107
5.3.1	Meridional variations	111
5.3.2	Zonal variations	114
5.3.3	Diurnal variations	116
5.3.4	Horizontal/diurnal variations of heavy species	117
5.3.5	Reliability check of the observed horizontal/diurnal variations	122
CHAPTER 6	DISTRIBUTION OF MOLECULAR HYDROGEN IN TITAN'S EXOSPHERE	131
6.1	Preliminary model of H ₂ distribution in Titan's exosphere	133
6.2	Thermal effect and external loss processes of H ₂	135
6.2.1	Temperature decrement for H ₂ near Titan's exobase	135
6.2.2	External loss of H ₂ in Titan's exosphere	141
6.3	Escape of H ₂ on Titan	146
6.3.1	Saturn's gravitational influence	147
6.3.2	Effect of diffusive motion	148
6.3.3	Non-Maxwellian feature of the velocity distribution function	149
CHAPTER 7	CONCLUDING REMARKS	156
APPENDIX A	Energy density and flux in the 13-moment approximation	162
REFERENCES	165

LIST OF FIGURES

2.1	The distribution of the INMS sample adopted in this work, with respect to latitude, longitude, local solar time, as well as altitude. The sample is exclusively for solar minimum conditions, and preferentially selects measurements made over Titan's northern hemisphere and the facing-Saturn side. The open histograms represent the sampling of abundant species including N_2 and CH_4 , extending from 950 km to 1,500 km. The filled histograms represent the sampling of other minor species (multiplied by a factor of 5), which is restricted to altitudes below 1,200 km.	26
3.1	Upper panel: The difference between the FU and REU peak sensitivities shown as a function of peak M/Z . All FU/REU measurements can be roughly fitted with a linear relation. Lower panel: The REU peak sensitivities as a function of peak M/Z . The solid line represents the offset, $S_{FU} - S_{REU}$ that needs to be applied to get the corresponding FU values. For several heavy neutral species (C_4H_6 , C_2H_3CN , C_6H_6 and C_7H_8), the required offsets are comparable with or greater than the measured REU sensitivities.	33
3.2	The relation between the FU and REU peak sensitivities, unscaled (panel a), scaled by the cross section for electron impact ionization (panel b), or scaled by the peak M/Z (panel c). Except for panel c, isotopes of Kr appear to be outliers. The solid lines are obtained by a linear fitting to the FU and REU measurements, including all species for panel c but excluding Kr for panels a and b. The best-fit relation shown in panel c is given by Eqn. 3.23 in the text.	35
3.3	The relation between the REU and FU branching ratios for N_2 , CH_4 , ^{40}Ar , C_2H_2 and C_2H_4 . Isotopes are not included. The solid line shows the best-fit log-linear relation, given by Eqn. 3.24. The corrections from the REU to FU branching ratios are relatively small, ranging between 0.5% and 7%.	37

LIST OF FIGURES – *Continued*

- 3.4 N_2 and CH_4 density profiles (for the inbound T32 measurements) as a function of altitude, determined from counts in different channels. The solid circles represent densities determined from counts in the main channel (28 for N_2 and 16 for CH_4), while the plus signs represent those from counts in a secondary channel (14 for N_2 and 12 for CH_4). The CH_4 densities can also be estimated from channels 13 and 15, which are not shown here. The open diamonds are densities determined from the secondary channels, scaled to maintain agreement with the peak channels. 39
- 3.5 The INMS instrument response in the CSN mode (the ram enhancement factor), as a function of angle of attack, i.e. the angle between the aperture normal and the spacecraft velocity vector. Several species with different molecular masses are shown, assuming a spacecraft velocity of 6 km s^{-1} , a temperature of 150 K in the ambient atmosphere, and a chamber wall temperature of 300 K. The instrument response increases with molecular mass and varies approximately as the cosine of the angle of attack. 41
- 3.6 The count rates (counts s^{-1}) in channels 14 and 28 as a function of altitude, adopted from the INMS measurements made during the inbound T32 flyby. Solid triangles and circles represent data recorded at the $\text{C}^{(1)}$ counter, while plus signs and asterisks data recorded at the $\text{C}^{(2)}$ counter. The $\text{C}^{(1)}$ count rates are saturated at altitudes below $\sim 1,200 \text{ km}$ for channel 28 and below $\sim 1,020 \text{ km}$ for channel 14. The $\text{C}^{(2)}$ count rates have been multiplied by an appropriate conversion factor of 5372 for channel 28 and 4873 for channel 14, respectively. . . 43
- 3.7 The counts in channel 2 as a function of altitude, for the inbound T30 flyby. Overplotted on the count profile is the information of accumulated thruster operation time on 1 s intervals. Each thruster firing nominally lasts 0.125 s, from which I calculate the total number of thruster firings in each 1 s interval. This number is shown on an arbitrary linear scale, at altitudes that coincide with real measurements made in channel 2. The channel 2 counts rejected from the spectral analysis due to thruster firing contaminations are shown as the open circles, while those uncontaminated are shown as the solid circles. . . 45

LIST OF FIGURES – *Continued*

3.8	The width of the Gaussian kernel, the center and width of the square function for the empirical model fitting of the background mass spectra. Solid and open symbols stand for inbound and outbound, respectively. These parameters appear to be constant with altitude. The mean values, given by the dashed lines, are 14.2 for the width of the Gaussian kernel, 25.7 for the center of the square function, and 12.2 for the width of the square function. These mean values are fixed in the empirical background model fitting.	47
3.9	The constant level (squares) and the height of the square function (five-stars) for the empirical model fitting of the background mass spectra. Solid and open symbols stand for inbound and outbound, respectively. These parameters show strong altitude variations.	47
3.10	The empirical model fitting of the background spectrum for the inbound T16 data at an altitude of 994.7 km. The histogram shows the observed mass spectrum, with the solid line giving the best-fit background model. The model fitting is based on counts in channels not affected by neutral constituents in the ambient atmosphere, represented by the solid circles.	48
3.11	The mean mass spectra obtained between 10,000 km and 20,000 km for the inbound (solid) and outbound (dotted) T18 flyby. These spectra are produced by the residual gases in the INMS chamber, including H ₂ , CH ₄ , H ₂ O, N ₂ , CO and CO ₂ (marked by arrows). The horizontal straight lines indicate the constant background levels, corresponding to the mean values calculated from counts in channels not occupied by residual gases.	50
3.12	The mass spectrum for the N ₂ reference gases used for FU characterization. Only the portion near M/Z~28 is shown. While counts in channels 28 and 29 are clearly associated with N ₂ and ¹⁴ N ¹⁵ N, the residual counts in surrounding channels are interpreted as a result of the crosstalk effect. The minor peak at channel 32 is caused by O ₂ impurities in the calibration chamber.	52

LIST OF FIGURES – *Continued*

- 4.1 The INMS mass spectra averaged between 960 and 980 km for the inbound T30 flyby (upper panel), between 1,100 and 1,200 km for the inbound T28 flyby (middle panel), and between 980 and 1,100 km for the outbound T18 flyby (lower panel). The solid circles give the measurements with 1σ errors due to counting statistics. Instrumental effects have been properly removed. The count rates in channel 27 are not shown since they are excluded in the spectral fitting due to crosstalk. The histograms show the model spectra, which are calculated with calibrated sensitivity values, appropriate ram enhancement factors, and best-fit densities obtained from the SVD algorithm. . . . 56
- 4.2 The INMS mass spectra averaged between 960 and 980 km for the inbound T30 flyby, near mass channels 16 (upper left), 28 (upper right), 40 (lower left) and 50 (lower right). The solid circles give the measurements with 1σ errors due to counting statistics. The histograms with different colors show the model spectra contributed by different neutral components of Titan's upper atmosphere, with the black ones representing the summation. The deviation between model and observation at channels 41 and 42 might be a signature of C_3H_6 on Titan. 57
- 4.3 Parameter space corresponding to the two smallest singular values in the SVD analysis of the inbound T16 spectrum averaged between 960 and 980 km. Different greyscales indicate the number of species with negative densities. The dark strip corresponds to the region of parameter space where all derived densities are positive. The plus sign marks the location of the lowest χ^2 value in the positive density region. 59
- 4.4 Upper panel: the mean density profiles of CH_4 (solid lines) and $^{13}CH_4$ (dashed lines) averaged over all flybys, with contribution from NH_3 ignored. The thin and thick lines give the inbound and outbound profiles separately. Lower panel: the observed $^{12}C/^{13}C$ ratio as a function of time from C/A, ignoring the contribution from NH_3 . Two extreme cases are shown, one for the T5 flyby with the maximum C/A altitude of 1,027 km in my sample, and the other for the T16 flyby with the minimum C/A altitude of 950 km. The solid and dashed lines give the $^{12}C/^{13}C$ ratio adopted for the T5 and T16 flybys in my SVD analysis (see text for details). 62

LIST OF FIGURES – *Continued*

- 5.1 The density profiles of N_2 , CH_4 , H_2 and ^{40}Ar , averaged over all flybys. The inbound (solid) and outbound (dashed) profiles are nearly identical, indicating that the wall effects are negligible for these species. 71
- 5.2 The density profiles of $\text{C}_2\text{H}_2/\text{C}_2\text{H}_4$, C_4H_2 , C_6H_6 , C_2N_2 , HC_3N and $\text{C}_2\text{H}_3\text{CN}$, obtained by averaging over all flybys and treating inbound (solid) and outbound (dashed) measurements separately. Leftward arrows indicate upper limit densities. All species show some signature of enhancement for the outbound legs, indicating that wall effects are important. 72
- 5.3 Density profiles of ^{40}Ar , $\text{CH}_3\text{C}_2\text{H}$, CH_3CN and NH_3 as a function of time from C/A, obtained by averaging over all flybys. Downward arrows are for upper limit densities. The ^{40}Ar profile serves as a reference which is symmetric about C/A. All other species show enhancement for the outbound legs, indicating that wall effects are important. 73
- 5.4 The distribution of t_0 and Δt in the parameter space of adsorption probability (p_{ads}) and desorption time constant ($t_{\text{des}}^{(\text{ref})}$ referred to an N_2 chamber density of 10^{11} cm^{-3}), where t_0 and Δt represent the time shift and width of the shifted Gaussian function used to characterize both the observed and model chamber density profiles. The thick solid lines mark the region where the combination of p_{ads} and $t_{\text{des}}^{(\text{ref})}$ provides reasonable fit to the observed chamber densities, following the simple adsorption/desorption model proposed in the thesis. . . . 77
- 5.5 The simple adsorption/desorption model fitting to the C_4H_2 densities obtained during the T29 flyby, as a function of time from C/A. The solid circles represent the observed C_4H_2 densities in the chamber, and the open triangles the corresponding atmospheric densities calculated with the ram enhancement factor. The solid and dotted lines represent the model density profiles, with the thick ones assuming $p_{\text{ads}} = 0.8$ and $t_{\text{des}} = 150 \text{ s}$ (referred to an N_2 chamber density of 10^{11} cm^{-3}) and the thin ones assuming $p_{\text{ads}} = 0.1$ and the same desorption time constant. 78

LIST OF FIGURES – *Continued*

- 5.6 The regions in the parameter space of adsorption probability and desorption time constant, where the combinations of these two parameters provide reasonable fits to the observed chamber densities, following the simple adsorption/desorption model proposed in the thesis. Different colors stand for different species, and the desorption time constants are given for a reference N_2 chamber density of 10^{11} cm^{-3} . For most species, the values of these parameters are not well constrained by the INMS data. 79
- 5.7 The realistic instrument response function calculated for $\text{C}_2\text{H}_3\text{CN}$ for different flybys and normalized by the ideal ram enhancement factor. The solid and dotted line portions of each curve represent the inbound and outbound passes, respectively. Values of the adsorption probability, p_{ads} and the desorption time constant, t_{des} used in the model calculations are indicated on the figure, where t_{des} is given for a reference N_2 chamber density of 10^{11} cm^{-3} 80
- 5.8 The instrument response as a function of adsorption probability, for several choices of the desorption time constant (all referred to an N_2 chamber density of 10^{11} cm^{-3}). In each panel, the solid and dashed lines represent the instrument response for species with a molecular mass of 30 and 80, respectively. This represents the reasonable mass range for all heavy species included in my spectral analysis. 81
- 5.9 The globally averaged density profiles of N_2 , CH_4 , H_2 and $^{14}\text{N}^{15}\text{N}$, between 950 and 1,500 km. The solid line overplotted on the N_2 observations is the best-fit hydrostatic equilibrium model, with a thermospheric temperature of 154 K. Also shown are the best-fit isothermal diffusion models for CH_4 and H_2 , with a most probable escape flux of $3.0 \times 10^9 \text{ cm}^{-2} \text{ s}^{-1}$ (for CH_4) and $1.3 \times 10^{10} \text{ cm}^{-2} \text{ s}^{-1}$ (for H_2), referred to Titan's surface. The diffusion model for $^{14}\text{N}^{15}\text{N}$ predicts a most probable nitrogen isotope ratio, $^{14}\text{N}/^{15}\text{N}$ of 131.6 ± 0.2 near Titan's surface (see also Fig. 5.11). 86
- 5.10 Diffusion coefficients adopted in this study as a function of altitude between 100 and 1,500 km. The eddy mixing profile, adopted from Yelle *et al.* (2008), is given by the solid line, and the molecular diffusion coefficients are given by the dotted line (for H_2), short-dashed line (for CH_4), long-dashed line (for $^{14}\text{N}^{15}\text{N}$) and dash-dotted line (for $^{13}\text{CH}_4$). The molecular diffusion coefficients for CH_4 , $^{14}\text{N}^{15}\text{N}$ and $^{13}\text{CH}_4$, which are nearly identical, cannot be distinguished on the figure. 87

LIST OF FIGURES – *Continued*

- 5.11 The solid line shows the profile of $^{14}\text{N}/^{15}\text{N}$ isotope ratio as a function of altitude, with a most probable value of 131.6 ± 0.2 near Titan's surface. The temperature profile of Yelle *et al.* (2008) is adopted. The solid circles show the GCMS measurement of 183 ± 5 at 36-41 km (Niemann *et al.* 2005), and the INMS TA measurement of 188^{+14}_{-16} at 1,200 km (Waite *et al.* 2005). 90
- 5.12 Diffusion model calculations of the carbon isotope ratio as a function of altitude, with the drift velocity ratio between $^{13}\text{CH}_4$ and CH_4 (at the exobase) treated as a free parameter. The solid line gives the best-fit model with a ratio of 1.14, and the dotted line corresponds to a ratio of 0.18 appropriate for Jeans escape. Also shown on the figure are the GCMS carbon isotope ratio of 82.3 measured at 6-18 km (Niemann *et al.* 2005), the INMS result of 95.6 obtained at an altitude of 1,200 km based on the TA data (Waite *et al.* 2005) and my result of 93.3 obtained at 1,100-1,200 km based on a much larger INMS sample. 92
- 5.13 The globally averaged mixing ratios of various hydrocarbons and nitriles observed in Titan's upper atmosphere, as a function of altitude between 950 and 1,200 km. These mixing ratios are obtained by averaging over all inbound measurements, assuming ram pressure enhancement only. Leftward arrows indicate 3σ upper limits. 95
- 5.14 The power law fitting to the density distribution of various species in Titan's upper atmosphere, obtained by averaging over all inbound measurements and assuming ram pressure enhancement only. These profiles are used to remove vertical dependence of these species before investigating possible horizontal/diurnal variations (see Chapter 5.3 for details). 98
- 5.15 The globally averaged distribution of $\text{CH}_3\text{C}_2\text{H}$ (upper panel) and HC_3N (lower panel) in Titan's upper atmosphere. The dashed and dotted lines show the mixing ratio profiles averaged over all inbound and outbound measurements (assuming ram pressure enhancement only). The solid lines represent the profiles corrected for adsorption/desorption (see Sec 5.2.3.2 for details). 101

LIST OF FIGURES – *Continued*

- 5.16 Comparison between Cassini/INMS and Voyager/UVS results of the distribution of neutral species in Titan's thermosphere. The open squares represent globally averaged mixing ratios from this work, combining data from 15 Titan flybys. These values are obtained by assuming ram pressure enhancement alone. The mixing ratio profiles for C_2H_2/C_2H_4 and HC_3N which are corrected for wall adsorption/desorption are shown by the dotted lines. The UVS results from Vervack *et al.* (2004) are given by the solid circles with large horizontal error bars, for comparison. Photochemical model calculations from Lavvas *et al.* (2008a, b) are shown with the dashed lines. 104
- 5.17 The barometric model fitting of the N_2 density distribution in Titan's upper atmosphere. Panel (a) shows the model fitting for three latitude bins over the northern hemisphere; panel (b) presents the N_2 distribution for four longitude bins; and panel (c) shows the average N_2 density profiles for the dayside and nightside, respectively. The figure implies that Titan's equatorial regions, magnetospheric ramside, as well as the nightside hemisphere are relatively warmer. . . 109
- 5.18 The average profiles of CH_4 mixing ratio in Titan's upper atmosphere for three latitude bins, defined as 0° - 30° N for the low latitude bin, 30° N- 60° N for the mid latitude bin and 60° N- 90° N for the high latitude bin. The figure shows depletion of CH_4 near the equator and accumulation of CH_4 near the north pole. The meridional variation of H_2 shows a more complicated pattern, with enhanced abundances at mid latitudes. 112
- 5.19 The average profiles of CH_4 and H_2 mixing ratios in Titan's upper atmosphere for four longitude sectors, denoted as the magnetospheric ramside and wakeside, as well as the facing-Saturn side and anti-Saturn side, each spanning a longitude range of 90° . For CH_4 , the figure shows depletion at Titan's ramside and facing-Saturn side, as well as accumulation at the wakeside and anti-Saturn side. The zonal variation of H_2 shows a more complex pattern. 115
- 5.20 The average profiles of CH_4 and H_2 mixing ratios for Titan's dayside and nightside hemispheres. For both species, depletion over the nightside and accumulation over the dayside can be observed. . . . 118

LIST OF FIGURES – *Continued*

- 5.21 The meridional variations of several representative minor species in Titan’s upper atmosphere. All measurements have been scaled to a common altitude of 1,050 km. These scaled mixing ratios are given by the open circles. For comparison, the solid circles represent the directly measured mixing ratios between 1,025 and 1,075 km based on SVD fits. Downward arrows indicate 3σ upper limit measurements. All species, except for ^{40}Ar , show some signature of depletion near polar regions. The mixing ratios presented in the figure are obtained by assuming ram pressure enhancement, and no correction for wall adsorption/desorption is made. 120
- 5.22 The zonal variations of several heavy species in Titan’s upper atmosphere. Drawing conventions are the same as Fig. 5.21. These species show a trend of accumulation toward zero longitude. However, such a feature is likely to be an observational bias caused by wall effects (see Chapter 5.3.5 for details). 121
- 5.23 Upper panel: A comparison between the latitude distribution for Titan’s ramside, wakeside, facing-Saturn side and anti-Saturn side. Both the wakeside and anti-Saturn side are strongly biased toward high latitude regions. Lower panel: the latitude distribution for Titan’s dayside and nightside hemispheres. The dayside sector preferentially selects measurements made near polar regions. 128
- 6.1 The global average H_2 distribution with $\pm 1\sigma$ uncertainties, in Titan’s thermosphere and exosphere, as a function of altitude. The solid circles are for inbound densities, and the open circles for outbound. Comparison between the average inbound and outbound H_2 profiles indicates that the wall effect is important for H_2 above the exobase, but not below. My analysis in this chapter relies exclusively on the inbound data. 132
- 6.2 The H_2 density profiles calculated with the collisionless model, assuming a truncated Maxwellian VDF for exospheric particles. Different lines correspond to different choices of the exobase temperature, with the solid line representing the most probable value of 151.2 K. The dotted line shows the exospheric H_2 profile calculated from collisionless Monte-Carlo simulations, including Saturn’s gravitational influence. An exobase height of 1,500 km is adopted. The models are overplotted on the INMS measurements averaged over all flybys in the sample. 134

LIST OF FIGURES – *Continued*

- 6.3 The thermal structure for the diffusing H_2 component on Titan, calculated from Eqn. 6.1 and satisfying energy flux continuity at the upper boundary. The model predicts a modest temperature decrement of ~ 2.5 K for H_2 from the lower boundary to the exobase. . . . 137
- 6.4 The relative magnitudes of various terms in the 13-moment energy equation (Eqn. 6.1). Different lines represent the energy gain/loss rates associated with different mechanisms, including thermal conduction (solid), viscosity (short-dashed), adiabatic outflow (dotted), and $\text{H}_2\text{-N}_2$ neutral collisions (long-dashed). 138
- 6.5 The relative magnitudes of various energy fluxes, including the conductive heat flux (dotted), the viscous energy flux (short-dashed), and the intrinsic energy flux (long-dashed) which combines the internal energy, the gravitational energy, as well as the bulk kinetic energy. The total energy flux is given by the thick solid line, which tends to follow the condition of energy flux continuity (given by the thin solid line) above $\sim 1,600$ km. 140
- 6.6 The model H_2 density profiles calculated with different values of the constant timescale for H_2 loss, assuming an exobase temperature of 154 K. The models are overplotted on the INMS data for comparison. The solid line corresponds to the case with no external loss mechanism. 143
- 6.7 The full two-dimensional velocity distribution in the 13-moment approximation (scaled by the drifting Maxwellian), plotted as a function of horizontal and radial velocities (scaled by either the local thermal velocity or the local escape velocity). Several representative contours are drawn. The upper panel and lower panel show the velocity distribution at 1,000 km and 2,500 km, respectively. Departure from Maxwellian is clearly seen at high altitudes. 151

LIST OF TABLES

2.1	Summary of the trajectory geometry at C/A for all Titan flybys used in this study. Altitudes (ALT) are given in km; latitudes (LAT) and longitudes (LON) are given in degrees, with latitudes defined as positive north and longitudes defined as positive east. The F10.7 cm solar fluxes are given in units of 10^{-19} ergs cm^{-2} s^{-1} for 1 AU.	28
3.1	Flight unit peak sensitivities. Values in parenthesis are calibrated REU values according to Eqn. 3.23, while the remainings are directly measured FU values. All sensitivities are in units of 10^{-4} counts $(\text{cm}^{-3} \text{s})^{-1}$	36
4.1	Relative uncertainties due to counting statistics and sensitivity calibration. In cases where the upper limits are obtained for the mixing ratios of several minor species, I only give the relative uncertainties due to sensitivity calibration, calculated as the standard deviations of upper limits from 1,000 random realizations.	68
5.1	Globally averaged total densities and mixing ratios of neutral constituents in Titan's upper atmosphere, obtained directly from the inbound measurements, assuming ram pressure enhancement only. Errors include uncertainties due to both counting statistics and sensitivity calibration.	85
5.2	Globally averaged mixing ratios of various minor species, both directly obtained from the inbound measurements assuming ram pressure enhancement and with possible effects of wall adsorption/desorption corrected. The correction is based on the possible values of adsorption probability and desorption time constant that are able to reproduce the time behavior of observed chamber densities. All mixing ratios are referred to an altitude of 1,077 km or 1,025 km, and the values at other altitudes can be obtained with the condition of diffusive equilibrium.	99

LIST OF TABLES – *Continued*

5.3	Comparisons between the INMS mixing ratios obtained directly from the CSN mode and the values predicted from the ion abundances measured in the OSI mode. The OSI values are adopted from Vuitton <i>et al.</i> (2008) based on the INMS T5 measurements. The CSN values for both the inbound and outbound T5 measurements are given, along with the values corrected for wall adsorption/desorption. All densities are derived from the integrated mass spectrum between 1,030 and 1,200 km.	106
5.4	Thermospheric temperatures of Titan. ϕ , θ and t stand for latitude, longitude and local solar time, respectively. All temperatures are determined from the barometric fitting of the observed N ₂ profiles averaged over the selected ranges of latitude, longitude or solar local time.	108
5.5	Kendall's- τ correlation coefficients. The numbers in the parenthesis are the significance levels of the Kendall's- τ correlation coefficients that deviate from a null hypothesis. The correlation coefficients are calculated between mixing ratio and latitude in the northern hemisphere (meridional), between mixing ratio and absolute longitude relative to the facing-Saturn side, $ \theta $ or the ideal ramside, $ \theta - 90^\circ $ (zonal), and between mixing ratio and $ h - 12 $, where h is the local solar time in hr (diurnal).	123
6.1	Characteristic timescales of H ₂ . The dynamical timescale refers to the mean time required by particles with different orbital characteristics to reach an altitude of 4,000 km, assuming they are injected in random upward directions and satisfy the Maxwellian VDF with a temperature of 154 K.	146
6.2	Thermal escape of H ₂ on Titan, where F_s denotes the H ₂ escape flux, referred to Titan's surface, and R denotes the H ₂ escape rate, equal to the escape flux multiplied by Titan's surface area.	153

ABSTRACT

In this thesis I present an in-depth study of the distribution of various neutral species in Titan's upper atmosphere, at altitudes between 950 and 1,500 km for abundant species (N_2 , CH_4 as well as their isotopes) and between 950 and 1,200 km for most minor species. However, the study of the H_2 distribution on Titan is extended to an altitude as high as 6,000 km in the exosphere. The analysis is based on a large sample of Cassini/INMS (Ion Neutral Mass Spectrometer) measurements in the CSN (Closed Source Neutral) mode, obtained during 15 close flybys of Titan.

The densities of abundant species including N_2 , CH_4 and H_2 are determined directly from their main channels. However, to untangle the overlapping cracking patterns of minor species, the technique of Singular Value Decomposition (SVD) is used to determine simultaneously the densities of various hydrocarbons, nitriles and oxygen compounds. All minor species except for ^{40}Ar present density enhancements measured during the outbound legs. This can be interpreted as a result of wall effects, which could be either adsorption/desorption or heterogeneous surface chemistry on the chamber walls. In the thesis, I use a simple model to describe the observed time behavior of minor species. Results on their atmospheric abundances are provided both in terms of direct inbound measurements assuming ram pressure enhancement and values corrected for wall adsorption/desorption. Among all minor species of photochemical interest, the INMS data provide direct observational evidences for C_2H_2 , C_2H_4 , C_2H_6 , $\text{CH}_3\text{C}_2\text{H}$, C_4H_2 , C_6H_6 , HC_3N and C_2N_2 in Titan's upper atmosphere. Upper limits are put for other minor species.

The globally averaged distribution of N_2 , CH_4 and H_2 are each modeled with the diffusion approximation. The N_2 profile suggests an average thermospheric temperature of 154 K. The CH_4 and H_2 distribution constrains their fluxes to be $3.0 \times 10^9 \text{ cm}^{-2} \text{ s}^{-1}$ and $1.3 \times 10^{10} \text{ cm}^{-2} \text{ s}^{-1}$, referred to Titan's surface. The H_2 escape

flux is about a factor of ~ 3 higher than the Jeans value, which is interpreted as enhanced thermal escape driven primarily by an upward conductive heat flux. Such a conclusion is based on kinetic model calculations in the 13-moment approximation that require energy continuity at the upper boundary. On the other hand, a proper interpretation of the observed CH_4 escape has to rely on the detailed nonthermal processes, which are still unknown at the present time. The INMS observations of the nitrogen isotope ratio implies $^{14}\text{N}/^{15}\text{N} = 131.6$ near Titan's surface. The profile of carbon isotope ratio combining INMS and GCMS results implies that both CH_4 and its isotope escape from Titan's exobase with roughly the same drift velocity, in contrast to the Jeans case which requires that CH_4 escapes with a much larger velocity due to its smaller mass.

The INMS data also suggest horizontal/diurnal variations of temperature and neutral gas distribution in Titan's thermosphere. The equatorial regions, the ram-side, as well as the nightside hemisphere of Titan appear to be warmer and present some evidences for the depletion of light species such as CH_4 . Meridional variations of most heavy species are also observed, with a trend of depletion toward the north pole. Though some of the above variations might be interpreted by either the solar-driven models or plasma-driven models, a physical scenario that reconciles all the observed horizontal/diurnal variations in a consistent way is still missing. With a careful evaluation of the effect of restricted sampling, some of the features shown in the INMS data are more likely to be observational biases.

CHAPTER 1

INTRODUCTION

Titan has a thick and extended atmosphere, which is composed of at least four distinct regions: troposphere, stratosphere, mesosphere and thermosphere (Yelle 1991). Throughout Titan's atmosphere below the exobase, the most abundant constituent is N_2 , followed by several percent of CH_4 and several tenths of percent of H_2 . Other minor species, including various hydrocarbons and nitriles, are also present on Titan, as products of the complicated photochemical network initiated by the dissociation of N_2 and CH_4 by solar UV photons, energetic ions/electrons from Saturn's magnetosphere, as well as cosmic ray particles (e.g. Wilson & Atreya 2004). This thesis focuses on the distribution of various neutral constituents in Titan's thermosphere above 950 km, which coexists with an ionosphere (e.g. Bird *et al.* 1997).

During the pre-Cassini epoch, our information on the structure and composition of Titan's thermosphere relied exclusively on the disk-averaged dayglow spectra and solar occultation data obtained with the Voyager UltraViolet Spectrometer (UVS) (e.g. Broadfoot *et al.* 1981, Smith *et al.* 1982, Strobel & Shemansky 1982, Strobel *et al.* 1992, Vervack *et al.* 2004). These earlier results have been used extensively to develop models of Titan's upper atmosphere in various aspects, including photochemistry (Yung *et al.* 1984, Toubanc *et al.* 1995, Lara *et al.* 1996, Banaszkiewicz *et al.* 2000, Wilson & Atreya 2004, Lavvas *et al.* 2008a, b), ion chemistry (Ip 1990, Keller *et al.* 1992, Fox & Yelle 1997, Molina-Cuberos *et al.* 2002), thermal structure (e.g. Lellouch *et al.* 1990, Yelle 1991), non-thermal escape (Lammer & Bauer 1993, Cravens *et al.* 1997, Lammer *et al.* 1998, Shematovich *et al.* 2001, 2003, Michael *et al.* 2005, Michael & Johnson 2005), as well as dynamics (Rishbeth *et al.* 2000, Müller-Wodarg *et al.* 2000, 2003, Müller-Wodarg & Yelle 2002).

The first in-situ measurements of the concentrations of various species in Titan's thermosphere have been made by the Ion Neutral Mass Spectrometer (INMS) on the

Cassini orbiter during its close Titan flybys (Waite *et al.* 2005). The INMS results, combined with observations made by other instruments onboard Cassini/Huygens, provide extensive information on the composition and structure of Titan’s atmosphere, and will certainly initiate many new modeling efforts. Results of investigation based on INMS have already been presented in Waite *et al.* (2005), Cravens *et al.* (2006), Yelle *et al.* (2006, 2008), De La Haye *et al.* (2007a, b), Lavvas *et al.* (2008a, b), Vuitton *et al.* (2007, 2008), Cui *et al.* (2008a, b) and Müller-Wodarg *et al.* (2006, 2008). Primary scientific goals of the INMS investigation include (1) to understand the detailed photochemistry leading to the formation of various hydrocarbons, nitriles and oxygen compounds on Titan; (2) to examine Titan’s atmospheric response to solar and magnetospheric energy inputs; and (3) to constrain the dynamics and escaping processes that take place in Titan’s upper atmosphere (Waite *et al.* 2004).

The INMS instrument consists of separate ion sources for sampling neutrals (in the Closed Source Neutral mode, hereafter CSN) and ions (in the Open Source Ion mode, hereafter OSI) in the coupled thermosphere and ionosphere of Titan (Waite *et al.* 2004). The INMS data obtained in the OSI mode have been presented recently by Cravens *et al.* (2006) and Vuitton *et al.* (2007), revealing that Titan has the most compositionally complex ionosphere in the Solar system, with ~ 50 ion species detected by the INMS. Starting from the measured ion abundances and based on an ion-neutral chemistry model, Vuitton *et al.* (2007) calculated the densities of various neutral species in Titan’s upper atmosphere. These predicted results can be compared with direct INMS measurements in the CSN mode, which helps us to understand better the neutral formation mechanisms in Titan’s upper atmosphere.

In this thesis, I present our analysis of a large sample of INMS measurements in the CSN mode, aimed at providing an extensive information on the abundances of various neutral species, both globally averaged and horizontally/diurnally varied, in Titan’s thermosphere, between 950 and 1,500 km for abundant species (N_2 , CH_4 , H_2) and between 950 and 1,200 km for other minor species. This study serves as an extension of the work by Waite *et al.* (2005) based on the INMS data from the TA

flyby, and is also complementary to the work by Vuitton *et al.* (2007) based on the INMS T5 data in the OSI mode. For the distribution of H_2 on Titan, the analysis will be extended to regions far above the exobase.

The structure of the thesis is as follows. Basic information on the instrumentation and observation is detailed in Chapter 2. I present the procedures of calibrating the raw INMS data in Chapter 3. In Chapter 4, I describe the basic algorithm to derive abundances of different neutral species, as well as an assessment of the primary source of errors. Results on the neutral gas distribution in Titan's thermosphere are detailed in Chapter 5, including evidences for wall chemistry (Chapter 5.1), the globally averaged distribution of various neutral species (Chapter 5.2), as well as their possible horizontal/diurnal variations (Chapter 5.3). The analysis of the H_2 distribution in both Titan's thermosphere and exosphere is presented in Chapter 6, in which I propose a kinetic model in the 13-moment approximation to interpret the observation of a large H_2 loss rate. Finally, I summarize and conclude in Sec. 6.

CHAPTER 2

INSTRUMENTATION AND OBSERVATION

The spectral analysis presented in this thesis relies exclusively on the measurements made in the Close Source Neutral (CSN) mode, which is specifically designed to optimize interpretation of the sampled neutral species (Waite *et al.* 2004). In this mode, the inflowing gas particles enter the orifice of a spherical antechamber, and thermally accommodate to the wall temperature through collisions. These particles then enter the ionization region where they get ionized by a collimated electron beam emitted from hot-filament electron guns. A quadrupole switching lens and other electrostatic lenses focus these ions into a dual radio frequency quadrupole mass analyzer, which filters the incoming ion fluxes according to their mass-to-charge ratios (hereafter M/Z). More details on the INMS instrumentation can be found in Waite *et al.* (2004).

In the four years' length of the prime Cassini mission, there will be over 40 encounters with Titan. My thesis work is based on the INMS data acquired during 15 of them, known in project parlance as T5, T16, T18, T19, T21, T23, T25, T26, T27, T28, T29, T30, T32, T36 and T37. This sample is nearly identical to that used in the recent investigations of N₂, CH₄ and ⁴⁰Ar on Titan (Müller-Wodarg *et al.* 2008, Yelle *et al.* 2008). In this study, for abundant species such as N₂ and CH₄, I investigate their distributions below the exobase at ~1,500 km, for H₂ the analysis is extended to an altitude of ~6,000 km, while for other minor species including various hydrocarbons, nitriles and oxygen compounds, the analysis is constrained to altitudes below 1,200 km. The INMS data from the T36 and T37 flybys, which were obtained recently, have not been included in any previous work. The INMS data from other low altitude flybys are excluded for various reasons: (1) The INMS operated only in the OSI mode during the T4 flyby; (2) The TA, T9, T13, T17 and T34 flybys primarily cover regions of Titan's upper atmosphere above the altitude

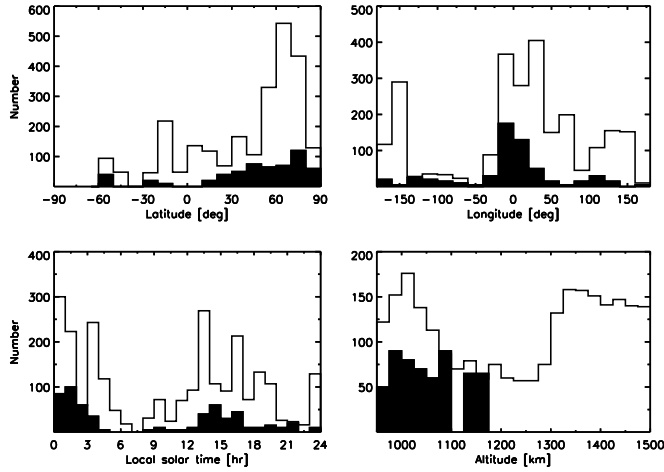


Figure 2.1 The distribution of the INMS sample adopted in this work, with respect to latitude, longitude, local solar time, as well as altitude. The sample is exclusively for solar minimum conditions, and preferentially selects measurements made over Titan’s northern hemisphere and the facing-Saturn side. The open histograms represent the sampling of abundant species including N_2 and CH_4 , extending from 950 km to 1,500 km. The filled histograms represent the sampling of other minor species (multiplied by a factor of 5), which is restricted to altitudes below 1,200 km.

range of our interest; (3) A software error occurred during the T7 flyby; (4) For all other flybys (including TB, T3, T6, T8, T10, T11, T12, T14, T15, T20, T22, T24, T31, T33 and T35), the spacecraft orientation was not appropriate for INMS measurements, with the ram angle at closest approach (hereafter C/A) greater than 60° (see Chapter 3.2).

The main characteristics of all flybys at C/A are detailed in Table 2.1, including the date of observation, altitude, local solar time, latitude, longitude and F10.7 cm solar flux at 1 AU. Latitude and longitude are defined as northward positive and eastward positive, respectively. The data sampling covers more than two years and a half, between Apr 16, 2005 for T5 and Nov 19, 2007 for T37. The F10.7 cm solar fluxes are adopted from the daily values reported by the Dominion Radio Astrophysical Observatory at Penticton, B.C., Canada. Table 2.1 shows that altitudes at C/A range from 950 km for T16 to 1,027 km for T5.

We show in Fig. 2.1 the distribution of the INMS sample adopted in this work

with respect to latitude, longitude, local solar time and altitude. The geometric information represented by the open histograms is extracted from channel 28 of all flybys, between 950 and 1,500 km. This represents the sample distribution for abundant species including N_2 and CH_4 and their isotopes (especially $^{14}\text{N}^{15}\text{N}$ and $^{13}\text{CH}_4$) analyzed in this work. The filled histograms represent the sample distribution for minor species, whose abundances are derived from the best-fit solutions to individual mass spectra below 1,200 km (see Chapter 4.1 for details). In Fig. 2.1, the distribution for minor species has been multiplied by a factor of 5. Though both inbound and outbound passes are included in Fig. 2.1, we will show below that our analysis of most minor species will primarily rely on the inbound measurements. For all species, the sample is unevenly distributed with respect to latitude, in the sense that most measurements were made over Titan’s northern hemisphere. The T36 and T37 data are unique since they are the only low altitude flybys probing Titan’s southern hemisphere to date. Also, the sample preferentially selects measurements made near Titan’s facing-Saturn side, while the magnetospheric wakeside is poorly sampled. The mean F10.7 cm flux for our sample is 76 at 1 AU, with a standard deviation of 12%, therefore the sample exclusively represents solar minimum conditions.

The INMS data in the CSN mode consist of a sequence of number counts in mass channels 1-8 and 12-99 Daltons. For channels that are expected to show significant count rates (channels 2, 12-17, 27-29), the INMS measures the ambient atmosphere with a typical sampling time of ~ 0.92 sec, corresponding to a spatial resolution of ~ 5.5 km along the spacecraft trajectory for a typical flyby velocity of 6 km s^{-1} relative to Titan. These channels are primarily associated with N_2 , CH_4 and H_2 in the ambient atmosphere. A special case is channel 28 for the T16 flyby, with a sampling time of 0.034 s, about equal to the INMS mass step dwell time (Waite *et al.* 2004). For all other channels, the sampling time is ~ 9.3 sec, indicating that the INMS data have a typical spatial resolution of ~ 56 km for the distribution of minor neutral species.

Table 2.1 Summary of the trajectory geometry at C/A for all Titan flybys used in this study. Altitudes (ALT) are given in km; latitudes (LAT) and longitudes (LON) are given in degrees, with latitudes defined as positive north and longitudes defined as positive east. The F10.7 cm solar fluxes are given in units of 10^{-19} ergs cm $^{-2}$ s $^{-1}$ for 1 AU.

Flyby	Date	ALT	LST	LAT	LON	F10.7
T5	4/16/05	1,027	23:17	74	89	83
T16	7/22/06	950	17:21	85	45	72
T18	9/23/06	962	14:25	71	3.0	70
T19	10/9/06	980	14:20	61	2.6	75
T21	12/12/06	1,000	20:20	43	95	102
T23	1/13/07	1,000	14:02	31	2.1	81
T25	2/22/07	1,000	00:35	30	-16	76
T26	3/10/07	981	01:45	32	2.1	71
T27	3/25/07	1,010	01:43	41	2.1	74
T28	4/10/07	991	01:40	50	2.0	69
T29	4/26/07	981	01:36	59	1.6	81
T30	5/12/07	960	01:32	69	1.2	71
T32	6/13/07	965	01:18	85	-1.2	71
T36	10/2/07	973	16:08	-60	-109	66
T37	11/19/07	999	15:28	-21	-117	70

CHAPTER 3

DATA CALIBRATION

The raw INMS data have to be corrected for various systematic uncertainties before they can be used in the spectral analysis. In the CSN mode, I take into account calibration of sensitivities, correction for ram pressure enhancement, correction for saturation in the high gain counter, removal of thruster firing contaminations, subtraction of background counts, as well as correction for channel crosstalk. The detailed procedures for these calibrations are described below in Chapter 3.1-3.6.

3.1 Sensitivities

The laboratory sensitivity calibration of the INMS flight unit (hereafter FU) was performed at Goddard Space Flight Center (GSFC) prior to launch (Waite *et al.* 2004). This pre-flight calibration was performed with the principle non-reactive neutral species expected on Titan, including N_2 , CH_4 , H_2 , C_2H_2 , C_2H_4 and ^{40}Ar . In addition, He and Kr were also chosen as reference species. Especially, Kr was used to characterize the FU performance for large M/Z (Waite *et al.* 2004). The calibration with Kr is important because of the presence of heavy hydrocarbons on Titan, such as C_6H_6 (Vuitton *et al.* 2008).

Characterization of INMS performance was continued during the post-launch period with the engineering unit (hereafter EU), including additional neutral species that had not been calibrated pre-flight. After the initial EU characterization immediately post-launch, the EU sensor ion sources were refurbished to better represent FU. This refurbished engineering unit (hereafter REU) has been used since early 2006 to characterize a large number of gases of scientific interest on Titan guided by preliminary INMS results. Because of differences in the response of the FU and REU, it is necessary to derive an algorithm to transfer the REU sensitivities for the

newly calibrated gases to the FU. This algorithm, described below, is based on the gases common to both the FU and REU calibrations.

3.1.1 Corrections for terrestrial isotope ratios

In most cases, both the FU and REU characterizations were performed on mixtures of reference gases with isotope. Therefore it is necessary, as the first step, to separate the relative contributions from the main gas and its isotope. An example is the calibration of the N_2 reference gas, which is actually a mixture of N_2 and $^{14}N^{15}N$. Denoting the count rates in channel i with $C(i)$, the densities of species j with $n(j)$, and the corresponding sensitivity with $S(i, j)$, we have

$$C(14) = S(14, N_2)n(N_2) + S(14, ^{14}N^{15}N)n(^{14}N^{15}N), \quad (3.1)$$

$$C(15) = S(15, ^{14}N^{15}N)n(^{14}N^{15}N), \quad (3.2)$$

$$C(28) = S(28, N_2)n(N_2), \quad (3.3)$$

$$C(29) = S(29, ^{14}N^{15}N)n(^{14}N^{15}N). \quad (3.4)$$

The terrestrial nitrogen isotope ratio is 271, corresponding to $y(N_2) = n(N_2)/n(^{14}N^{15}N) = 135$ since two N atoms make up one N_2 molecule. With this, Eqn. 3.1-3.4 can be recast as

$$\hat{S}(14, N_2) = S(14, N_2) + \frac{S(14, ^{14}N^{15}N)}{y(N_2)}, \quad (3.5)$$

$$\hat{S}(15, N_2) = \frac{S(15, ^{14}N^{15}N)}{y(N_2)}, \quad (3.6)$$

$$\hat{S}(28, N_2) = S(28, N_2), \quad (3.7)$$

$$\hat{S}(29, N_2) = \frac{S(29, ^{14}N^{15}N)}{y(N_2)}, \quad (3.8)$$

where $\hat{S}(i, j) = C(i)/n(j)$ represents the sensitivity not corrected for isotope ratio. Clearly we have $S(14, ^{14}N^{15}N) = S(15, ^{14}N^{15}N)$, and Eqn. 3.5-3.8 can be used to uniquely determine the values of the four independent unknowns, $S(14, N_2)$, $S(28, N_2)$, $S(14, ^{14}N^{15}N)$ and $S(29, ^{14}N^{15}N)$.

The case for CH_4 and its isotope $^{13}CH_4$ is similar though more complicated. Here the count rates in channels 12-17 are relevant, and with $y(CH_4) =$

$n(\text{CH}_4)/n(^{13}\text{CH}_4) = 90$ for the terrestrial composition, we have analogous to Eqn. 3.5-3.8,

$$\hat{S}(2, \text{CH}_4) = S(2, \text{CH}_4) + \frac{S(2, ^{13}\text{CH}_4)}{y(\text{CH}_4)}, \quad (3.9)$$

$$\hat{S}(3, \text{CH}_4) = S(3, \text{CH}_4) + \frac{S(3, ^{13}\text{CH}_4)}{y(\text{CH}_4)}, \quad (3.10)$$

$$\hat{S}(12, \text{CH}_4) = S(12, \text{CH}_4), \quad (3.11)$$

$$\hat{S}(13, \text{CH}_4) = S(13, \text{CH}_4) + \frac{S(13, ^{13}\text{CH}_4)}{y(\text{CH}_4)}, \quad (3.12)$$

$$\hat{S}(14, \text{CH}_4) = S(14, \text{CH}_4) + \frac{S(14, ^{13}\text{CH}_4)}{y(\text{CH}_4)}, \quad (3.13)$$

$$\hat{S}(15, \text{CH}_4) = S(15, \text{CH}_4) + \frac{S(15, ^{13}\text{CH}_4)}{y(\text{CH}_4)}, \quad (3.14)$$

$$\hat{S}(16, \text{CH}_4) = S(16, \text{CH}_4) + \frac{S(16, ^{13}\text{CH}_4)}{y(\text{CH}_4)}, \quad (3.15)$$

$$\hat{S}(17, \text{CH}_4) = \frac{S(17, ^{13}\text{CH}_4)}{y(\text{CH}_4)}. \quad (3.16)$$

The number of linear equations (8) is smaller than the total number of unknowns (14). To complete the problem, I further assume that CH_4 and $^{13}\text{CH}_4$ have similar cracking patterns, i.e.

$$\frac{S(2, \text{CH}_4)}{S(16, \text{CH}_4)} = \frac{S(2, ^{13}\text{CH}_4)}{S(17, ^{13}\text{CH}_4)}, \quad (3.17)$$

$$\frac{S(3, \text{CH}_4)}{S(16, \text{CH}_4)} = \frac{S(3, ^{13}\text{CH}_4)}{S(17, ^{13}\text{CH}_4)}, \quad (3.18)$$

$$\frac{S(12, \text{CH}_4)}{S(16, \text{CH}_4)} = \frac{S(13, ^{13}\text{CH}_4)}{S(17, ^{13}\text{CH}_4)}, \quad (3.19)$$

$$\frac{S(13, \text{CH}_4)}{S(16, \text{CH}_4)} = \frac{S(14, ^{13}\text{CH}_4)}{S(17, ^{13}\text{CH}_4)}, \quad (3.20)$$

$$\frac{S(14, \text{CH}_4)}{S(16, \text{CH}_4)} = \frac{S(15, ^{13}\text{CH}_4)}{S(17, ^{13}\text{CH}_4)}, \quad (3.21)$$

$$\frac{S(15, \text{CH}_4)}{S(16, \text{CH}_4)} = \frac{S(16, ^{13}\text{CH}_4)}{S(17, ^{13}\text{CH}_4)}. \quad (3.22)$$

Eqn. 3.9-3.22 form a complete set of 14 independent linear equations, which can be used to uniquely determine the values of all the unknown sensitivities. Similar

procedures are used to infer isotope-specific sensitivities for H_2 , Ar and Kr. Usually, the corrections to peak sensitivities are small (except for Kr), typically on 1% level, although the corrections to the branching ratios can be large. I show below how the peak sensitivities as well as the branching ratios, with proper corrections for isotope ratios, are calibrated between the FU and REU.

3.1.2 Calibrations of peak sensitivities between flight unit (FU) and refurbished engineering unit (REU)

In this section, I present several possible schemes for calibrating the peak sensitivities between the FU and REU characterizations. The calibration depends on eight species for which both FU and REU sensitivities are available, including H_2 , He, CH_4 , C_2H_2 , N_2 , C_2H_4 , Ar, Kr and their isotope. The peak sensitivity of a neutral species always refers to the highest value shown in its cracking pattern. For most species, the channel of peak sensitivity corresponds to the singly ionized state of the parent molecule.

One possible scheme for calibrating peak sensitivities is to examine the offsets between FU and REU values, i.e. $S_{\text{FU}} - S_{\text{REU}}$. The upper panel of Fig. 3.1 shows that although the scattering is relatively large, the offset varies approximately linearly with M/Z . The best-fit linear relation is given by the solid line in the figure. The lower panel of Fig. 3.1 presents the relation between REU peak sensitivities and M/Z , with the solid line giving the offsets that need to be applied to obtain the FU values. We see that for several heavy species (C_4H_6 , $\text{C}_2\text{H}_3\text{CN}$, C_6H_6 and C_7H_8), the required offsets are comparable with or even greater than the measured REU sensitivities. This raises a conceptual difficulty, in the sense that the peak sensitivity for a heavy species might be largely controlled by the offset alone, independent of the actually measured REU value. This is a physically unrealistic situation, and the scheme for calibration based on offset is therefore not adopted in this work.

As an alternative scheme, I normalize the REU sensitivities to the FU values with a direct scaling, as shown in Fig. 3.2a. Except for Kr, the correlation between the FU and REU values can be reasonably described by a linear relation, shown as the

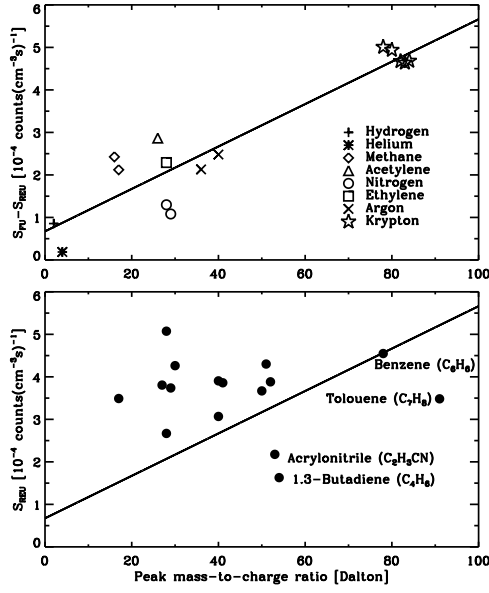


Figure 3.1 Upper panel: The difference between the FU and REU peak sensitivities shown as a function of peak M/Z. All FU/REU measurements can be roughly fitted with a linear relation. Lower panel: The REU peak sensitivities as a function of peak M/Z. The solid line represents the offset, $S_{FU} - S_{REU}$ that needs to be applied to get the corresponding FU values. For several heavy neutral species (C_4H_6 , $\text{C}_2\text{H}_3\text{CN}$, C_6H_6 and C_7H_8), the required offsets are comparable with or greater than the measured REU sensitivities.

solid line in the figure. However, the Kr data is quite badly fit by the linear relation. This is a serious failing because Kr is the only species available for characterizing the high-mass end of the INMS spectrum, and it is important to adopt a calibration scheme that is valid for this species.

I further investigate a different linear relation between the FU and REU peak sensitivities, in which data from both FU and REU are scaled by the cross section of electron impact ionization for the species in question. Such a scaling is physically motivated, since the probability for ionization by electron impact is proportional to the corresponding cross section. The relation between the FU and REU peak sensitivities scaled by cross section is shown in Fig. 3.2b, indicating that measurements for Kr are still outliers, similar to the unscaled case.

The way that an ionized molecule passes through the switching and focusing lens system depends on M/Z (Waite *et al.* 2004). This motivates us to investigate the relationship between the FU and REU peak sensitivities, when both are scaled by M/Z of the dissociative fragments. Such a relation is presented in Fig. 3.2c, which shows that all species, including Kr, lie approximately on a straight line given by

$$(M/Z)^{-1}S_{\text{FU}} = 3.321 \times 10^{-6} + 1.291(M/Z)^{-1}S_{\text{REU}}, \quad (3.23)$$

where S_{FU} and S_{REU} represent the FU and REU peak sensitivities in units of counts $(\text{cm}^{-3} \text{ s})^{-1}$. I adopt this relationship to transfer REU sensitivities to the FU. However, for species for which both REU and FU calibrations are available, the FU peak sensitivities are always used.

An estimate of the uncertainties of peak sensitivities is required, which will be used later to determine the density errors of the ambient atmosphere from the INMS data (see Chapter 4.5). The uncertainties for the two coefficients in Eqn. 3.23 are calculated from the corresponding covariance matrix. These are then used to calculate the uncertainties of the peak FU sensitivities. The peak sensitivities for all neutral species included in our spectral analysis, appropriate for the FU characterization, are listed in Table 3.1, with 1σ relative uncertainties. The relative uncertainty tends to increase with mass, and can be as large as 10% for complex

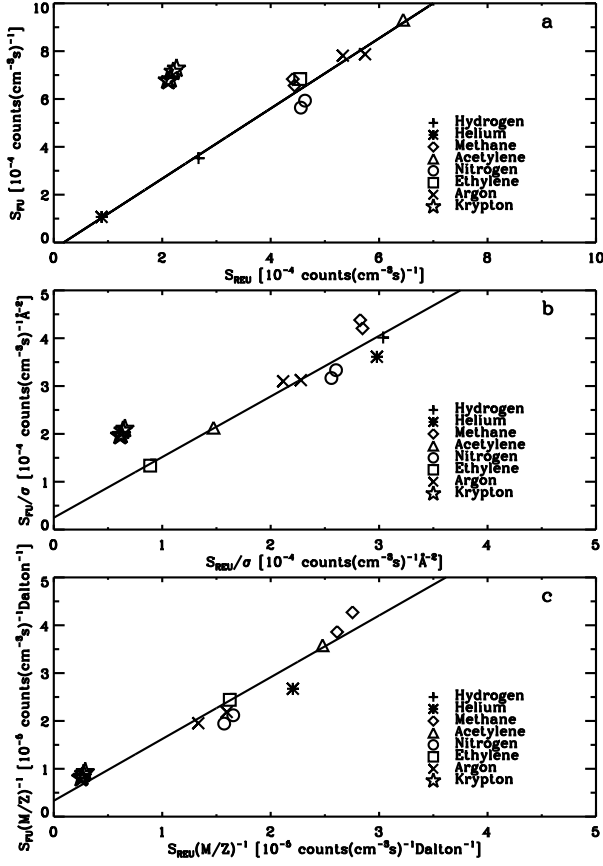


Figure 3.2 The relation between the FU and REU peak sensitivities, unscaled (panel a), scaled by the cross section for electron impact ionization (panel b), or scaled by the peak M/Z (panel c). Except for panel c, isotopes of Kr appear to be outliers. The solid lines are obtained by a linear fitting to the FU and REU measurements, including all species for panel c but excluding Kr for panels a and b. The best-fit relation shown in panel c is given by Eqn. 3.23 in the text.

Table 3.1 Flight unit peak sensitivities. Values in parenthesis are calibrated REU values according to Eqn. 3.23, while the remainings are directly measured FU values. All sensitivities are in units of 10^{-4} counts $(\text{cm}^{-3} \text{ s})^{-1}$.

Species	Name	Peak M/Z	S_{FU}	$\sigma(S_{\text{FU}})/S_{\text{FU}}$
H ₂	hydrogen	2	3.526	0.018
HD	deuterium hydride	3	1.857	0.021
CH ₄	methane	16	6.833	0.025
¹³ CH ₄	methane	17	6.563	0.027
(NH ₃)	ammonia	17	5.068	0.032
(H ₂ O)	water	18	4.696	0.036
C ₂ H ₂	acetylene	26	9.310	0.028
(HCN)	hydrogen cyanide	27	5.809	0.042
C ₂ H ₄	ethylene	28	6.836	0.038
N ₂	nitrogen	28	5.931	0.044
¹⁴ N ¹⁵ N	nitrogen	29	5.638	0.047
(¹⁵ N ¹⁵ N)	nitrogen	30	6.498	0.042
(C ₂ H ₆)	ethane	28	7.478	0.035
³⁶ Ar	argon	36	7.872	0.042
⁴⁰ Ar	argon	40	7.811	0.046
(CH ₂ C ₂ H ₂)	allene	40	6.368	0.055
(CH ₃ C ₂ H)	methyacetylene	40	5.288	0.066
(CH ₃ CN)	acetonitrile	41	6.343	0.057
(C ₃ H ₈)	propane	29	5.787	0.045
(CO ₂)	carbon dioxide	44	8.154	0.048
(C ₄ H ₂)	diacetylene	50	6.396	0.068
(HC ₃ N)	cyanoacetylene	51	7.244	0.061
(C ₂ N ₂)	cyanogen	52	6.737	0.067
(C ₂ H ₃ CN)	acrylonitrile	53	4.569	0.099
(C ₄ H ₆)	1,3-butadiene	54	3.895	0.118
(C ₂ H ₅ CN)	propanenitrile	28	4.374	0.056
(C ₆ H ₆)	benzene	78	8.460	0.079
(C ₇ H ₈)	toluene	91	7.516	0.103

species such as C₄H₆ and C₇H₈. The origins for the listed sensitivities are also indicated in Table 3.1, either directly taken from pre-flight measurements, or calibrated from the REU values according to Eqn. 3.23.

I notice that the best-fit linear relation given by Eqn. 3.23 has a finite offset, implying that the predicted FU peak sensitivity is non-zero even if the REU calibration gives a zero sensitivity. Although this is a physically unrealistic feature, the smallest peak sensitivity (scaled by M/Z) among all species appears for C₄H₆ with a value of 7.215×10^{-6} counts $(\text{cm}^{-3} \text{ s})^{-1}$. This is more than a factor of 2 greater than the offset value of 3.321×10^{-6} counts $(\text{cm}^{-3} \text{ s})^{-1}$, implying that the potential errors associated with the non-zero offset in Eqn. 3.23 are not significant.

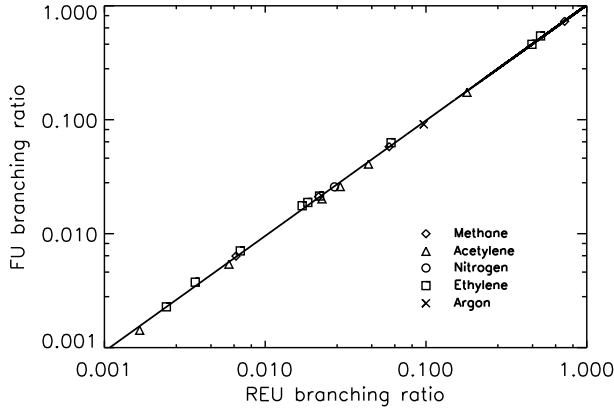


Figure 3.3 The relation between the REU and FU branching ratios for N_2 , CH_4 , ^{40}Ar , C_2H_2 and C_2H_4 . Isotopes are not included. The solid line shows the best-fit log-linear relation, given by Eqn. 3.24. The corrections from the REU to FU branching ratios are relatively small, ranging between 0.5% and 7%.

3.1.3 Cracking patterns

In addition to the peak sensitivity, the cracking pattern of a given neutral species also requires calibration between the FU and REU measurements. I show in Fig. 3.3 the FU and REU branching ratios for several species, including N_2 , CH_4 , C_2H_2 , C_2H_4 and Ar. Isotopes are not included since I assume that the branching ratios for a species are the same as those for its isotope (e.g. Eqn. 3.17-3.22 for CH_4). Typically, the REU and FU cracking patterns are nearly identical. Fig. 3.3 shows that the calibration between the REU and FU branching ratios can be described by a log-linear relation with the form

$$\log b_{FU} = 0.007 + 1.014 \log b_{REU}, \quad (3.24)$$

where b_{FU} and b_{REU} represent the FU and REU branching ratios. Such a log-linear relation is given by the solid line in Fig. 3.3. Similar to the calibration of peak sensitivities, for all species with FU characterization available, the FU cracking patterns are always adopted. For gases with only REU measurements, Eqn. 3.24 is used to predict the corresponding FU cracking patterns. The corrections according to Eqn. 3.24 are small, ranging between 0.5% and 7%.

Uncertainties of the inferred branching ratios are estimated from the errors of the two coefficients in the log-linear relation given by Eqn. 3.24, which are calculated from the corresponding covariance matrix. On average, the relative uncertainties of branching ratios are $\sim 4\%$, smaller than those of the peak sensitivities which range between 3% and 10%. Notice that the calibration of cracking pattern presented here depends on the measurements of dissociative fragments with $M/Z < 20$. A simple extrapolation to heavy fragments, encountered in the cracking patterns of heavy neutral species such as C_6H_6 , is implicitly assumed in the calibration.

Additional calibration of the cracking pattern is required to guarantee that densities of a given species derived from different channels are consistent. As an example, I find that the N_2 densities determined from channel 28 are not identical to those determined from channel 14. As pointed out by Yelle *et al.* (2006), this may reflect a change of the INMS sensitivity to N_2 at channel 14, and is likely to be caused by excess kinetic energy imparted to N^+ ions through electron impact dissociative ionization of N_2 . Such a feature may influence the N_2 branching ratio at channel 14, by affecting the way that the fragment ions are transmitted through the INMS ion optics. To correct for this, I calculate for each flyby the ratio of the N_2 density profile determined from channel 28 to that determined from channel 14, between 1,100 and 1,450 km. For each flyby, the average ratio is taken as a constant scaling factor, which is then used to calibrate the branching ratio of N_2 at channel 14. A complexity in the above procedure is that the $C^{(1)}$ counts in channel 28 may be saturated. The details on correcting for saturation will be presented in Chapter 3.3.

A similar procedure is performed for calibrating the branching ratios of CH_4 at channels 12, 13 and 15. An analogous scaling factor for CH_4 at channel 14 is not considered, since it is coupled to the issue of N_2 calibration at the same channel. An illustration is given in Fig. 3.4, with the solid circles representing N_2 (CH_4) densities determined from counts in channel 28 (16) and the plus signs representing those determined from counts in channel 14 (12) adopting the uncalibrated branching ratios. Offsets are clearly seen between them. The open diamonds in Fig. 3.4 give the densities derived from the calibrated branching ratios, which are consistent with

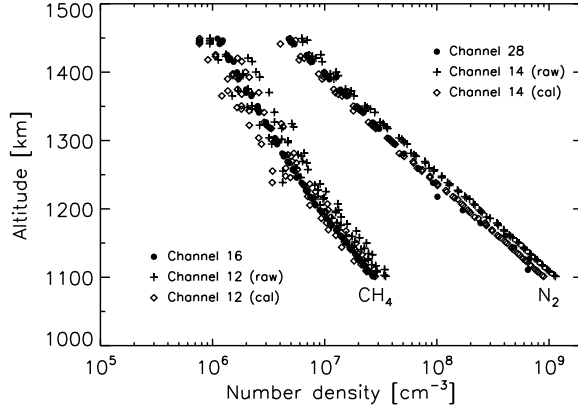


Figure 3.4 N_2 and CH_4 density profiles (for the inbound T32 measurements) as a function of altitude, determined from counts in different channels. The solid circles represent densities determined from counts in the main channel (28 for N_2 and 16 for CH_4), while the plus signs represent those from counts in a secondary channel (14 for N_2 and 12 for CH_4). The CH_4 densities can also be estimated from channels 13 and 15, which are not shown here. The open diamonds are densities determined from the secondary channels, scaled to maintain agreement with the peak channels.

those determined from the peak channels. The mean scaling factors are 0.76 ± 0.02 for N_2 at channel 14, 0.81 ± 0.02 and 0.85 ± 0.01 for CH_4 at channels 12 and 13, where the errors quoted here reflect scatterings among different flybys. On the other hand, the CH_4 scaling factor at channel 15 is very close to unity for all flybys.

In principle, a similar calibration is required for other species. However, a full knowledge of all the individual scaling factors is impossible, due to the coupling between cracking patterns of these species. In addition, introducing too many scaling factors is equivalent to introducing the same number of free parameters in the overall fit of an observed mass spectrum, which is practically unrealistic and unnecessary. For simplicity, such a correction for other species is not attempted in this work. However, it should be born in mind that the neglect of this effect may introduce additional uncertainties as large as $\sim 20\%$ in the derived densities of a neutral species, unless the densities are primarily estimated from the peak channel.

3.2 Ram pressure enhancement

The INMS response in the CSN mode, in terms of the ram pressure enhancement factor, is shown in Fig. 3.5, for several species with different molecular masses. For instrument configurations with the angle of attack (the angle between the aperture normal and the spacecraft velocity) smaller than 90° , an enhancement of the ambient number density is achieved by limiting the conductance through the transfer tube (to the ionization region) and maintaining the high conductance through the entrance aperture (Waite *et al.* 2004). With the presence of the spherical antechamber, the closed source has a geometric field of view as wide as 2π steradians, and the angular response varies as the cosine of the angle of attack (Waite *et al.* 2004). The ram enhancement factor increases with molecular mass. At a temperature of 150 K for the ambient atmosphere, the maximum enhancement factor, which appears for zero angle of attack, ranges from 13.5 for H_2 , 38 for CH_4 , 50 for N_2 , 60 for ^{40}Ar , to 84 for C_6H_6 . For angles of attack greater than 90° , the instrument response drops to zero, and the spacecraft configuration does not allow the recording of any useful data of the ambient atmosphere.

The instrument response mentioned above implies an effective peak sensitivity for any given species that is equal to the actual sensitivity multiplied by the corresponding ram enhancement factor (see also Chapter 4.1). The dependence of response on molecular mass, angle of attack, as well as the temperature of the ambient gas can be predicted from the kinetic theory, which estimates the number density in the antechamber by balancing the incoming flux at the spacecraft velocity with the outgoing flux at the thermal velocity corresponding to the wall temperature (Waite *et al.* 2004). Throughout this work, the ram enhancement factor is calculated from the kinetic theory with a fixed spacecraft velocity of 6 km s^{-1} , a temperature of 150 K in the ambient atmosphere, and a chamber wall temperature of 300 K.

The above discussion on ram pressure enhancement implicitly assumes that the incoming molecules through the entrance aperture collide elastically with the chamber walls, and effects such as adsorption/desorption and heterogeneous surface chem-

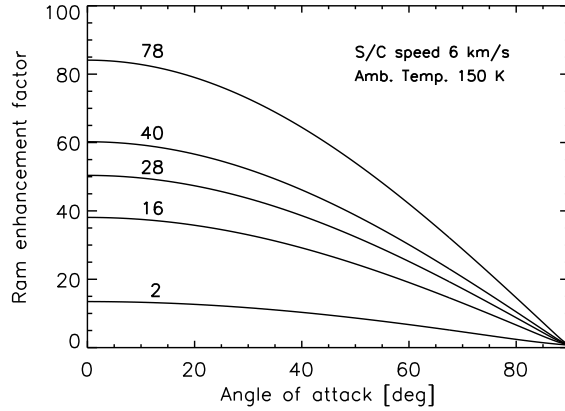


Figure 3.5 The INMS instrument response in the CSN mode (the ram enhancement factor), as a function of angle of attack, i.e. the angle between the aperture normal and the spacecraft velocity vector. Several species with different molecular masses are shown, assuming a spacecraft velocity of 6 km s^{-1} , a temperature of 150 K in the ambient atmosphere, and a chamber wall temperature of 300 K. The instrument response increases with molecular mass and varies approximately as the cosine of the angle of attack.

istry are not involved. However, such an assumption may not be correct, as revealed by recent investigations of the INMS data (Vuitton *et al.* 2008). These complexities, denoted as wall effects throughout this thesis, will be addressed in more detail in Chapter 5.1.

3.3 Saturations

The INMS has both a high gain counter (hereafter $C^{(1)}$) and a low gain counter (hereafter $C^{(2)}$). In more detail, two electron multipliers are electronically biased to allow most of the ions to be deflected into the primary detector, with the remaining being scattered into the secondary one (Waite *et al.* 2004). This design increases the overall dynamic range of INMS measurements by a factor of 1,500 (Waite *et al.* 2004). When not saturated, the $C^{(1)}$ counts, with much higher signal-to-noise ratios than $C^{(2)}$, are always used for density determination. However, the $C^{(1)}$ counts for channels 14, 15, 16, 28 and 29 are likely to be saturated at low altitudes, leading to

an underestimate of the densities of N_2 , CH_4 and $^{14}\text{N}^{15}\text{N}$ in the ambient atmosphere. Correction for saturation requires a determination of the $C^{(1)}/C^{(2)}$ conversion ratio, which is assumed to be constant for a given mass channel and for a given flyby in our work. At low altitudes, these conversion ratios are used to scale the $C^{(2)}$ counts to the actual $C^{(1)}$ counts, from which unbiased densities can be determined.

For channels 14, 15, 16 and 29, the determination of the conversion ratio is relatively easy, accomplished with a Monte-Carlo method. I assume a Poissonian distribution for the number counts in both $C^{(1)}$ and $C^{(2)}$ counters, and throw random samples of counts for a given channel by taking the measured values as the Poissonian mean. For each random realization, a conversion ratio is calculated by dividing the total $C^{(1)}$ counts to the total $C^{(2)}$ counts, over the typical altitude range of 1,050-1,300 km where counts in $C^{(1)}$ are not saturated and counts in $C^{(2)}$ are not too low. The reason for taking the ratio between total counts (as opposed to taking the average of individual count ratios) is to avoid math errors caused by possible zero $C^{(2)}$ counts. For any given channel, a mean conversion ratio is obtained by averaging over 10,000 random realizations. This procedure is repeated for each flyby in our sample.

For channel 28 in which counts are mainly contributed by the ambient N_2 gas, I have to rely on regions above $\sim 1,300$ km where the $C^{(1)}$ counts are not saturated. However, the altitude range for calculating the $C^{(1)}/C^{(2)}$ conversion ratios in this channel can be extended by noticing that the majority of counts in channel 14 are also contributed by the ambient N_2 molecules, corresponding to N^+ ions produced by electron impact dissociative ionization within the INMS instrument. This indicates that it is possible to estimate N_2 densities from $C^{(1)}$ counts of channel 14, and use the derived N_2 density profile to predict the corresponding $C^{(1)}$ counts in channel 28. These predicted $C^{(1)}$ counts do not suffer from saturation (at least for regions where $C^{(1)}$ counts of channel 14 are not saturated), and can be used to determine more accurately the $C^{(1)}/C^{(2)}$ conversion ratio for channel 28, following the Monte-Carlo procedure described above.

The determination of N_2 densities from channel 14 requires calibration of the N_2

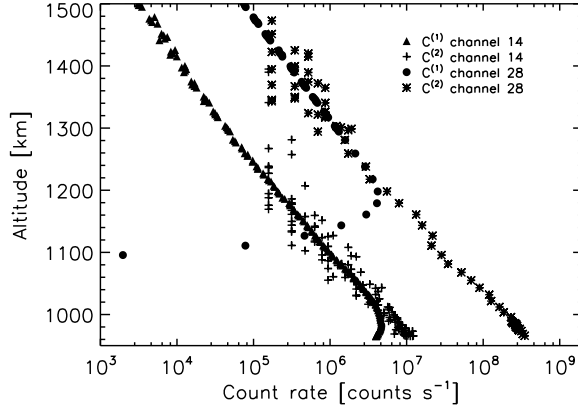


Figure 3.6 The count rates (counts s^{-1}) in channels 14 and 28 as a function of altitude, adopted from the INMS measurements made during the inbound T32 flyby. Solid triangles and circles represent data recorded at the $C^{(1)}$ counter, while plus signs and asterisks data recorded at the $C^{(2)}$ counter. The $C^{(1)}$ count rates are saturated at altitudes below $\sim 1,200$ km for channel 28 and below $\sim 1,020$ km for channel 14. The $C^{(2)}$ count rates have been multiplied by an appropriate conversion factor of 5372 for channel 28 and 4873 for channel 14, respectively.

cracking pattern, as shown in Chapter 3.1.3. Since the calibration of N_2 branching ratio at channel 14 is coupled to the calibration of $C^{(1)}$ saturation at channel 28, both the N_2 scaling factor and $C^{(2)}/C^{(1)}$ conversion ratio are derived simultaneously (in an iterative manner) to ensure self-consistency. Also notice that the CH_4 densities have to be determined separately to allow their contributions to channel 14 to be subtracted. The determination of CH_4 densities is based on the $C^{(1)}$ counts in channel 16, with contributions from $^{13}CH_4$ subtracted (Müller-Wodarg *et al.* 2008). Finally, I notice that in calculating the $C^{(1)}/C^{(2)}$ conversion ratios for channel 28, counts contributed by background signals have to be determined separately (see Chapter 3.5). Here the background signals are roughly estimated from linear interpolation of counts in surrounding channels at the same altitude, unoccupied by any neutral species in the ambient atmosphere.

The $C^{(1)}/C^{(2)}$ conversion ratio, which is assumed to be constant for each flyby, varies for different channels. The average value is 5292 ± 281 for channel 14, 4247 ± 245 for channel 15, 3768 ± 166 for channel 16, 5037 ± 205 for channel 28, and

5686 ± 297 for channel 29, where the uncertainties quoted here represent standard deviations among different flybys. An illustration of the $C^{(1)}/C^{(2)}$ conversion is given in Fig. 3.6 for the T32 inbound data. The solid circles (triangles) represent $C^{(1)}$ counts of channel 28 (14), and the asterisks (plus signs) represent the corresponding $C^{(2)}$ counts multiplied by the appropriate conversion ratio.

3.4 Thruster firings

For channel 2, additional corrections for thruster firings are required (Yelle *et al.* 2006, Cui *et al.* 2008). The Cassini spacecraft thrusters operate with hydrazine (N_2H_4), with H_2 being a significant component of the thruster effluent. This effect is usually manifest as large excursions from the expected counts in channel 2, interspersed over the whole altitude range over which measurements were made. In most cases, contamination by thruster firings is serious near C/A when thrusters fire frequently to offset the torque on the spacecraft due to atmospheric drag (Yelle *et al.* 2006). Regions thought to be contaminated by thruster firings are identified by correlating with accumulated thruster operation time, accompanied by eyeball checking (Cui *et al.* 2008). The counts in channel 2 for these regions can be replaced by the values interpolated from surrounding measurements unaffected by thruster firings for each flyby. The contamination of channel 28 counts by the same effect is ignored here, since the N_2 densities of the ambient atmosphere are much higher than those of the spacecraft effluent.

An example of the thruster firing contaminations is shown in Fig. 3.7, for the inbound T30 measurements. The open (solid) circles represent channel 2 counts which are thought to be contaminated (uncontaminated) by this effect. Also shown on the figure is the information on the accumulated thruster operation time on 1 s intervals. Each thruster firing nominally lasts 0.125 s, from which I calculate the total number of thruster firings in each 1 s interval. This number is shown on an arbitrary linear scale in Fig. 3.7, at altitudes that coincide with real measurements made in channel 2. Fig. 3.7 shows that the total number of thruster firings is not

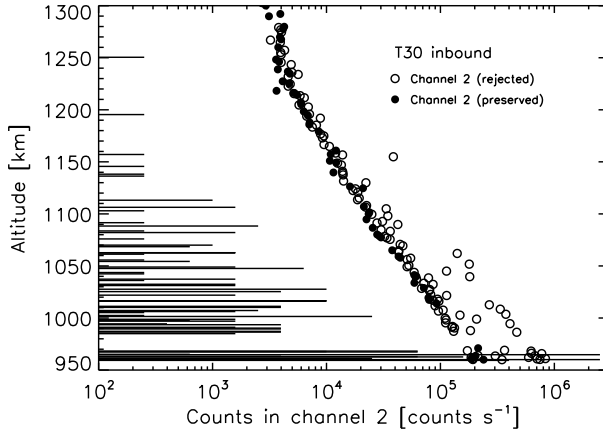


Figure 3.7 The counts in channel 2 as a function of altitude, for the inbound T30 flyby. Overplotted on the count profile is the information of accumulated thruster operation time on 1 s intervals. Each thruster firing nominally lasts 0.125 s, from which I calculate the total number of thruster firings in each 1 s interval. This number is shown on an arbitrary linear scale, at altitudes that coincide with real measurements made in channel 2. The channel 2 counts rejected from the spectral analysis due to thruster firing contaminations are shown as the open circles, while those uncontaminated are shown as the solid circles.

exactly correlated with the apparent deviations of channel 2 counts. Eyeball checking and manual rejection are sometimes required, in order to obtain a reasonable correction for the thruster firing contaminations.

3.5 Subtraction of background counts

3.5.1 Empirical background model

A typical INMS mass spectrum at low altitudes shows clear peaks centered in isolated mass channels, superimposed on a broad smooth spectrum extending over the whole M/Z range from 1 to 99 Daltons. While the isolated peaks are clearly associated with neutral constituents in the INMS antechamber, the broad spectrum is interpreted as background signals.

To subtract the background spectra, I construct an empirical model, $B(M/Z)$, defined as the sum of a constant level and the convolution of a square function with

a Gaussian kernel,

$$B(M/Z) = \frac{1}{\sqrt{2\pi}w^2} \int_{m_0-\frac{\Delta}{2}}^{m_0+\frac{\Delta}{2}} h \exp\left[-\frac{(M/Z - m)^2}{2w^2}\right] dm + c, \quad (3.25)$$

where c is the constant level, h , m_0 and Δ are the height, center and width of the square function, w is the width of the Gaussian kernel. There are consequently five free parameters in the empirical model fitting.

In practice, for a given mass spectrum, I determine the constant level, c by taking the average of all counts in channels with $M/Z > 65$. Peak counts are usually clearly identified in channels 73-80, and in some cases, minor peaks are seen in channels 90-91, due to the presence of C_6H_6 and C_7H_8 in the INMS antechamber (Vuitton *et al.* 2008). These channels have to be avoided in calculating the constant level. The most probable values for the other parameters in the empirical model are determined by a Levenberg-Marquardt least-squares fit to measured counts with the constant level subtracted (Press *et al.* 1992). Except for mass slots associated with C_6H_6 and C_7H_8 , channels 12-18, 24-30, 39-40, 44, 49-52, 61-62 are also excluded in the background fitting, to avoid contributions from various neutral species in the ambient atmosphere.

Since the signals in the background spectra are relatively low, an accurate determination of the model parameters is sometimes difficult. This is an especially serious concern at high altitudes where the Levenberg-Marquardt least-squares fit occasionally gives unrealistic parameter values for h , Δ , m_0 or w (e.g. negative). Usually, this happens when many channels under consideration have zero counts.

I first consider measurements made at altitudes below 1,000 km and typically binned by 25 km, where values of all the free parameters can be determined accurately. Although the binsize is smaller than the spatial resolution of 56 km for most channels (see Chapter 2), a binned spectrum typically incorporates 2-3 consecutive measurements in any given channel, due to the inclination of the spacecraft trajectory with respect to vertical. The empirical fitting for each flyby is performed on the mass spectra with count rates in all channels interpolated to a common altitude grid defined by channel 26, i.e. the main peak channel of C_2H_2 (see Table 3.1).

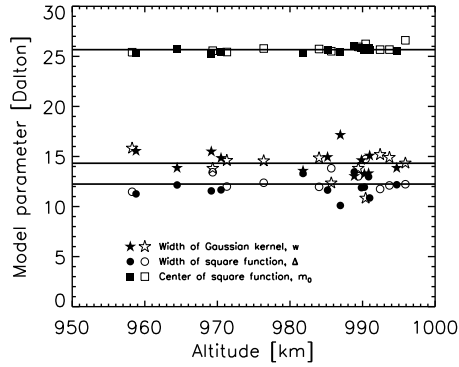


Figure 3.8 The width of the Gaussian kernel, the center and width of the square function for the empirical model fitting of the background mass spectra. Solid and open symbols stand for inbound and outbound, respectively. These parameters appear to be constant with altitude. The mean values, given by the dashed lines, are 14.2 for the width of the Gaussian kernel, 25.7 for the center of the square function, and 12.2 for the width of the square function. These mean values are fixed in the empirical background model fitting.

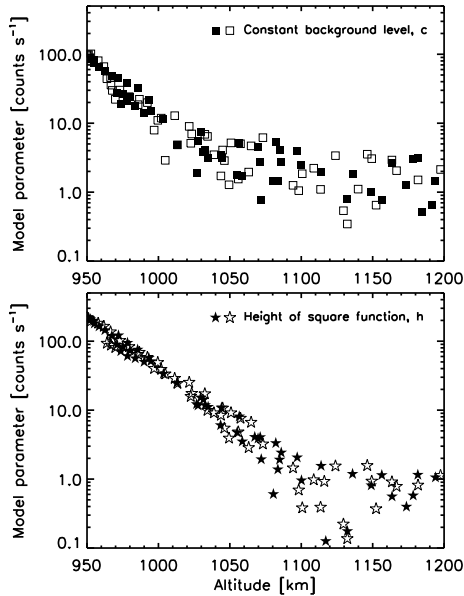


Figure 3.9 The constant level (squares) and the height of the square function (five-stars) for the empirical model fitting of the background mass spectra. Solid and open symbols stand for inbound and outbound, respectively. These parameters show strong altitude variations.

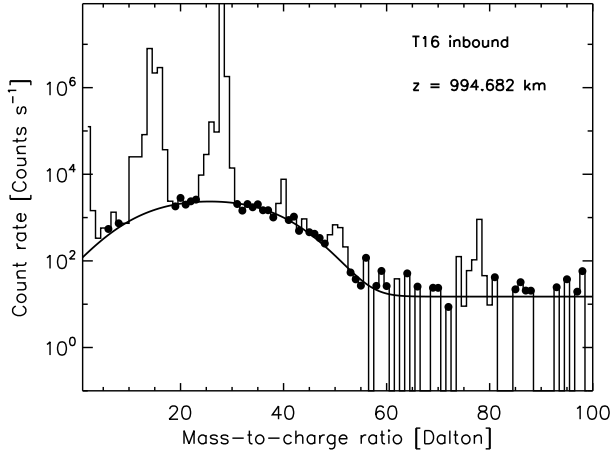


Figure 3.10 The empirical model fitting of the background spectrum for the inbound T16 data at an altitude of 994.7 km. The histogram shows the observed mass spectrum, with the solid line giving the best-fit background model. The model fitting is based on counts in channels not affected by neutral constituents in the ambient atmosphere, represented by the solid circles.

I present in Fig. 3.8 the variations of the parameters w , Δ and m_0 , which show that their values are approximately independent of altitude. This suggests us to adopt the mean values of w , Δ and m_0 as fixed model parameters at all altitudes and for all flybys. Specifically, I adopt $w = 14.2 \pm 1.3$, $\Delta = 12.2 \pm 1.0$ and $m_0 = 25.7 \pm 0.3$, where all values are in units of Dalton and the 1σ errors represent standard deviations. With these fixed values, I run Levenberg-Marquardt least-squares fit again on the unbinned spectra to determine the values for the remaining parameter, h at each altitude. The variations of this parameter, as well as the constant level, c are presented in Fig. 3.9, both of which show strong altitude dependence. It also appears that both parameters tend to be constant with altitude above $\sim 1,100$ km. A typical example of the empirical background fitting is shown in Fig. 3.10, for the inbound T16 observation at an altitude of ~ 995 km. Values for w , Δ and m_0 are fixed in the fitting, whereas c and h are treated as free parameters. Such a scheme is adopted throughout this work.

The errors associated with the background signals are estimated with a Monte-Carlo method, in which the mean values and uncertainties of all free parameters in

the empirical background fitting are estimated from the spread of points in Fig. 3.8 and 3.9, taking into account possible altitude variations. By choosing random values of model parameters, I calculate 1,000 random background spectra at any given altitude. The spread of these model counts is used to represent the uncertainties associated with the background model. This procedure is repeated for all altitudes between 950 and 1,200 km, which essentially constructs an error matrix depending on both altitude and M/Z .

Finally, I discuss briefly the potential sources for the background spectra. Titan's upper atmosphere is, most of the time, within Saturn's corotating plasma. Although reduced by an external tantalum shield, the highly energetic particles in the ambient magnetosphere can produce a residual count rate on the INMS detector which is not separated by quadrupole selection according to M/Z (Waite *et al.* 2004). This is likely the cause of the constant background level incorporated in our empirical model. The thermal background noise in the INMS detectors is not relevant here, since it is much weaker, producing signals of order 1 count min^{-1} , and it should not vary significantly with altitude (Waite *et al.* 2004). The origin for the broad structure centered near channel 25 is still unknown. The leakage of N_2^+ ions from mass channel 28 is not a concern, since the shape of the background spectra is too broad to be interpreted by overflow (see Chapter 3.6). In this thesis, I will not attempt to provide a physical model for the broad distribution of background counts described here. However, it is worth emphasizing that such a model should be able to account for both the shape and altitude dependence of the background spectra. Also, in Fig. 3.8 and 3.9, the solid and open symbols represent background model parameters obtained from inbound and outbound mass spectra, respectively. No systematic difference between inbound and outbound appears to be present. This indicates that the parent molecules responsible for the background counts are not involved in wall effects (see Chapter 5.1).

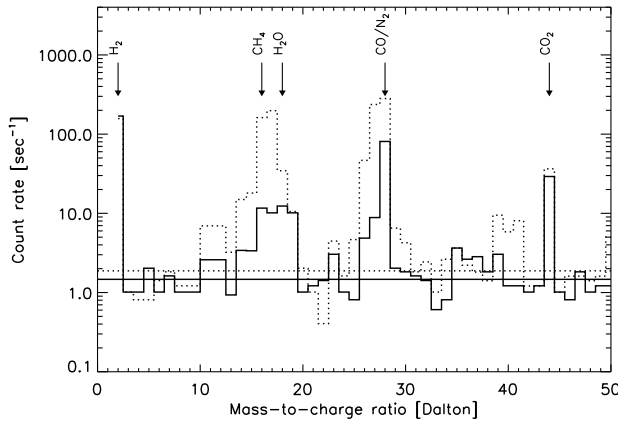


Figure 3.11 The mean mass spectra obtained between 10,000 km and 20,000 km for the inbound (solid) and outbound (dotted) T18 flyby. These spectra are produced by the residual gases in the INMS chamber, including H_2 , CH_4 , H_2O , N_2 , CO and CO_2 (marked by arrows). The horizontal straight lines indicate the constant background levels, corresponding to the mean values calculated from counts in channels not occupied by residual gases.

3.5.2 Residual gas in the INMS chamber

In addition to the empirical background model described above, residual gases in the INMS antechamber represent an additional channel-specific background that must be subtracted. As compared to the empirical background model which occupies all mass channels and shows strong altitude variations as illustrated in Fig. 3.9, the residual gases in the chamber tend to create constant background signals in mass slots occupied by neutral species, including H_2 , CH_4 , H_2O , N_2 , CO , CO_2 and probably other inert species (Waite *et al.* 2004). An example for the inbound T18 flyby is given in Fig. 3.11, which shows the mean inbound (solid line) and outbound (dotted line) mass spectra obtained by averaging counts between 10,000 km and 20,000 km. Peaks associated with H_2 , CH_4 , H_2O , N_2 , CO and CO_2 are marked with arrows. At such far distances from Titan, the densities of all species in the ambient exosphere become vanishingly small, with the only possible source for the observed counts being residual gas in the INMS chamber.

To obtain accurate densities of neutral constituents in Titan's atmosphere, the

contributions from these residual gases are subtracted from the observed mass spectra (e.g. Cui *et al.* 2008). Inbound and outbound spectra are treated separately, because Fig. 3.11 shows that the residual signals recorded during the outbound legs are much stronger than those recorded during the inbound legs. This is expected to be a result of the wall effects which will be discussed in a more general context in Chapter 5.1. For the T25 flyby and the outbound T37 flyby during which no INMS measurements were made above $\sim 10,000$ km, the residual spectra averaged over all the other flybys are adopted. The residual spectrum shows a constant background level, indicated by the horizontal straight lines in Fig. 3.11, which are calculated as the mean values of counts in those channels not occupied by possible residual gases. These are analogous to the constant term, c in Eqn. 7, and need to be subtracted from the spectra of the residual gases before removing their contributions to the observed INMS spectra. It is interesting to note that the background level of order 1 count s^{-1} shown in Fig. 3.11 is consistent with the asymptotic value of the constant background above $\sim 1,100$ km shown in the upper panel of Fig. 3.9. This implies a common origin for both background signals, which is likely to be the energetic particles in Saturn's magnetosphere, as mentioned above.

3.6 Channel crosstalk

The INMS quadrupole mass analyzer consists of four rods mounted in a mechanical assembly and excited by radio frequency (RF) and direct current (DC) potentials (Waite *et al.* 2004). While the combination of the RF amplitude and frequency (either 3.57 MHz and 1.64 MHz) determines the transmitted M/Z , the resolution is controlled by the ratio of the DC and RF amplitudes (Waite *et al.* 2004). The finite resolving capability indicates that the incident ions are never separated perfectly according to M/Z , but rather produce a spectrum that spills over slightly into adjacent channels. An example is given in Fig. 3.12, which shows the mass spectrum for the N_2 reference gas obtained during the FU characterization. While the peaks at channels 28 and 29 reflect contributions from N_2 and its isotope $^{14}N^{15}N$, the residual

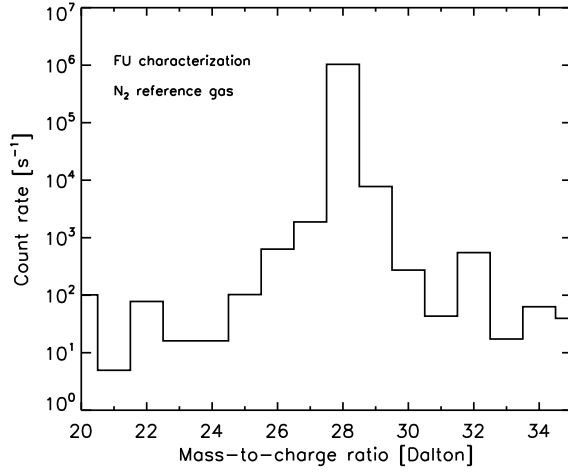


Figure 3.12 The mass spectrum for the N_2 reference gases used for FU characterization. Only the portion near $M/Z \sim 28$ is shown. While counts in channels 28 and 29 are clearly associated with N_2 and $^{14}\text{N}^{15}\text{N}$, the residual counts in surrounding channels are interpreted as a result of the crosstalk effect. The minor peak at channel 32 is caused by O_2 impurities in the calibration chamber.

counts at surrounding channels (especially channel 27) are interpreted by channel crosstalk. Notice that the minor peak at channel 32 is likely to be caused by O_2 impurities in the calibration chamber.

In principle, the FU spectrum for the N_2 reference gas allows us to characterize the deconvolution kernel that can be used to correct for crosstalk in an observed spectrum. In more detail, I find that with the contribution from $^{14}\text{N}^{15}\text{N}$ taken into proper account, a Voigt kernel provides a reasonable fit to the spectrum in Fig. 3.12. However, when I adopt such a kernel to deconvolve the real INMS spectra, the counts in channel 27 turn out to be negative in most cases. This indicates that the overflow of counts from channel 28 to 27 is overestimated by the Voigt kernel derived from the N_2 reference gas. Therefore I expect that the correction for crosstalk may strongly depend on the pressure or density of the measured gas, and the reference N_2 spectrum cannot be used to correct for channel crosstalk in the observed INMS spectra.

Based on the data shown in Fig. 3.12, I estimate that the overflow of counts

from channel 28 to 27 is approximately 0.15%. Unfortunately, this means that in a Titan spectrum, the counts in channel 27 due to crosstalk are significantly higher than that produced by the ambient HCN molecules, adopting a typical mixing ratio of 2×10^{-4} in Titan's thermosphere (Vuitton *et al.* 2006) and with the possible pressure dependence of crosstalk ignored. This channel will be excluded in the following spectral analysis, which prevents us from determining the HCN abundance in Titan's atmosphere. The overflow of counts from channel 28 to more distant channels such as channel 26 is ignored, since the effect of crosstalk is usually within 1 amu (Waite *et al.* 2004). In fact, if I adopt the Voigt kernel to fit the pure N₂ spectrum in Fig. 3.12, I obtain a best-fit value for the kernel width of ~ 0.3 amu.

The correction for crosstalk is not important for other species. As an example, I estimate that the counts in channel 39 caused by overflow from channel 40 are about 0.1% of those caused by the ambient atmosphere. Here, I assume that the channel 40 count is due to ⁴⁰Ar, with a typical mixing ratio of 5×10^{-6} (Yelle *et al.* 2008), and that channel 39 count is due to CH₃C₂H, with a typical mixing ratio of 1×10^{-5} (Wilson & Atreya 2004). I have also used the fact that the ⁴⁰Ar sensitivity at channel 40 is about 50% higher than the CH₃C₂H sensitivity at channel 39. The difference in the ram enhancement factors for these two species is ignored for simplicity. I will not correct for the overflow from channel 28 to 29 for the same reason, i.e. the counts caused by the ambient ¹⁴N¹⁵N molecules are much higher than those due to crosstalk.

CHAPTER 4

SINGULAR VALUE DECOMPOSITION OF THE NEUTRAL MASS SPECTRA

4.1 Basic algorithm

The density determination of neutral constituents in Titan's upper atmosphere is complicated by the fact that the counts in a particular mass channel are likely to be contributed by more than one species. This is a result of the overlapping cracking patterns for various species present on Titan. In general, it can be shown that

$$c_i = \sum_{j=1}^N S_{i,j} n_j, \quad (4.1)$$

where $i = 1, 2, \dots, M$, $j = 1, 2, \dots, N$, with M and N being the total numbers of the mass channels and neutral species included in the spectral analysis. In Eqn. 4.1, c_i is the measured count rate in channel i , n_j is the density of the neutral species j , and $S_{i,j}$ represents the element of the sensitivity matrix which has been multiplied by the appropriate ram enhancement factor (see Chapter 3.2). This is essentially a problem of solving the linear algebraic equations for n_j 's. In my problem, the number of equations (M) is always larger than the number of unknowns (N), which implies that I have to solve for n_j 's in a minimum χ^2 sense. Many techniques are available for such a problem, and I adopt specifically the method of Singular Value Decomposition (SVD) to obtain the most probable densities, n_j 's for all species. The SVD decomposition is based on the following theorem in linear algebra: Any $M \times N$ matrix \mathbf{S} whose number of rows M is greater than or equal to its number of columns N , can be expressed as the product of an $M \times N$ column-orthogonal matrix \mathbf{U} , an $N \times N$ diagonal matrix \mathbf{W} with positive or zero elements, and the transpose of an $N \times N$ orthogonal matrix \mathbf{V} , i.e. $\mathbf{S} = \mathbf{U} \times \mathbf{W} \times \mathbf{V}^T$ (Press *et al.* 1992). With the SVD decomposition applied to the sensitivity matrix and inserted

back into Eqn. 4.1, the solution to n_j 's can be written as

$$n_j = \sum_{k=1}^N \sum_{i=1}^M \left(\frac{u_{ik} c_i}{w_k} \right) v_{jk}, \quad (4.2)$$

where u_{ij} 's and v_{ij} 's are the elements of the matrices \mathbf{U} and \mathbf{V} , w_i 's are the non-zero diagonal elements of \mathbf{W} . Eqn. 4.2 indicates that the solutions to n_j 's are the linear combinations of the column vectors of matrix \mathbf{V} . The associated density errors can be calculated by

$$\sigma_j = \sqrt{\sum_{i=1}^M \left(\sum_{k=1}^N \frac{u_{ik} v_{jk}}{w_k} \right)^2 \tilde{\sigma}_i^2}, \quad (4.3)$$

where σ_j is the density error of species j and $\tilde{\sigma}_i$ is the error of the count rate recorded in channel i . These density errors are associated with counting statistics only, which also include uncertainties caused by correction for saturation and background subtraction (see also Chapter 4.5).

The SVD decomposition, similar to the traditional least square approach, provides the best fit to the desired solutions of number densities. An important virtue of SVD decomposition is that it provides a better understanding of the parameter space, in the sense that the singular values, w_j 's indicate the importance of each column vector of the matrix \mathbf{V} to the overall fit. Specifically, smaller values of w_k indicate that the fit is largely independent of the associated column vectors. This feature is used for eliminating negative densities, as described below.

Three examples of the INMS spectral fits based on the SVD algorithm are given in Fig. 4.1, for the inbound T30 data between 960 and 980 km (upper panel), the inbound T28 data between 1,100 and 1,200 km (middle panel), and the outbound T18 data between 980 and 1,000 km (lower panel), respectively. The solid circles show the INMS measurements, averaged over the specified altitude range for a given flyby. Instrumental effects have been properly removed following the procedures described in Chapter 3, including correction for saturation, removal of thruster firings and background subtraction. The signals in channel 27 are not shown since this channel is not included in the SVD fit due to channel crosstalk. Also shown on Fig. 4.1 are $\pm 1\sigma$ uncertainties due to counting statistics, which also include the uncertainties in

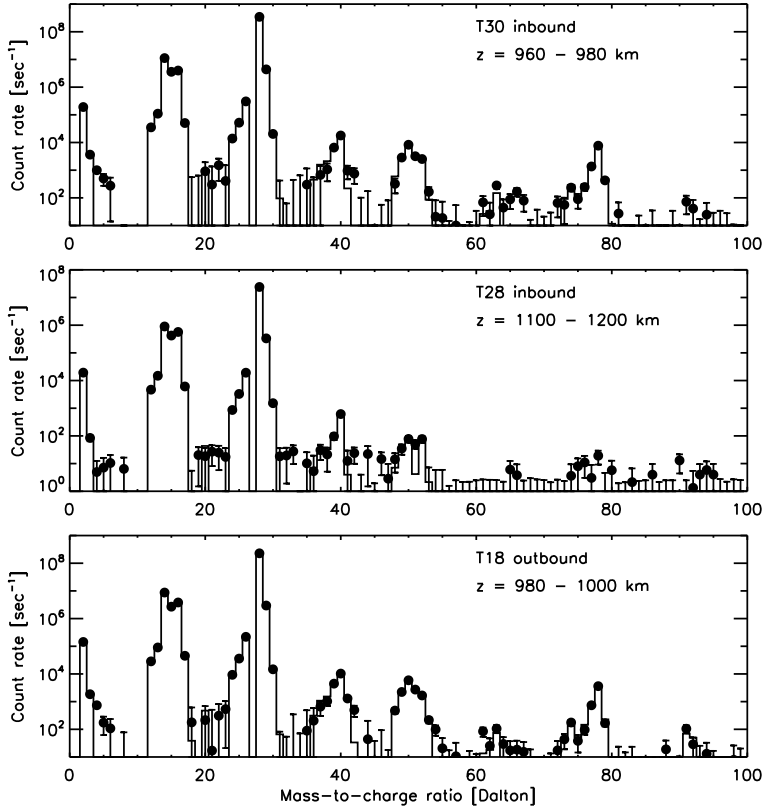


Figure 4.1 The INMS mass spectra averaged between 960 and 980 km for the inbound T30 flyby (upper panel), between 1,100 and 1,200 km for the inbound T28 flyby (middle panel), and between 980 and 1,100 km for the outbound T18 flyby (lower panel). The solid circles give the measurements with 1σ errors due to counting statistics. Instrumental effects have been properly removed. The count rates in channel 27 are not shown since they are excluded in the spectral fitting due to crosstalk. The histograms show the model spectra, which are calculated with calibrated sensitivity values, appropriate ram enhancement factors, and best-fit densities obtained from the SVD algorithm.

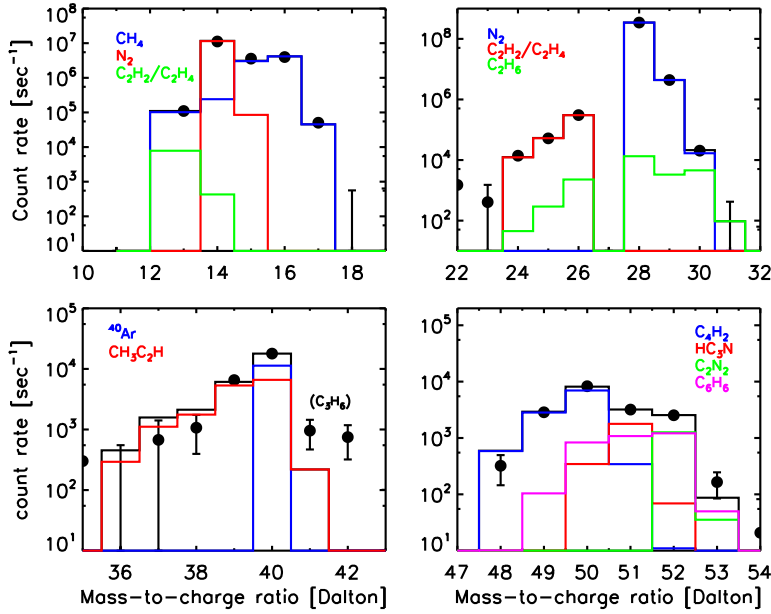


Figure 4.2 The INMS mass spectra averaged between 960 and 980 km for the inbound T30 flyby, near mass channels 16 (upper left), 28 (upper right), 40 (lower left) and 50 (lower right). The solid circles give the measurements with 1σ errors due to counting statistics. The histograms with different colors show the model spectra contributed by different neutral components of Titan's upper atmosphere, with the black ones representing the summation. The deviation between model and observation at channels 41 and 42 might be a signature of C₃H₆ on Titan.

the empirical background models through error propagation. The solid histograms in Fig. 4.1 show the model spectra, that are calculated with calibrated sensitivity values, appropriate ram enhancement factors, and best-fit densities obtained from the SVD fit.

At both high and low altitudes, the model spectra reasonably describe the data. The major features near channels 2, 16, 28, 40, 50 and 78 in the observed spectra are well reproduced by the model. These features are mainly associated with H₂, CH₄, N₂, ⁴⁰Ar/CH₃C₂H, C₄H₂/HC₃N and C₆H₆, as detailed in Fig. 4.2. C₆H₆ produces a minor feature near channel 63, which is also consistent with the model prediction. Small deviations occur at channel 42, especially for spectral analysis at relatively low altitudes (see the lower left panel of Fig. 4.2). However, I notice that

the disagreement here is smaller than 2σ , not as prominent as apparently viewed on the figure since the spectrum is plotted on a logarithmic scale. Significant counts in channel 42 might be a signature of C_3H_6 on Titan. Sensitivity calibration (either FU or REU) has not been made for this species, and thus it is not included in my spectral analysis (see also Chapter 4.4).

Comparing the three panels of Fig. 4.1 immediately shows an interesting feature. Although the densities of any species in general decrease with increasing altitudes, some species show stronger signals in the outbound spectra, irrespective of altitude. An example is C_7H_8 , which is not detected at 3σ significance level during the inbound legs, even at the lowest altitudes. However, the INMS spectrum averaged between 980 and 1,000 km for the outbound T18 flyby (the lower panel of Fig. 4.1) clearly shows a peak near channel 90 which is produced by C_7H_8 molecules. Such a feature can be reasonably explained by the wall effects (Vuitton *et al.* 2008).

4.2 Corrections for negative densities

One mathematical difficulty inherent in the SVD decomposition described above is that the most probable solution to the linear algebraic equations does not guarantee all densities to be positive. Special considerations are required in my spectral analysis to avoid negative values whenever they occur. It should be emphasized that negative densities are not necessarily associated with the statistical uncertainties of measured count rates, especially for minor species in Titan's atmosphere. Rather this is a result of the coupling between several neutral species whose cracking patterns are overlapping.

The negative density problem can be avoided by noticing one important property of small singular values, w_k 's in the SVD decomposition. As mentioned above, small values of w_k indicate that the most probable solution to Eqn. 4.1 is not sensitive to the associated column vectors of matrix \mathbf{V} . In practice, it is free to adjust the solution vector by adding a linear combination of the associated column vectors,

$$\tilde{n}_j = n_j + \sum_k \lambda_k v_{jk}, \quad (4.4)$$

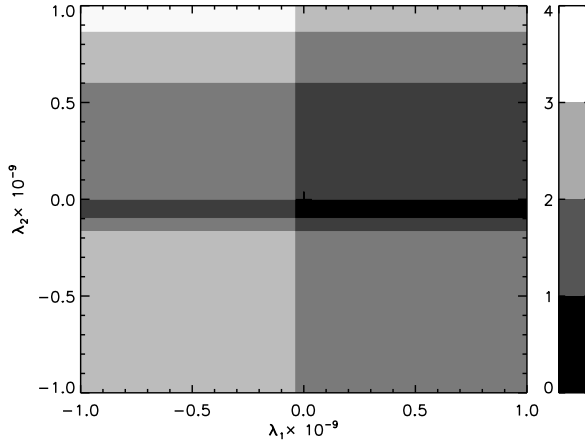


Figure 4.3 Parameter space corresponding to the two smallest singular values in the SVD analysis of the inbound T16 spectrum averaged between 960 and 980 km. Different greyscales indicate the number of species with negative densities. The dark strip corresponds to the region of parameter space where all derived densities are positive. The plus sign marks the location of the lowest χ^2 value in the positive density region.

where n_j is the most probable density of species j obtained from the SVD decomposition which does not guarantee positive, and \tilde{n}_j is the adjusted density which is always positive, λ_k 's are coefficients of the linear combination, treated as free parameters. Since fits to the INMS spectra are typically characterized by two small singular values, the summation in Eqn. 4.4 is always taken over the two associated column vectors of matrix \mathbf{V} . In practice, I search for positive solutions to all n_j 's in the parameter space of λ_1 and λ_2 , and identify the solution with the minimum χ^2 value.

An example is given in Fig. 4.3, which shows the parameter space corresponding to the two smallest singular values, w_1 and w_2 in the SVD analysis of the inbound T16 spectrum averaged between 960 and 980 km. Different greyscales indicate the number of species with negative densities, for different combinations of the linear coefficients, λ_1 and λ_2 . The dark strip indicates the region of parameter space where all derived densities are positive. The plus sign marks the location of the lowest χ^2 value in the positive density region, which corresponds to the final solution of Eqn.

4.1 for the given mass spectrum.

4.3 Major neutral species and their isotopes

4.3.1 Nitrogen

The most abundant neutral species in Titan's upper atmosphere is N_2 , whose presence was predicted by Hunten (1972) and observationally confirmed with the Voyager UVS instrument (Broadfoot *et al.* 1981). The cracking patterns of N_2 and its isotope $^{14}\text{N}^{15}\text{N}$ peak at channels 28 and 29, respectively. However, other neutral species in Titan's atmosphere also contribute to counts in these two channels, e.g. C_2H_4 , C_2H_6 and C_3H_8 . This raises a difficulty in the SVD spectral analysis, in which any small fractional change in the derived densities of N_2 or $^{14}\text{N}^{15}\text{N}$ causes a large variation in the densities of other neutral species. To avoid this, I directly determine the abundances of N_2 and $^{14}\text{N}^{15}\text{N}$ from counts in channels 14, 28 and 29, with all necessary calibrations taken into proper account. The detailed procedure for deriving N_2 densities is described in Müller-Wodarg *et al.* (2008), which is based on $\text{C}^{(2)}$ counts in channel 28 at low altitudes, $\text{C}^{(1)}$ counts in channel 28 at high altitudes, and $\text{C}^{(1)}$ counts in channel 14 between. The procedure for deriving $^{14}\text{N}^{15}\text{N}$ is based on counts in channel 29 only and will not be detailed here. An estimate of the nitrogen isotope ratio, $y_{\text{N}} = n(^{14}\text{N})/n(^{15}\text{N})$ on Titan can thus be determined, from which I can further obtain the ratio of the $^{15}\text{N}^{15}\text{N}$ density to N_2 density from $1/[1 + y(\text{N})]^2$. With the known densities of N_2 as well as its isotopes ($^{14}\text{N}^{15}\text{N}$ and $^{15}\text{N}^{15}\text{N}$), I calculate from their cracking patterns the contributions of these species to channels 14, 15, 28, 29, and 30. These contributions are subtracted from the original mass spectra, and the SVD analysis can then be performed without the difficulty induced by the N_2 density errors. An independent determination of the $^{15}\text{N}^{15}\text{N}$ densities is important, since the abundances of both $^{15}\text{N}^{15}\text{N}$ and C_2H_6 are mainly constrained by counts in the same channel (30), and thus the coupling between these two species in the SVD analysis needs to be untangled.

4.3.2 Methane

The second major species in Titan's thermosphere is CH_4 , whose abundances can be derived accurately from the INMS measurements based on counts in channel 16, except below $\sim 1,100$ km where the $\text{C}^{(1)}$ counts of this channel become saturated and the CH_4 densities are alternatively determined from counts in channels 12 and 13 (see Müller-Wodarg *et al.* 2008 for details). However, the density determination of its isotope, $^{13}\text{CH}_4$ suffers from the contamination of NH_3 , since the densities of both species are mainly constrained by counts in channel 17.

To untangle the coupling between $^{13}\text{CH}_4$ and NH_3 , I apply an adhoc carbon isotope ratio for a given mass spectrum. This is then used to estimate the $^{13}\text{CH}_4$ density from the CH_4 measurement, independent of the actual count rate in channel 17. Here I need to incorporate the vertical variation of the isotope ratio, as a result of diffusive separation since $^{13}\text{CH}_4$ is slightly heavier than CH_4 (Lunine *et al.* 1999). The most recent determination of the carbon isotope ratio on Titan gives $y(\text{CH}_4) = n(\text{CH}_4)/n(^{13}\text{CH}_4) = 82.3 \pm 0.1$, based on Huygens Gas Chromatography Mass Spectrometer (GCMS) measurements made between 6 and 18 km (Niemann *et al.* 2005). Approximating this value as the carbon isotope ratio at the homopause, which I place at an altitude of 850 km (Yelle *et al.* 2008), it is easy to show that $y(\text{CH}_4) = n(\text{CH}_4)/n(^{13}\text{CH}_4) = 97.1$ at an altitude of 1,150 km, where I have ignored eddy mixing above the homopause as well as CH_4 escape for the moment.

The carbon isotope ratio above the homopause can also be estimated directly from the INMS measurements. The upper panel of Fig. 4.4 shows the mean CH_4 (solid lines) and $^{13}\text{CH}_4$ (dashed lines) densities as a function of altitude. The inbound and outbound profiles are given separately by the thin and thick lines, respectively. The $^{13}\text{CH}_4$ densities in Fig. 4.4 are calculated from counts in channel 17, ignoring contribution from NH_3 for the moment. The densities shown in the figure are obtained by averaging over all flybys, which should effectively remove possible horizontal and diurnal variations. The CH_4 distribution is symmetric about C/A, indicating that wall effects are not important for this species. The same feature

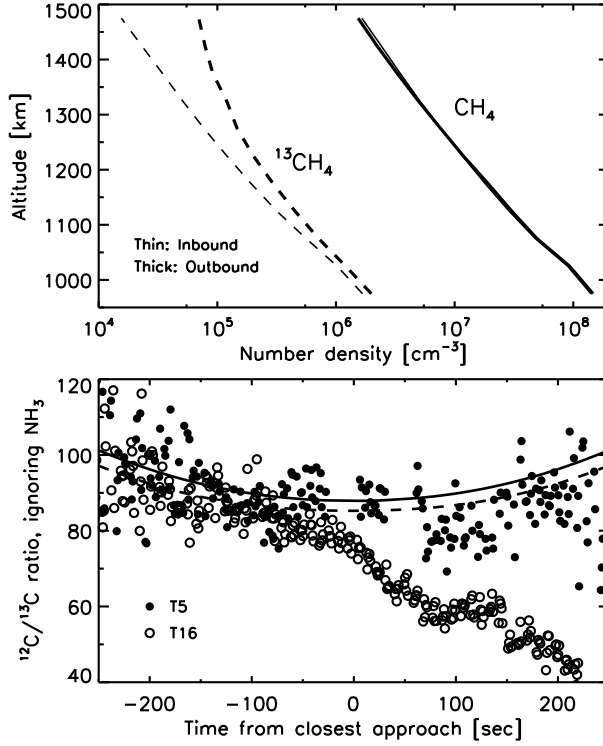


Figure 4.4 Upper panel: the mean density profiles of CH₄ (solid lines) and ¹³CH₄ (dashed lines) averaged over all flybys, with contribution from NH₃ ignored. The thin and thick lines give the inbound and outbound profiles separately. Lower panel: the observed ¹²C/¹³C ratio as a function of time from C/A, ignoring the contribution from NH₃. Two extreme cases are shown, one for the T5 flyby with the maximum C/A altitude of 1,027 km in my sample, and the other for the T16 flyby with the minimum C/A altitude of 950 km. The solid and dashed lines give the ¹²C/¹³C ratio adopted for the T5 and T16 flybys in my SVD analysis (see text for details).

should in principle be observed for $^{13}\text{CH}_4$ as well, since both species have similar chemical properties. The asymmetric distribution of $^{13}\text{CH}_4$ therefore implies that the counts in channel 17 are actually contributed by both $^{13}\text{CH}_4$ and NH_3 , of which the latter is subject to wall effects and the former has a symmetric distribution about C/A similar to the observations of CH_4 . The lower panel of Fig. 4.4 further shows the observed $^{12}\text{C}/^{13}\text{C}$ ratio, ignoring the contributions from NH_3 to counts in channel 17. Two extreme cases are given, one for the T5 flyby with the maximum C/A altitude of 1,031 km in my sample, and the other for the T16 flyby with the minimum C/A altitude of 950 km. The $^{12}\text{C}/^{13}\text{C}$ ratio does tend to the same constant level above $\sim 1,100$ km for the inbound legs of both flybys, suggesting that the contributions from NH_3 are negligible for these measurements. The very low $^{12}\text{C}/^{13}\text{C}$ ratios obtained during the outbound legs, especially for the T16 flyby, are consistent with the suggestion that a significant fraction of the channel 17 counts are from NH_3 molecules. These counts from NH_3 appear to increase significantly with time from C/A, consistent with my assumption that the wall effects are important for this species.

Based on the above discussions, I estimate the carbon isotope ratio in Titan's thermosphere by averaging all observed $n(\text{CH}_4)/n(^{13}\text{CH}_4)$ values between 1,100 and 1,200 km during the inbound legs of all flybys. This gives $n(^{12}\text{C})/n(^{13}\text{C}) = 93.3 \pm 0.1$ at a mean altitude of 1,150 km, which is consistent with the value of 97.1 inferred from the GCMS measurements when corrected for diffusive separation. Throughout my SVD analysis, I evaluate the $^{12}\text{C}/^{13}\text{C}$ ratio in Titan's thermosphere, adopting a diffusion model that is in agreement with both the GCMS and INMS results. Such a model will be detailed in Chapter 5.2.1, which also includes the effect of CH_4 escape. The $^{12}\text{C}/^{13}\text{C}$ ratios calculated from the diffusion model are shown in the lower panel of Fig. 4.4, for the T5 (solid line) and T16 (dashed line) flybys. The variation of this ratio shown in the figure is associated with diffusion/escape only. With the presumed density ratio of CH_4 to $^{13}\text{CH}_4$, I treat in the SVD analysis the combined $\text{CH}_4/^{13}\text{CH}_4$ gas, with the sensitivities calculated from Eqn. 3.9-3.16. Finally, I emphasize that in this study, the presence of NH_3 in Titan's upper atmosphere is

implied from the distribution of channel 17 counts with respect to time from C/A in the context of wall effects. The detection of NH_3 on Titan will be revisited in Chapter 5.2.3.

4.4 Identification of neutral constituents

One of the key problems in the spectral analysis is to decide what neutral species should be included in the SVD fit described in Chapter 4.1. The candidate neutrals include N_2 , CH_4 , H_2 , C_2H_2 , C_2H_4 , C_2H_6 , C_3H_4 , C_3H_8 , C_4H_2 , C_4H_6 , C_6H_6 , C_7H_8 , NH_3 , HCN , CH_3CN , HC_3N , $\text{C}_2\text{H}_3\text{CN}$, $\text{C}_2\text{H}_5\text{CN}$, C_2N_2 , H_2O , CO_2 and ^{40}Ar . The isotopes of N_2 , CH_4 , H_2 and ^{40}Ar are also considered, including $^{14}\text{N}^{15}\text{N}$, $^{15}\text{N}^{15}\text{N}$, $^{13}\text{CH}_4$, HD and ^{36}Ar . The choice of the above species list is based on (1) results from recent nadir observations made with the Cassini Composite Infrared Spectrometer (CIRS) (Coustenis *et al.* 2007); (2) predictions from existing photochemical models of Titan's neutral upper atmosphere (e.g. Wilson & Atreya 2004, Lavvas *et al.* 2008a, b); and (3) available FU/REU sensitivity calibrations (therefore I exclude C_3H_6 though its presence is suggested by the counts in channels 41 and 42, see Chapter 4.1). For a historical description of the identification of various neutral species on Titan, see Waite *et al.* (2004). It should also be pointed out that the CIRS spectra characterize regions in Titan's stratosphere, which are far below the altitude range probed by the INMS. Therefore observational evidence for a given species in the CIRS spectra does not necessarily indicate the presence of the same species in the INMS spectra.

In the above list, several neutral species are excluded in my SVD analysis for various reasons, which are detailed as follows. (1) C_3H_4 can be either $\text{CH}_3\text{C}_2\text{H}$ (methylacetylene) or $\text{CH}_2\text{C}_2\text{H}_2$ (allene), whose cracking patterns are similar but not exactly identical. However, recent Cassini/CIRS nadir observations show evidence for the $\text{CH}_3\text{C}_2\text{H}$ ν_9 emission band, whereas signatures for the ν_{10} and ν_{11} bands of $\text{CH}_2\text{C}_2\text{H}_2$ appear to be absent in the CIRS spectra (Coustenis *et al.* 2007). Theoretically, $\text{CH}_3\text{C}_2\text{H}$ is more stable than $\text{CH}_2\text{C}_2\text{H}_2$, and can be formed indirectly

through collisional isomerization of $\text{CH}_2\text{C}_2\text{H}_2$ (Wilson & Atreya 2004). (2) No direct detection of $\text{C}_2\text{H}_5\text{CN}$ has been reported to date, though it has been predicted from the INMS OSI spectra (Vuitton *et al.* 2007). More important, the cracking pattern of $\text{C}_2\text{H}_5\text{CN}$ peaks at channel 28, which is dominated by counts from N_2 . This implies that the $\text{C}_2\text{H}_5\text{CN}$ densities, even if this species is present in Titan's upper atmosphere, are difficult to be constrained directly with the INMS data. (3) The presence of HCN has been confirmed by Cassini/CIRS observations through its 713 cm^{-1} emission band (Coustenis *et al.* 2007). In the context of INMS measurements, the abundances of HCN are mainly constrained by counts in channel 27. However, this channel is ignored in this study since there is no solid way to correct for crosstalk near channel 28 (see Chapter 3.6). For the reasons above, $\text{CH}_2\text{C}_2\text{H}_2$, HCN and $\text{C}_2\text{H}_5\text{CN}$ are excluded from my spectral analysis.

C_2H_2 and C_2H_4 present an additional difficulty in the SVD analysis. Their cracking patterns suggest that in principle, their abundances can be constrained from counts in channels 24-26. The signals in channels 12-14 cannot be reliably used because these channels are dominated by CH_4 . For channels 24-26, the branching ratios of C_2H_2 are approximately a factor of 3 higher than those of C_2H_4 , i.e. their relative signals in these channels remain nearly the same. This indicates that in practice, the counts in channels 24-26 can only be used to constrain the linear combination of C_2H_2 and C_2H_4 densities in the form of $3n(\text{C}_2\text{H}_2) + n(\text{C}_2\text{H}_4)$, where I have ignored the small difference in their ram enhancement factors. In the following spectral analysis, rather than treating the two species separately, I investigate an *imaginary* species with densities set equal to $\frac{3}{4}n(\text{C}_2\text{H}_2) + \frac{1}{4}n(\text{C}_2\text{H}_4)$ on Titan. It is easily seen that the sensitivities of this species should be set as four times the C_2H_4 values.

Throughout my analysis, those species with relatively high abundances on Titan are always incorporated, including N_2 , CH_4 , H_2 , C_2H_2 , C_2H_4 and their isotopes. Notice that the contributions from N_2 , $^{14}\text{N}^{15}\text{N}$ and $^{15}\text{N}^{15}\text{N}$ are determined independently and subtracted from the raw data before the SVD fit is applied, the CH_4 to $^{13}\text{CH}_4$ density ratio is fixed with an adhoc value which takes into account diffusive

separation as well as escape, and the inclusion of C_2H_2 and C_2H_4 is through the linear combination of $\frac{3}{4}n(\text{C}_2\text{H}_2) + \frac{1}{4}n(\text{C}_2\text{H}_4)$. The remaining minor species are more difficult to detect at high altitudes. For each of these species, whether it is included in the spectral fit depends on the signal-to-noise ratio of the count rate in its main channel. In more detail, I adopt the following scheme: (1) if $c_{18} > 3\sigma_{18}$, then H_2O is included; (2) if $c_{30} > 3\sigma_{30}$ (with the contribution from $^{15}\text{N}^{15}\text{N}$ subtracted), then C_2H_6 is included; (3) if $c_{36} > 3\sigma_{36}$, then ^{36}Ar is included; (4) if $c_{39} > 3\sigma_{39}$, then $\text{CH}_3\text{C}_2\text{H}$ is included; (5) if $c_{40} > 3\sigma_{40}$, then ^{40}Ar is included; (6) if $c_{41} > 3\sigma_{41}$, then CH_3CN is included; (7) if $c_{43} > 3\sigma_{43}$, then C_3H_8 is included; (8) if $c_{44} > 3\sigma_{44}$, then CO_2 is included; (9) if $c_{50} > 3\sigma_{50}$, then C_4H_2 is included; (10) if $c_{51} > 3\sigma_{51}$, then HC_3N is included; (11) if $c_{52} > 3\sigma_{52}$, then C_2N_2 is included; (12) if $c_{53} > 3\sigma_{53}$, then $\text{C}_2\text{H}_3\text{CN}$ is included; (13) if $c_{54} > 3\sigma_{54}$, then C_4H_6 is included; (14) if $c_{78} > 3\sigma_{78}$, then C_6H_6 is included; (15) if $c_{91} > 3\sigma_{91}$, then C_7H_8 is included. In all the above expressions, c_i and σ_i represent the count rate in channel i and its uncertainty. Such a scheme is aimed at minimizing the coupling between the cracking patterns of all species. In general, the above inequalities imply that a particular species is considered to be present and included in the spectral analysis, only when it is detected at more than 3σ significance level based on its signal in one of its main channels. On the other hand, if a species is below the detection limit, I estimate an upper limit density based on the 3σ uncertainty of count in the same channel.

I notice that the cracking pattern of C_3H_8 peaks at both channels 43 and 44. Therefore in principle, CO_2 does not need to be included in the spectral analysis, if I assign most of the channel 44 counts to C_3H_8 . However, in a typical mass spectrum, the ratio of the channel 44 count to channel 43 count is much higher than the corresponding ratio in the C_3H_8 cracking pattern. This implies the presence of CO_2 in Titan's upper atmosphere. Therefore I include both C_3H_8 and CO_2 in my spectral analysis, with the former marked by counts in channel 43 and the latter marked by counts in channel 44.

The situation for NH_3 is more complicated, since there is no single channel of which the count rate is mainly contributed by this species. Note that $^{13}\text{CH}_4$

contributes to a significant fraction of the channel 17 counts in all cases. Here I adopt a scheme in which the SVD fit is applied to a given spectrum with NH_3 always included. However, in many cases the derived NH_3 density is too low to justify the presence of NH_3 at more than 3σ significance level. In such cases, I simply replace the derived NH_3 density with an upper limit evaluated from the density error tripled.

4.5 Error analysis

The density determination based on the SVD analysis described above relies on the most probable sensitivity values either directly taken from the FU measurements or scaled from the REU measurements. Therefore the errors given directly by the SVD fits are associated with counting statistics only, which also include uncertainties associated with background subtraction. Here I use a Monte-Carlo technique to estimate the extra uncertainties related to sensitivity calibration (see Chapter 3.1). By comparing with uncertainties due to counting statistics, I can then identify the dominant source of errors in the derived densities or mixing ratios for all species.

I start from the relative uncertainties of peak sensitivities listed in Table 3.1, and I further include uncertainties due to calibration of cracking patterns, as detailed in Chapter 3.1.3. For an individual flyby, either inbound or outbound, I perform 1,000 SVD fits to the mean mass spectrum obtained by averaging over a given altitude bin. Random choices of the sensitivity values are adopted in these SVD fits, following a Gaussian distribution with the standard deviation taken from the combined uncertainty of peak sensitivity and cracking pattern. For any given flyby, the densities obtained from these random samples are used to evaluate the uncertainties due to sensitivity calibration for all neutral species. I detail in Table 4.1 the relative uncertainties of mixing ratios obtained for two representative mass spectra, one for the inbound T16 spectrum between 980 and 1,000 km, and the other one for the inbound T36 spectrum between 1,050 and 1,100 km. Uncertainties due to sensitivity calibration and counting statistics are given separately for comparison.

Table 4.1 Relative uncertainties due to counting statistics and sensitivity calibration. In cases where the upper limits are obtained for the mixing ratios of several minor species, I only give the relative uncertainties due to sensitivity calibration, calculated as the standard deviations of upper limits from 1,000 random realizations.

Species	T16 (980-1,000 km)		T36 (1,050-1,100 km)	
	Counting	Sensitivity	Counting	Sensitivity
N ₂	4.0×10^{-4}	1.4×10^{-3}	6.7×10^{-4}	2.0×10^{-3}
¹⁴ N ¹⁵ N	2.5×10^{-3}	4.5×10^{-2}	4.1×10^{-3}	4.3×10^{-2}
CH ₄	1.8×10^{-3}	4.4×10^{-2}	2.4×10^{-3}	4.8×10^{-2}
H ₂	1.1×10^{-2}	3.5×10^{-2}	1.8×10^{-2}	5.1×10^{-2}
HD	1.3×10^{-1}	5.0×10^{-2}	...	5.4×10^{-2}
C ₂ H ₂ /C ₂ H ₄	1.0×10^{-2}	4.5×10^{-2}	1.6×10^{-2}	5.0×10^{-2}
C ₂ H ₆	1.2×10^{-1}	1.4×10^{-1}	1.8×10^{-1}	2.1×10^{-1}
CH ₃ C ₂ H	4.0×10^{-1}	4.6×10^{-2}	2.9×10^{-1}	6.4×10^{-2}
C ₃ H ₈	...	5.8×10^{-2}	...	8.9×10^{-2}
C ₄ H ₂	2.2×10^{-1}	6.3×10^{-2}	2.6×10^{-1}	7.1×10^{-2}
C ₄ H ₆	...	1.1×10^{-1}	...	1.7×10^{-1}
C ₆ H ₆	1.2×10^{-1}	6.6×10^{-2}	...	1.1×10^{-1}
C ₇ H ₈	...	7.8×10^{-2}	...	1.2×10^{-1}
NH ₃	4.3×10^{-2}	1.9×10^{-1}	2.5×10^{-2}	1.6×10^{-1}
HC ₃ N	3.9×10^{-1}	8.4×10^{-2}	...	6.1×10^{-2}
CH ₃ CN	...	5.8×10^{-2}	...	6.9×10^{-2}
C ₂ H ₃ CN	...	1.0×10^{-1}	...	1.2×10^{-1}
C ₂ N ₂	4.7×10^{-1}	1.1×10^{-1}	...	5.0×10^{-2}
H ₂ O	...	4.7×10^{-2}	...	5.8×10^{-2}
CO ₂	...	6.2×10^{-2}	...	6.3×10^{-2}
⁴⁰ Ar	1.2×10^{-1}	6.7×10^{-2}	1.4×10^{-1}	8.1×10^{-2}
³⁶ Ar	...	4.2×10^{-2}	...	5.9×10^{-2}

For relatively abundant constituents in Titan's upper atmosphere, such as CH₄, H₂ and C₂H₂/C₂H₄, uncertainties due to counting statistics are usually smaller than those due to sensitivity calibration. This is expected as a result of the high signal-to-noise ratios of counts in their main channels. On the contrary, for most of the minor constituents, the counting statistics is the dominant source of error in their derived mixing ratios. As the most abundant species, the uncertainties of the N₂ mixing ratio are not strongly affected by sensitivity calibration. This is because the total density varies in response to the N₂ density, leading to a small change of the N₂ mixing ratio. However, the uncertainties of the N₂ number density are still on $\sim 5\%$ level due to sensitivity calibration. For most species, the relative uncertainties due to sensitivity calibration are typically $\sim 10\%$ at different altitudes, while those due to counting statistics span a considerably large range from smaller than 1% to over 40%, and may vary significantly with altitude.

CHAPTER 5

NEUTRAL GAS DISTRIBUTION IN TITAN'S THERMOSPHERE

For a given flyby, the fully calibrated count rates in any mass channel are interpolated to the grid of time from C/A defined by channel 26. These interpolated count rates are then divided into several altitude bins, with typical widths of 20-25 km below 1,000 km and 50-100 km above. Throughout my analysis, the inbound and outbound data are treated separately. For minor species, only measurements made below 1,200 km are considered, and their densities (or 3σ upper limits) are obtained following the SVD algorithm described in the previous chapter. To retain the full spatial resolution of the INMS data, for N_2 , CH_4 and H_2 , I adopt their densities directly determined from counts in the main channels (e.g. Müller-Wodarg *et al.* 2008, Cui *et al.* 2008), and I extend the analysis of these species to Titan's exobase at $\sim 1,500$ km. The distribution of these abundant species in Titan's exosphere have been presented in De La Haye *et al.* (2007a) and Cui *et al.* (2008), and will not be discussed here. All errors quoted in this chapter reflect uncertainties associated with both counting statistics and sensitivity calibration (see Chapter 4.5). A total number of 114 individual spectra are analyzed. Among all the density measurements, 970 are upper limits. Most of the upper limits are obtained for minor species at relatively high altitudes during the inbound legs. Especially, for C_3H_8 , C_4H_6 , C_7H_8 , $\text{C}_2\text{H}_3\text{CN}$, CO_2 , H_2O and ^{36}Ar , the SVD fits to most of the observed spectra give 3σ upper limits only.

Each of the density measurements is associated with definite values of altitude, latitude, longitude, local solar time and time from C/A. The combination of all the densities and upper limits provides information on the vertical distribution and horizontal/diurnal variations of all neutral constituents in Titan's upper atmosphere above 950 km. The variations of neutral species with time from C/A do not necessarily provide information on the ambient atmosphere, but reflect whether wall

effects are important. An investigation of possible wall effects is necessary for justifying that the derived densities are associated with the ambient atmosphere rather than processes within the instrument. In this chapter, I start with a discussion of the wall effects in Chapter 5.1. I present in Chapter 5.2 the globally averaged vertical profiles of various species in Titan's upper atmosphere, followed by a discussion of possible horizontal and/or diurnal variations in Chapter 5.3.

5.1 Wall effects

The INMS chamber walls have a certain probability to adsorb molecules entering the instrument orifice. On one hand, the adsorption of incoming molecules on the chamber walls reduces the actual signals, leading to an underestimate of the atmospheric abundances. On the other hand, these molecules are desorbed from the chamber walls at a later time, leading to overestimated values. The latter effect is enhanced by heterogeneous surface chemistry, such as the recombination of H and C_6H_5 radicals to form C_6H_6 molecules on the chamber walls (Vuitton *et al.* 2008). The recombination of radicals on the chamber walls has been realized in previous analysis of mass spectrometer data, such as been used to derive the densities of atomic N in the Venusian upper atmosphere (Kasprzak *et al.* 1980).

A simple way to examine whether the wall effect is important for a given species is to check the differences between the inbound and outbound density profiles, as done in Cui *et al.* (2008). I divide all measurements into several altitude bins and take averages, with inbound and outbound data treated separately. Since other effects such as horizontal and/or diurnal variations tend to be removed by averaging, the appearance of a density enhancement for the outbound profile is considered as an indication of the wall effects. Alternatively, I can also investigate the density distribution of a given species as a function of time from C/A, in which wall effects are illustrated as an asymmetric distribution about C/A with a positive time shift.

Fig. 5.1 shows the density profiles of N_2 , CH_4 , H_2 and ^{40}Ar measured by INMS, with the solid and dashed lines representing inbound and outbound measurements,

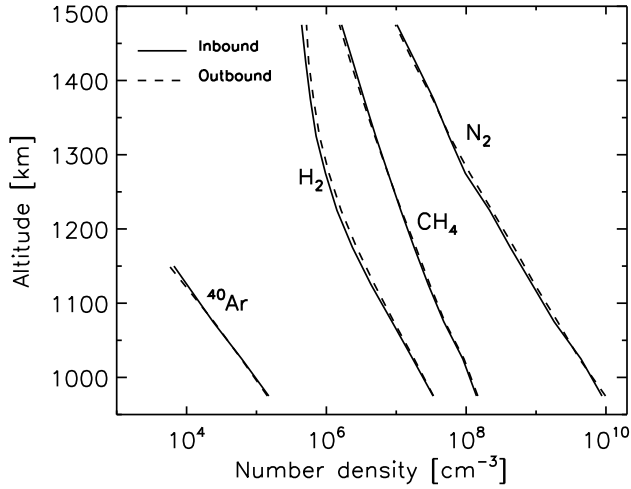


Figure 5.1 The density profiles of N_2 , CH_4 , H_2 and ^{40}Ar , averaged over all flybys. The inbound (solid) and outbound (dashed) profiles are nearly identical, indicating that the wall effects are negligible for these species.

respectively. The CH_4 profiles are the same as those shown in the upper panel of Fig. 4.4. Notice that the ^{40}Ar profiles are obtained by averaging densities derived from SVD fits, while the N_2 , CH_4 and H_2 densities are directly calculated from counts in their main channels. The inbound and outbound profiles are nearly identical for these species as well as their isotopes, indicating that the wall effects are negligible, at least below 1,500 km. For N_2 , CH_4 and H_2 , their densities in the ambient atmosphere are much higher than those involved in wall effects. On the other hand, the wall effect is unlikely to be relevant for ^{40}Ar , which is an inert species. However, it should be pointed out that the outbound densities of N_2 and H_2 may still be affected by wall effects above the exobase (e.g. Cui *et al.* 2008), probably as a result of the recombination of H and N atoms on the chamber walls. Especially I notice that nonthermal escape processes may produce a significant amount of N atoms in Titan's exosphere (Shematovich *et al.* 2001, 2003, Michael *et al.* 2005).

In Fig. 5.2, I show the average density distribution for several minor species, including $\text{C}_2\text{H}_2/\text{C}_2\text{H}_4$, C_4H_2 , C_6H_6 , C_2N_2 , HC_3N and $\text{C}_2\text{H}_3\text{CN}$. Solid and dashed lines are for inbound and outbound profiles, respectively. Notice that the $\text{C}_2\text{H}_2/\text{C}_2\text{H}_4$ profiles represent densities of the *imaginary* species described in Chapter 4.4. Some

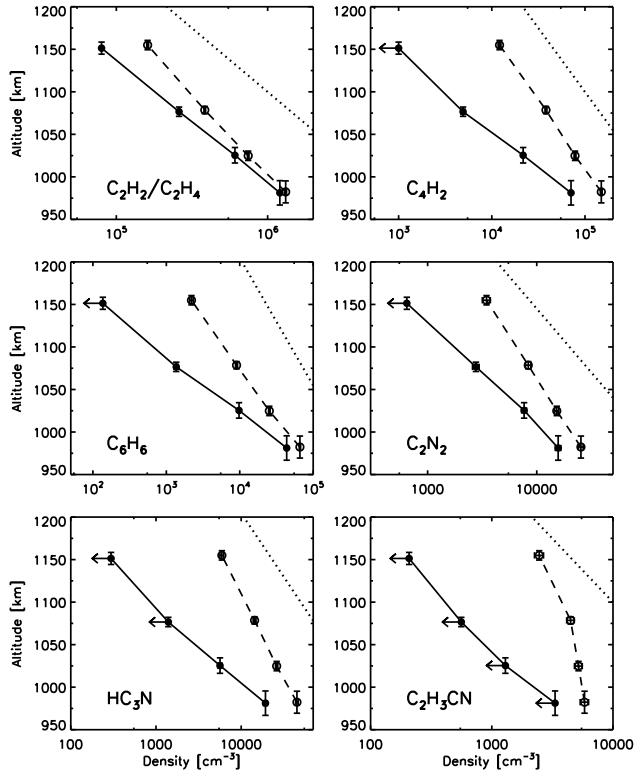


Figure 5.2 The density profiles of $\text{C}_2\text{H}_2/\text{C}_2\text{H}_4$, C_4H_2 , C_6H_6 , C_2N_2 , HC_3N and $\text{C}_2\text{H}_3\text{CN}$, obtained by averaging over all flybys and treating inbound (solid) and outbound (dashed) measurements separately. Leftward arrows indicate upper limit densities. All species show some signature of enhancement for the outbound legs, indicating that wall effects are important.

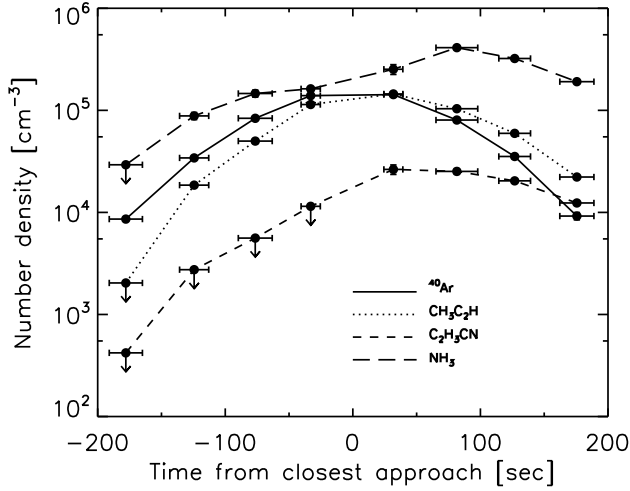


Figure 5.3 Density profiles of ^{40}Ar , $\text{CH}_3\text{C}_2\text{H}$, CH_3CN and NH_3 as a function of time from C/A, obtained by averaging over all flybys. Downward arrows are for upper limit densities. The ^{40}Ar profile serves as a reference which is symmetric about C/A. All other species show enhancement for the outbound legs, indicating that wall effects are important.

minor species are not detected at more than 3σ significance level, and thus only 3σ upper limits can be put on their densities. Here I use the Kaplan-Meier product-limit estimator to evaluate the mean densities as well as the uncertainties in each altitude bin (Feigelson & Nelson, 1985). Such a technique uses both exact measurements and upper limits (termed as right-censored data in the statistical literature). All species in the figure show clear signatures of wall effects, represented by density enhancement observed during the outbound legs. Especially, I notice that significant $\text{C}_2\text{H}_3\text{CN}$ molecules are detected during the outbound legs but absent in the inbound spectra. The dotted lines in Fig. 5.2 give the N_2 density profiles on an arbitrary scale. For all heavy species shown in the figure, their average outbound profiles show scale heights that are comparable with or even greater than the N_2 scale height. These unrealistic features can be interpreted as a result of the wall effects.

In Fig. 5.3, the density profiles for several species are shown as a function of time from C/A, calculated by averaging over all flybys with the Kaplan-Meier product-limit estimator. Downward arrows indicate 3σ upper limits. No scaling has been

applied to correct for the vertical variations. The solid line, corresponding to ^{40}Ar , shows a roughly symmetric distribution about C/A and represents a typical case for which the wall effects are not a concern. All other species, including $\text{CH}_3\text{C}_2\text{H}$, CH_3CN and NH_3 , show enhanced densities measured during the outbound legs. For all species, their profiles peak at a positive time from C/A.

With sufficient information on the details of the adsorption/desorption and surface chemical processes that take place on the INMS chamber walls, it is possible to correct for the wall effects for various species and obtain their true atmospheric densities. Though such a procedure will not be attempted in this study, it is interesting to ask whether the inbound or outbound INMS measurements represent the ambient atmosphere more reasonably. Based on photochemical considerations, Vuitton *et al.* (2008) have shown that the majority of the C_6H_6 molecules recorded by the INMS detector are those formed on the chamber walls through the recombination of C_6H_5 with H. While this study does emphasize the importance of heterogeneous surface chemistry, such a feature cannot be naively generalized to all species since it depends critically on the abundances of the associated radicals in the ambient atmosphere as well as the relevant time constant for the detailed wall chemistry. The example for C_6H_6 may simply be an exception, due to the relatively high C_6H_5 abundances in Titan's upper atmosphere as a result of the large C_6H_6 photolysis rate (Vuitton *et al.* 2008).

If, for most heavy species, the simple processes of adsorption and desorption are more important, it is expected that the way the measured counts are affected by wall effects depends on the fraction of molecules that are adsorbed to the walls (hereafter adsorption probability, denoted as p_{ads}) and the characteristic time constant for the molecules to spend on the walls before desorption (hereafter desorption time constant, denoted as t_{des}). In the absence of heterogeneous wall chemistry, the atmospheric densities, n_{atm} , chamber densities, n_{ch} and surface densities, σ on the walls of a given species are related through

$$0 = n_{\text{atm}}v_{\text{sc}}A_{\text{x}} - \frac{1}{4}n_{\text{ch}}v_{\text{th}}A_{\text{x}} - S\frac{d\sigma}{dt}, \quad (5.1)$$

$$\frac{d\sigma}{dt} = \frac{1}{4}n_{\text{ch}}v_{\text{th}}p_{\text{ads}} - \frac{\sigma}{t_{\text{des}}}, \quad (5.2)$$

where $V_{\text{ch}} = 3.3 \text{ cm}^3$ is the chamber volume, $S = 11 \text{ cm}^2$ is the surface area of the chamber walls, $A_x = 0.22 \text{ cm}^2$ is the size of the entrance aperture, $v_{\text{sc}} = 6 \text{ km s}^{-1}$ is the spacecraft velocity, v_{th} is the thermal velocity of the given species corresponding to a constant wall temperature of 300 K, and I adopt a zero ram angle. I have also assumed a steady state for the gas in the INMS chamber, and in the limit of negligible wall effects, Eqn. 5.1 reduces to the ideal case of ram pressure enhancement (see Chapter 3.2). However, I still allow for the accumulation/depletion of gas on the chamber walls with time, i.e. nonzero $d\sigma/dt$.

In Eqn. 5.1 and 5.2, p_{ads} is assumed to be constant for any given species throughout the mission, and t_{des} is taken to be inversely proportional to the N_2 density in the chamber. This choice of t_{des} is based on the consideration that desorption is likely to be initiated by collisions of the incoming N_2 molecules with the chamber walls. Model calculations based on Eqn. 5.1 and 5.2 show that adopting a constant t_{des} produces too many counts for the outbound legs in all realistic cases to match the observations, thus the scheme with a constant t_{des} will not be further discussed in this thesis. Since the N_2 densities in the chamber are directly determined from the measurements, I only need to specify the value of t_{des} for a reference N_2 density, chosen as a chamber density of $1 \times 10^{11} \text{ cm}^{-3}$ throughout my model calculations (corresponding to an ambient N_2 density of $\sim 2 \times 10^9 \text{ cm}^{-3}$). For any heavy species, the value of t_{des} for this reference N_2 density is assumed to be constant for all flybys. This parameter is denoted as $t_{\text{des}}^{(\text{ref})}$ in the rest of the thesis, and clearly I have $t_{\text{des}} = t_{\text{des}}^{(\text{ref})}[10^{11}/n_{\text{ch}}(\text{N}_2)]$ where $n_{\text{ch}}(\text{N}_2)$ is the chamber density of N_2 in units of cm^{-3} .

I solve Eqn. 5.1 and 5.2 for the chamber density, n_{ch} and wall surface density, σ for a given species and given flyby, with any combination of p_{ads} and $t_{\text{des}}^{(\text{ref})}$, and with the initial condition of zero wall surface density at -500 sec from C/A. The density profile of the given species in the ambient atmosphere has also to be specified a priori. Here I assume that the atmospheric density profile of any heavy species follows

diffusive equilibrium, i.e. decreases exponentially with its own scale height (with a constant temperature of 154 K in the ambient atmosphere, see Chapter 5.2.1 below). The remaining free parameter of the atmospheric density at any reference altitude is easily constrained by requiring that the peak model profile of n_{ch} matches the observed peak chamber density. Such a procedure is justified by the self-similarity of Eqn. 5.1 and 5.2.

In principle, I can compare the model chamber density profiles directly to the INMS observations, and search for the most probable values of p_{ads} and $t_{\text{des}}^{(\text{ref})}$ in a minimum χ^2 sense. Here I adopt a simplified scheme, in which both the observed and calculated chamber densities are parametrized in the same way, and the most probable values of p_{ads} and $t_{\text{des}}^{(\text{ref})}$ are identified by comparing the values of the selected parameters. In more detail, I find that for a given species, the variation of the chamber density with time from C/A can be reasonably fit with a shifted Gaussian distribution, $n_{\text{ch}} \propto \exp[-(t - t_0)^2/\Delta t^2]$, where the time shift, t_0 and time width, Δt are two free parameters in the fitting. Similarly, I use the same empirical form to fit the model chamber density profile. For any combination of p_{ads} and $t_{\text{des}}^{(\text{ref})}$, the model chamber density profiles are calculated separately for different flybys and then averaged over the whole sample. I search for regions in the $p_{\text{ads}} - t_{\text{des}}^{(\text{ref})}$ parameter space where t_0 and Δt values roughly overlap between the model and the observations.

An example is given in Fig. 5.4 for C_4H_2 , representing a case for which the values of p_{ads} and t_{des} can be reasonably constrained by the data. The upper and lower panels of Fig. 5.4 show the distribution of t_0 and Δt in the parameter space, calculated from the adsorption/desorption model. Their values are estimated from the INMS data as 42 ± 5 sec and 100 ± 8 s respectively, where the uncertainties quoted above represent standard deviations among different flybys. The thick solid line in Fig. 5.4 gives the region for consistent values of both t_0 and Δt between the model and the observations (within 1σ standard deviation). This region constrains the possible values of the adsorption probability to be $p_{\text{ads}} > 0.2$ and the desorption time constant to be $60 < t_{\text{des}}^{(\text{ref})} < 180$ s, where $t_{\text{des}}^{(\text{ref})}$ is for a reference N_2 chamber

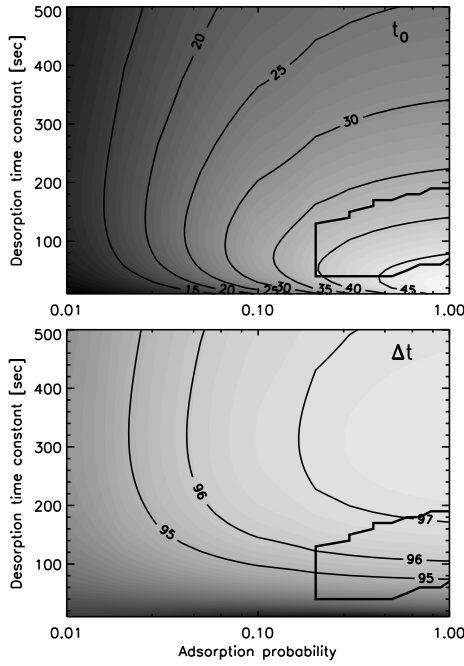


Figure 5.4 The distribution of t_0 and Δt in the parameter space of adsorption probability (p_{ads}) and desorption time constant ($t_{\text{des}}^{(\text{ref})}$ referred to an N_2 chamber density of 10^{11} cm^{-3}), where t_0 and Δt represent the time shift and width of the shifted Gaussian function used to characterize both the observed and model chamber density profiles. The thick solid lines mark the region where the combination of p_{ads} and $t_{\text{des}}^{(\text{ref})}$ provides reasonable fit to the observed chamber densities, following the simple adsorption/desorption model proposed in the thesis.

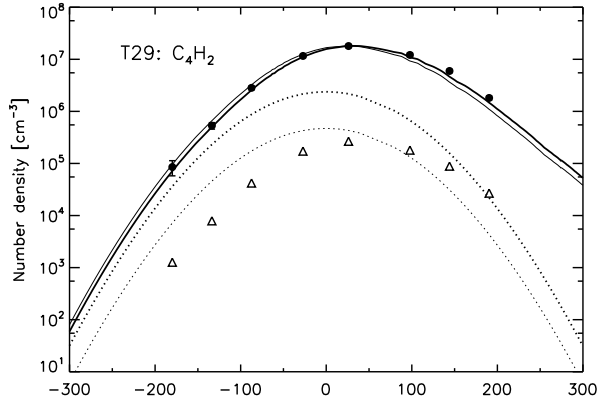


Figure 5.5 The simple adsorption/desorption model fitting to the C_4H_2 densities obtained during the T29 flyby, as a function of time from C/A. The solid circles represent the observed C_4H_2 densities in the chamber, and the open triangles the corresponding atmospheric densities calculated with the ram enhancement factor. The solid and dotted lines represent the model density profiles, with the thick ones assuming $p_{\text{ads}} = 0.8$ and $t_{\text{des}} = 150\text{s}$ (referred to an N_2 chamber density of 10^{11}cm^{-3}) and the thin ones assuming $p_{\text{ads}} = 0.1$ and the same desorption time constant.

density of 10^{11}cm^{-3} .

I show in Fig. 5.5 the model calculations for the wall effects of C_4H_2 observed during the T19 flyby. The solid lines show the C_4H_2 density profiles in the chamber, calculated from Eqn. 5.1 and 5.2. The thick solid line is calculated with an adsorption probability of $p_{\text{ads}} = 0.8$ and a desorption time constant of $t_{\text{des}}^{(\text{ref})} = 150\text{s}$, within the region of the $p_{\text{ads}} - t_{\text{des}}^{(\text{ref})}$ parameter space where the model reasonably matches the observed C_4H_2 chamber density profile (indicated by the solid circles). The thin solid line is calculated with $p_{\text{ads}} = 0.1$ and the same desorption time constant, and does not fit the observations, especially for outbound measurements. The thick and thin dotted lines give the corresponding C_4H_2 density profiles in the ambient atmosphere, which are symmetric about C/A and follow diffusive equilibrium. Clearly, the true atmospheric abundances of C_4H_2 in both cases are significantly higher than the values derived by considering the ram pressure enhancement only (indicated by the open triangles in the figure).

The simple adsorption/desorption model presented above reasonably describes

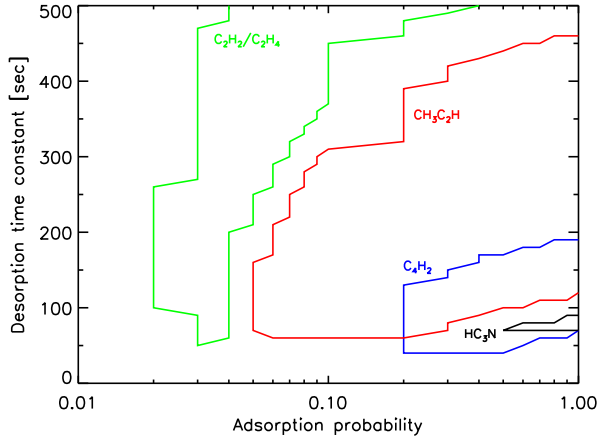


Figure 5.6 The regions in the parameter space of adsorption probability and desorption time constant, where the combinations of these two parameters provide reasonable fits to the observed chamber densities, following the simple adsorption/desorption model proposed in the thesis. Different colors stand for different species, and the desorption time constants are given for a reference N_2 chamber density of 10^{11} cm^{-3} . For most species, the values of these parameters are not well constrained by the INMS data.

the variation of several minor species with time from C/A, including C_2H_2/C_2H_4 , CH_3C_2H , C_4H_2 , C_6H_6 , HC_3N and NH_3 . I show in Fig. 5.6 the regions of the $p_{\text{ads}} - t_{\text{des}}^{(\text{ref})}$ parameter space for C_2H_2/C_2H_4 , CH_3C_2H , C_4H_2 and HC_3N where the calculated chamber density profiles reasonably match the observations in terms of the parametrization with a shifted Gaussian, as discussed above. C_6H_6 and NH_3 are not shown in the figure, since heterogeneous surface chemistry on the chamber walls might be of more importance, which will be addressed further below. The values for the adsorption probability and desorption time constant are not well constrained for C_2H_2/C_2H_4 and CH_3C_2H , with a wide range of p_{ads} and $t_{\text{des}}^{(\text{ref})}$ values reasonably reproducing the data. In contrast, for C_2N_2 , no combination of these parameters produces the model chamber density profile that matches the observations. This may imply that the simple adsorption/desorption model proposed here does not provide a reasonable representation of the wall effects for this species. For other minor species, including C_2H_6 , C_3H_8 , C_4H_6 , C_7H_8 , CH_3CN , C_2H_3CN , H_2O and CO_2 , the simple

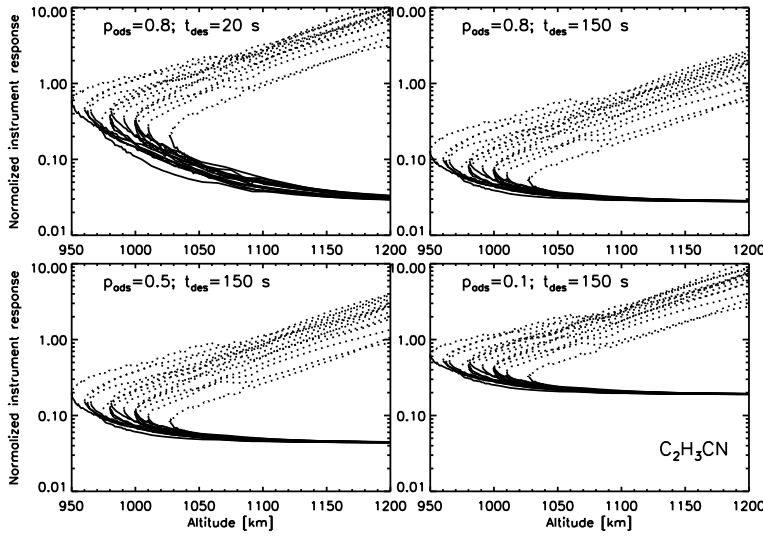


Figure 5.7 The realistic instrument response function calculated for $\text{C}_2\text{H}_3\text{CN}$ for different flybys and normalized by the ideal ram enhancement factor. The solid and dotted line portions of each curve represent the inbound and outbound passes, respectively. Values of the adsorption probability, p_{ads} and the desorption time constant, t_{des} used in the model calculations are indicated on the figure, where t_{des} is given for a reference N_2 chamber density of 10^{11} cm^{-3} .

adsorption/desorption model for wall effects will not be investigated directly based on the data, since most of the inbound INMS spectra give upper limit densities for these species, and model fits to constrain p_{ads} and $t_{\text{des}}^{(\text{ref})}$ are unreliable.

Despite the difficulty in applying the simple adsorption/desorption model directly to other heavy species, it is interesting to investigate how the realistic instrument response for a given species varies with time from C/A, for various choices of the adsorption probability and desorption time constant. Owing to the self-similarity of Eqn. 5.1 and 5.2, such an investigation can be easily performed for all species independent of their actual measurements. An example is shown in Fig. 5.7 for $\text{C}_2\text{H}_3\text{CN}$, for which most of the individual INMS spectra give upper limit densities due to the low signal-to-noise ratios of counts in channel 53 (also see Chapter 4.4). The realistic instrument response functions for all flybys are given as a function of altitude, normalized by the ram pressure enhancement factor assuming zero ram an-

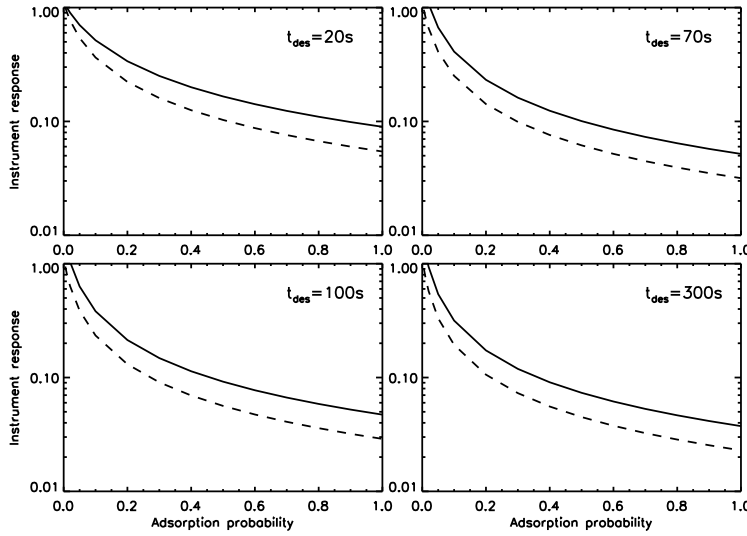


Figure 5.8 The instrument response as a function of adsorption probability, for several choices of the desorption time constant (all referred to an N_2 chamber density of 10^{11} cm^{-3}). In each panel, the solid and dashed lines represent the instrument response for species with a molecular mass of 30 and 80, respectively. This represents the reasonable mass range for all heavy species included in my spectral analysis.

gle. The solid line portion and dotted line portion of each curve in the figure stand for inbound and outbound passes, respectively. The values of p_{ads} and $t_{\text{des}}^{(\text{ref})}$ adopted for the calculations are also indicated in the figure. Clearly, the true atmospheric abundances are underestimated for normalized instrument response smaller than unity. Comparisons between different panels of Fig. 5.7 and the same calculations for other species immediately reveal that the instrument response for the inbound measurements tends to a fairly constant level above $\sim 1,050 \text{ km}$ for all flybys. This feature suggests that it is likely to correct for the wall adsorption/desorption effects based on the inbound measurements obtained not too close to C/A.

I show in Fig. 5.8 the instrument response as a function of adsorption probability, normalized by the 'ideal' ram enhancement factor and averaged between 1,050 and 1,200 km over the inbound portions of all flybys. Different panels represent different choices of the desorption time constant, $t_{\text{des}}^{(\text{ref})}$ (referred to the value for an N_2 chamber density of 10^{11} cm^{-3} , see above). In each panel, the solid and dashed lines correspond

to species with molecular mass of 30 and 80, respectively. This reasonably represents the mass range for most heavy species included in my spectral analysis. From Fig. 5.8, at the limit of no adsorption ($p_{\text{ads}} = 0$), the normalized instrument response is close to unity, i.e. identical to the ram enhancement factor, which is expected since no correction for wall effects is required. At the limit of complete adsorption ($p_{\text{ads}} = 1$), the instrument response tends to a constant value which is not sensitive to the molecular mass and the desorption time constant, at least for $t_{\text{des}}^{(\text{ref})} > 100$ s. I notice that for any individual flyby, the spacecraft travels through Titan's upper atmosphere from an altitude of 1,200 km to C/A with a typical time of ~ 200 s. Therefore, with a desorption time constant comparable with or greater than this value, the desorption term in Eqn. 5.2 is not important, and thus the chamber densities are largely controlled by the adsorption probability alone. On the other hand, with a small desorption time constant, incoming molecules adsorbed on the chamber walls get desorbed nearly locally and the instrument response depends on both the adsorption probability and desorption time constant.

Fig. 5.8 presents a scheme to correct for the wall adsorption/desorption effects for typical heavy species detected by the INMS. The (multiplicative) correction factor can be adopted as the inverse of the normalized instrument response shown in the figure. In the case of complete adsorption ($p_{\text{ads}} = 1$) and large desorption time constant ($t_{\text{des}} > 100$ s), the normalized instrument response tends to a constant value of ~ 0.03 roughly independent of molecular mass. This is to say that the densities obtained from the INMS measurements adopting the ram enhancement factor should be divided by the same factor, or equivalent, multiplied by a factor of ~ 30 , in order to get the true atmospheric abundances. I emphasize that the normalized instrument response shown in Fig. 5.8 should only be applied to inbound measurements away from C/A. At lower altitudes or for outbound measurements, correction for wall adsorption/desorption is more difficult, since Fig. 5.7 shows that the calculated instrument response function presents a significant scattering from flyby to flyby and is dependent on both the adsorption probability and desorption time constant.

An inherent assumption in the simple wall effect model presented here is that

no heterogeneous surface chemistry is involved. Therefore, even though the adsorption/desorption model is able to provide reasonable fits to the observed chamber density profiles of C_6H_6 as mentioned above, the interpretation of this result deserves some caution, since Vuitton *et al.* (2008) have shown that a significant fraction of the observed C_6H_6 molecules are those formed through the recombination of C_6H_5 radicals on the chamber walls. This additional chemical source term is not included in the model presented here. The similar process for C_7H_8 has also been discussed in Vuitton *et al.* (2008). Another species likely to be influenced by wall surface chemistry is NH_3 , due to the relatively high abundances of N and H radicals in the ambient atmosphere. In fact, the NH_3 mixing ratios directly obtained from the INMS data in the CSN mode are much higher than those predicted from the measurements of the associated ion species in the OSI mode (Vuitton *et al.* 2007), even without a correction for wall adsorption/desorption. To reconcile with the OSI results, it is reasonable to assume that a significant fraction of the NH_3 molecules in the INMS chamber are formed from N and H radicals through surface chemistry. In addition, as mentioned above, the observed C_2N_2 chamber densities cannot be reproduced by the adsorption/desorption model, with any combination of p_{ads} and $t_{\text{des}}^{(\text{ref})}$ values. Considering this, I also treat C_2N_2 as a species for which surface chemistry is likely to be a concern. Fortunately, such an effect of surface chemistry may not be important for other minor species, due to the very low abundances of the associated radicals in the ambient atmosphere, as revealed by photochemical model calculations (e.g. Lavvas *et al.* 2008a, b). For these species, the simple adsorption/desorption processes are likely to be the dominant aspect of the wall effects, and with a knowledge of their adsorption probability as well as desorption time constant, their true atmospheric abundances can be reasonably obtained with the realistic instrument response as shown in Fig. 5.7 and 5.8. I will revisit this issue in Chapter 5.2.3, in which I present the atmospheric abundances of various minor species with possible effects of wall adsorption/desorption corrected.

To summarize, in the following sections, I will analyze both the inbound and outbound measurements. While the densities derived for N_2 , CH_4 , H_2 and ^{40}Ar (as

well as their isotopes) reflect true values in the ambient atmosphere, the interpretation of the abundances of other minor species deserves caution, since wall effects have been shown as important. How the measured counts reflect the abundances of the local atmosphere relies on the details of the wall effects, which could be either simple adsorption/desorption processes or more complicated heterogeneous surface chemistry on the chamber walls. Due to the peculiar scale heights as shown in Fig. 5.2, the outbound measurements of heavy minor species are not representative of the ambient atmosphere. I choose two schemes for the analysis of heavy species, either based on direct SVD fits to the inbound mass spectra or based on the simple model proposed above to correct for wall adsorption/desorption. The model requires a knowledge of the adsorption probability and desorption time constant, the latter of which is assumed to be inversely proportional to the N_2 density in the chamber. The possible values for these two parameters are obtained for several species in this section (see Fig. 5.6), which will be treated as a guide to the analysis of other species in Chapter 5.2.3.

5.2 Globally averaged vertical distribution

5.2.1 Nitrogen, methane and hydrogen

The globally averaged density profiles of N_2 , CH_4 and H_2 have been presented in some recent papers, based on a smaller INMS sample (Yelle *et al.* 2006, 2008, Cui *et al.* 2008). The analysis of the H_2 distribution will be extended to regions well above Titan's exobase in Chapter 6. The mixing ratios of these species and their errors are detailed in Table 5.1 at four representative altitudes. These errors correspond to uncertainties due to counting statistics and sensitivity calibration, not necessarily associated with horizontal and/or diurnal variations. Uncertainties due to background subtraction have been included through error propagation. Fig. 5.9 shows with the solid circles the globally averaged density profiles of these species as a function of altitude, between 950 and 1,500 km. These profiles are based on the densities directly determined from their main channels (Müller-Wodarg *et al.* 2008,

Table 5.1 Globally averaged total densities and mixing ratios of neutral constituents in Titan's upper atmosphere, obtained directly from the inbound measurements, assuming ram pressure enhancement only. Errors include uncertainties due to both counting statistics and sensitivity calibration.

Altitude	981 km	1,025 km	1,077 km	1,151 km
Density [cm^{-3}]	$(8.90 \pm 0.01) \times 10^9$	$(4.35 \pm 0.01) \times 10^9$	$(1.95 \pm 0.01) \times 10^9$	$(7.23 \pm 0.01) \times 10^8$
N ₂	(96.7 \pm 0.1)%	(96.2 \pm 0.2)%	(95.7 \pm 0.5)%	(94.8 \pm 0.1)%
CH ₄	(1.61 \pm 0.01)%	(2.06 \pm 0.01)%	(2.45 \pm 0.01)%	(3.41 \pm 0.01)%
H ₂	$(3.81 \pm 0.01) \times 10^{-3}$	$(4.15 \pm 0.01) \times 10^{-3}$	$(4.55 \pm 0.02) \times 10^{-3}$	$(4.95 \pm 0.01)\%$
HD	$(8.66 \pm 0.16) \times 10^{-5}$	$(5.31 \pm 0.12) \times 10^{-5}$	$(3.23 \pm 0.13) \times 10^{-5}$	$< 2.10 \times 10^{-5}$
⁴⁰ Ar	$(1.66 \pm 0.04) \times 10^{-5}$	$(1.40 \pm 0.03) \times 10^{-5}$	$(1.25 \pm 0.04) \times 10^{-5}$	$(8.76 \pm 0.43) \times 10^{-6}$
³⁶ Ar	$< 2.38 \times 10^{-6}$	$< 1.17 \times 10^{-6}$	$< 1.01 \times 10^{-6}$	$< 7.11 \times 10^{-7}$
C ₂ H ₂ /C ₂ H ₄	$(1.35 \pm 0.02) \times 10^{-4}$	$(1.40 \pm 0.02) \times 10^{-4}$	$(1.33 \pm 0.02) \times 10^{-4}$	$(1.10 \pm 0.02) \times 10^{-4}$
C ₂ H ₆	$(3.39 \pm 0.25) \times 10^{-5}$	$(3.16 \pm 0.28) \times 10^{-5}$	$< 2.09 \times 10^{-5}$	$< 1.81 \times 10^{-5}$
CH ₃ C ₂ H	$(1.20 \pm 0.05) \times 10^{-5}$	$(9.60 \pm 0.34) \times 10^{-6}$	$(6.11 \pm 0.27) \times 10^{-6}$	$< 2.81 \times 10^{-6}$
C ₃ H ₈	$< 3.97 \times 10^{-6}$	$< 2.07 \times 10^{-6}$	$< 2.38 \times 10^{-6}$	$< 1.22 \times 10^{-6}$
C ₄ H ₂	$(7.97 \pm 0.21) \times 10^{-6}$	$(4.99 \pm 0.14) \times 10^{-6}$	$(2.52 \pm 0.12) \times 10^{-6}$	$< 1.38 \times 10^{-6}$
C ₄ H ₆	$< 2.46 \times 10^{-7}$	$< 1.83 \times 10^{-7}$	$< 1.67 \times 10^{-7}$	$< 3.34 \times 10^{-7}$
C ₆ H ₆	$(4.90 \pm 0.12) \times 10^{-6}$	$(2.25 \pm 0.07) \times 10^{-6}$	$(6.99 \pm 0.45) \times 10^{-7}$	$< 1.89 \times 10^{-7}$
C ₇ H ₈	$< 6.39 \times 10^{-8}$	$< 4.49 \times 10^{-8}$	$< 8.30 \times 10^{-8}$	$< 1.31 \times 10^{-7}$
HC ₃ N	$(2.17 \pm 0.11) \times 10^{-6}$	$(1.30 \pm 0.07) \times 10^{-6}$	$< 7.15 \times 10^{-7}$	$< 4.11 \times 10^{-7}$
CH ₃ CN	$< 1.87 \times 10^{-6}$	$< 1.52 \times 10^{-6}$	$< 1.36 \times 10^{-6}$	$< 5.82 \times 10^{-7}$
C ₂ H ₃ CN	$< 3.74 \times 10^{-7}$	$< 2.98 \times 10^{-7}$	$< 2.87 \times 10^{-7}$	$< 2.88 \times 10^{-7}$
C ₂ N ₂	$(1.77 \pm 0.10) \times 10^{-6}$	$(1.76 \pm 0.09) \times 10^{-6}$	$(1.42 \pm 0.10) \times 10^{-6}$	$< 8.92 \times 10^{-7}$
NH ₃	$< 1.57 \times 10^{-5}$	$(3.87 \pm 0.29) \times 10^{-5}$	$(3.44 \pm 0.30) \times 10^{-5}$	$< 4.05 \times 10^{-5}$
H ₂ O	$< 1.23 \times 10^{-5}$	$< 3.47 \times 10^{-6}$	$< 3.92 \times 10^{-6}$	$< 3.30 \times 10^{-6}$
CO ₂	$< 1.28 \times 10^{-6}$	$< 5.78 \times 10^{-7}$	$< 7.53 \times 10^{-7}$	$< 1.10 \times 10^{-6}$

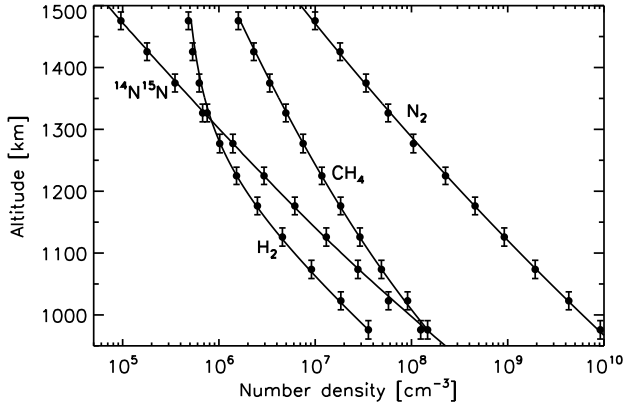


Figure 5.9 The globally averaged density profiles of N_2 , CH_4 , H_2 and $^{14}\text{N}^{15}\text{N}$, between 950 and 1,500 km. The solid line overplotted on the N_2 observations is the best-fit hydrostatic equilibrium model, with a thermospheric temperature of 154 K. Also shown are the best-fit isothermal diffusion models for CH_4 and H_2 , with a most probable escape flux of $3.0 \times 10^9 \text{ cm}^{-2} \text{ s}^{-1}$ (for CH_4) and $1.3 \times 10^{10} \text{ cm}^{-2} \text{ s}^{-1}$ (for H_2), referred to Titan's surface. The diffusion model for $^{14}\text{N}^{15}\text{N}$ predicts a most probable nitrogen isotope ratio, $^{14}\text{N}/^{15}\text{N}$ of 131.6 ± 0.2 near Titan's surface (see also Fig. 5.11).

Cui *et al.* 2008). Both inbound and outbound data are included for these species, since the wall effects are negligible as shown in Fig. 5.1.

As the most abundant atmospheric species on Titan, the density distribution of N_2 directly provides information on the thermospheric temperature, assuming hydrostatic equilibrium. The most recent determination is given by Cui *et al.* (2008) as 152.5 K, which is also consistent with earlier results from Voyager UVS measurements (Vervack *et al.* 2004). Based on the N_2 distribution between 950 and 1,500 km obtained in this work, I derive a similar thermospheric temperature of $154.0 \pm 1.5 \text{ K}$, and the corresponding hydrostatic equilibrium model is overplotted on the data in Fig. 5.9. The small change in the temperature value is primarily associated with the additional data (T36 and T37) included in this work compared with previous analysis.

The vertical distribution of CH_4 and H_2 can each be described by the diffusion

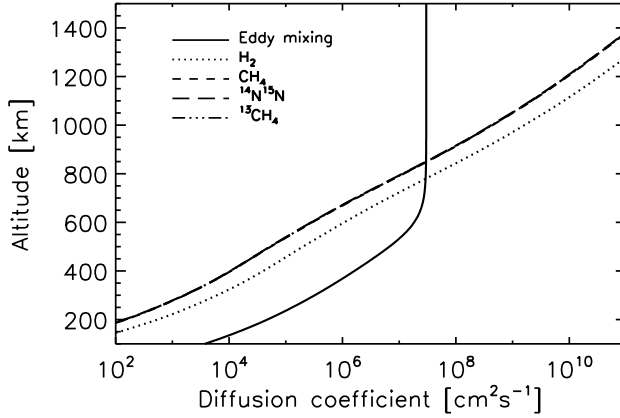


Figure 5.10 Diffusion coefficients adopted in this study as a function of altitude between 100 and 1,500 km. The eddy mixing profile, adopted from Yelle *et al.* (2008), is given by the solid line, and the molecular diffusion coefficients are given by the dotted line (for H_2), short-dashed line (for CH_4), long-dashed line (for $^{14}\text{N}^{15}\text{N}$) and dash-dotted line (for $^{13}\text{CH}_4$). The molecular diffusion coefficients for CH_4 , $^{14}\text{N}^{15}\text{N}$ and $^{13}\text{CH}_4$, which are nearly identical, cannot be distinguished on the figure.

model,

$$F_i = -(D_i + K)\left(\frac{dn_i}{dr} + \frac{n_i}{T} \frac{dT}{dr}\right) - \left(\frac{D_i}{H_i} + \frac{K}{H_a}\right)n_i, \quad (5.3)$$

where n_i and F_i are the flux and number density of species i , D_i is the molecular diffusion coefficient taken from Mason & Marrero (1970) and K the eddy diffusion coefficient, $H_i = (k_B T)/(m_i g)$ is the scale height with $T = 154$ K being the thermospheric temperature, k_B the Boltzmann constant, g the local gravity, and m_i the molecular mass of species i , $H_a = (k_B T)/(m_a g)$ is the scale height of the ambient atmosphere, with m_a representing the mean molecular mass. The mean molecular mass is calculated from the observed densities of various species at any given altitude, which decreases monotonically from 27.8 amu at 950 km to 25.1 amu at 1,500 km. I adopt an eddy profile given by Eqn. 4 in Yelle *et al.* (2008). The asymptotic eddy diffusion coefficient, K_∞ is taken as $3 \times 10^7 \text{ cm}^2 \text{ s}^{-1}$, based on both INMS and GCMS observations of ^{40}Ar (Yelle *et al.* 2008). The eddy mixing profile adopted in this work, along with the molecular diffusion coefficients for H_2 and CH_4 are shown in Fig. 5.10. The figure shows that diffusive separation becomes important above a homopause level at $\sim 800\text{--}850$ km.

The isothermal diffusion model given by Eqn. 5.3 is applied to the globally averaged density profiles of CH_4 and H_2 between 950 and 1,500 km. The boundary conditions are adopted from the INMS data as $1.47 \times 10^8 \text{ cm}^{-3}$ for CH_4 and $3.56 \times 10^7 \text{ cm}^{-3}$ for H_2 at 976 km. The neglect of the thermal diffusion term in Eqn. 5.3 follows the assumption of isothermal. Though the condition of energy continuity may imply modest temperature decrement near the exobase for these two species, such a thermal effect does not have an appreciate influence on the solution to the diffusion equation (Cui *et al.* 2008).

I solve Eqn. 5.3 with a 4th-order Runge-Kutta algorithm, taking into account the variation of gravity with altitude. The CH_4 and H_2 fluxes referred to Titan's surface are treated as free parameters in the fitting. The most probable flux values are found to be $(3.04^{+0.06}_{-0.10}) \times 10^9 \text{ cm}^{-2} \text{ s}^{-1}$ for CH_4 and $(1.29 \pm 0.01) \times 10^{10} \text{ cm}^{-2} \text{ s}^{-1}$ for H_2 . These flux values are in general consistent with the values given by Yelle *et al.* (2008) and Cui *et al.* (2008), with the small differences due to the inclusion of more INMS data. Notice that eddy diffusion is not included in the analysis of H_2 distribution by Cui *et al.* (2008), which causes some further deviations, but not significant since molecular diffusion dominates at these altitudes above the homopause. The errors of the best-fit fluxes given above are related to uncertainties in the eddy profile, with a reasonable range of K_∞ values between $2 \times 10^7 \text{ cm}^2 \text{ s}^{-1}$ and $5 \times 10^7 \text{ cm}^2 \text{ s}^{-1}$ (Yelle *et al.* 2008). The diffusion models for CH_4 and H_2 , calculated with the best-fit fluxes, are shown by the solid lines in Fig. 5.9.

The H_2 flux on Titan derived above is higher than the Jeans value of $4.6 \times 10^9 \text{ cm}^{-2} \text{ s}^{-1}$ (referred to the surface) by a factor of ~ 3 , where the Jeans flux is calculated with a temperature of 154 K and an exobase height of 1,500 km. However, this is not necessarily associated with any nonthermal mechanism of H_2 escape on Titan. The interpretation of this result will be presented in Chapter 6.4.

The CH_4 escape flux is more sensitive to the choice of the eddy profile, due to the relatively low molecular diffusion coefficient (see Fig. 5.10). Yelle *et al.* (2006) has shown that the CH_4 distribution on Titan observed with INMS can be understood in terms of either a significant escape flux or an eddy diffusion coefficient much higher

than the typical values for other planetary systems. However, the eddy profile constrained independently from the INMS/GCMS observations of ^{40}Ar unambiguously shows that interpreting the observed CH_4 distribution on Titan requires a significant escape flux (Yelle *et al.* 2008). Since the Jeans flux of CH_4 is tiny (of order $1 \text{ cm}^{-2} \text{ s}^{-1}$ referred to the surface) due to the relatively large CH_4 molecular mass and the low exobase temperature on Titan, non-thermal processes are required to account for the observed CH_4 escape. Further supports on the non-thermal escape of CH_4 come from the exospheric distribution of this species on Titan, which suggests the presence of a suprathermal CH_4 corona (De La Haye *et al.* 2007a).

5.2.2 Isotope ratios

The observed $^{14}\text{N}^{15}\text{N}$ densities are shown in Fig. 5.9 as a function of altitude, obtained by averaging over all flybys. Similar to the treatment of CH_4 and H_2 , I fit the INMS observations of $^{14}\text{N}^{15}\text{N}$ with a diffusion model, assuming zero upward flux. Here to compare with the nitrogen isotope ratio obtained in Titan's lower atmosphere, I adopt the temperature profile given by Yelle *et al.* (2008) and extend the diffusion model calculation from 1,500 km down to Titan's surface. Such a temperature profile was obtained by combining CIRS results below 500 km (Vinatier *et al.* 2007) and INMS results above 1,000 km (Müller-Wodarg *et al.* 2008). The molecular diffusion coefficient of $^{14}\text{N}^{15}\text{N}$ in the background N_2 gas can be estimated from measurements of H_2 and CH_4 . Kinetic theory predicts that the molecular diffusion coefficient is inversely proportional to the molecular mass of the minor species and its collision frequency with the background component (Schunk & Nagy 2000). For a hard sphere approximation, it can be shown that

$$\frac{D_2}{D_1} = \sqrt{\frac{m_1(m_2 + m_0)}{m_2(m_1 + m_0)}} \left(\frac{a_1 + a_0}{a_2 + a_0} \right)^2, \quad (5.4)$$

where D_1 and D_2 stand for the molecular diffusion coefficients for species 1 and 2, both diffusing through the same background component denoted by 0, m_i and a_i are the mass and hard sphere radius of an i molecule. I adopt values of a_i given

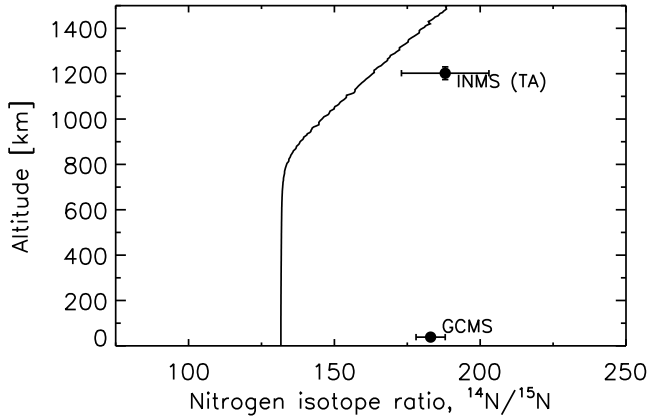


Figure 5.11 The solid line shows the profile of $^{14}\text{N}/^{15}\text{N}$ isotope ratio as a function of altitude, with a most probable value of 131.6 ± 0.2 near Titan's surface. The temperature profile of Yelle *et al.* (2008) is adopted. The solid circles show the GCMS measurement of 183 ± 5 at 36-41 km (Niemann *et al.* 2005), and the INMS TA measurement of 188^{+14}_{-16} at 1,200 km (Waite *et al.* 2005).

by De La Haye *et al.* (2007b), inferred from viscosity measurements of pure i gas. Applying Eqn. 5.4 to both H_2 and CH_4 , I find that the molecular diffusion coefficient for $^{14}\text{N}^{15}\text{N}$ is 26% of the H_2 value and 96% of the CH_4 value, with the average of the two adopted in the diffusion model (given by the long-dashed line in Fig. 5.10).

I solve Eqn. 5.3 for $^{14}\text{N}^{15}\text{N}$, treating the nitrogen isotope ratio at Titan's surface as the only free parameter. The most probable value is found to be 131.6 ± 0.2 , i.e. about half of the terrestrial isotope ratio. The model $^{14}\text{N}^{15}\text{N}$ profile is shown in Fig. 5.9, overplotted on the INMS data.

The vertical variation of the nitrogen isotope ratio, $^{14}\text{N}/^{15}\text{N}$ is given in Fig. 5.11 throughout Titan's atmosphere. The ratio remains constant below ~ 800 km, and increases monotonically above as a result of diffusive separation, since $^{14}\text{N}^{15}\text{N}$ is slightly heavier than N_2 . Also shown in Fig. 5.11 is the TA measurement of 188^{+14}_{-16} based on the integration method (Waite *et al.* 2005). This is about 15% higher than my value at the same altitude of $\sim 1,200$ km. Such a deviation might be associated with the scaling factor applied to the branching ratio of N_2 at channel 14, to ensure consistency between the N_2 densities derived from different channels (see Chapter 3.1.3). This calibration has not been considered in early INMS data analysis. The

effect of overflow near channel 28, likely leading to an underestimate of the nitrogen isotope ratio, is not a concern here, since crosstalk only contributes to a small fraction of signals in channel 29. The figure also shows that the INMS measurements of $^{14}\text{N}/^{15}\text{N}$ are not consistent with the GCMS value of 183 ± 5 estimated at 36-41 km (Niemann *et al.* 2005). The origin for such a deviation is likely to be associated with the uncertainties in the absolute calibration of both instruments.

In Chapter 4.3.2, I adopt a similar formalism to estimate the carbon isotope ratio in Titan's thermosphere, as a function of altitude, which is then used to separate contributions of $^{13}\text{CH}_4$ and NH_3 to counts in channel 17. In more detail, it can be shown from Eqn. 5.3 that

$$\frac{d}{dr}\left(\frac{n_1}{n_2}\right) = -\frac{n_1}{n_2}\left[\frac{1}{D_1 + K}\left(\frac{D_1}{H_1} + \frac{K}{H_a}\right) - \frac{1}{D_2 + K}\left(\frac{D_2}{H_2} + \frac{K}{H_a}\right) + \frac{u_1}{D_1 + K} - \frac{u_2}{D_2 + K}\right], \quad (5.5)$$

where 1 and 2 stand for CH_4 and $^{13}\text{CH}_4$, respectively, $u_1 = F_1/n_1$ and $u_2 = F_2/n_2$ are their drift velocities. The molecular diffusion coefficient of $^{13}\text{CH}_4$ is estimated by scaling from the measurements of H_2 and CH_4 according to Eqn. 5.4. The vertical profile of the $^{13}\text{CH}_4$ molecular diffusion coefficient is shown by the dash-dotted line in Fig. 5.10. Eqn. 5.5 indicates that the vertical variation of carbon isotope ratio depends on the fluxes of both CH_4 and its isotope. The CH_4 flux is dominated by escape throughout Titan's upper atmosphere, with a most probable value of $3.04 \times 10^9 \text{ cm}^{-2} \text{ s}^{-1}$ referred to the surface (see above). An estimate of the $^{13}\text{CH}_4$ flux requires a knowledge of the detailed (non-thermal) escape mechanism, which is still absent (e.g. De La Haye *et al.* 2007b). In the simplest case of Jeans escape and adopting an exobase temperature of 154 K, it can be shown that the $^{13}\text{CH}_4$ drift velocity (equal to the Jeans velocity in this case) is about 18% of the CH_4 Jeans velocity at the exobase. However, I have shown above that the CH_4 escape on Titan cannot be thermal (see also Yelle *et al.* 2008). Here I treat the drift velocity of $^{13}\text{CH}_4$ at the exobase as a free parameter in the model fitting, and use the condition of flux continuity to infer its values at other altitudes.

In the diffusion model fitting, the CH_4 escape flux is fixed with a value of $3.04 \times 10^9 \text{ cm}^{-2} \text{ s}^{-1}$ referred to the surface, and I adopt a lower boundary condition of

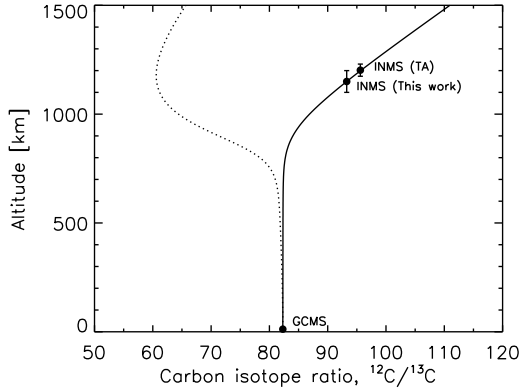


Figure 5.12 Diffusion model calculations of the carbon isotope ratio as a function of altitude, with the drift velocity ratio between $^{13}\text{CH}_4$ and CH_4 (at the exobase) treated as a free parameter. The solid line gives the best-fit model with a ratio of 1.14, and the dotted line corresponds to a ratio of 0.18 appropriate for Jeans escape. Also shown on the figure are the GCMS carbon isotope ratio of 82.3 measured at 6-18 km (Niemann *et al.* 2005), the INMS result of 95.6 obtained at an altitude of 1,200 km based on the TA data (Waite *et al.* 2005) and my result of 93.3 obtained at 1,100-1,200 km based on a much larger INMS sample.

$n(\text{CH}_4)/n(^{13}\text{CH}_4) = 82.3$ based on the GCMS measurements (Niemann *et al.* 2005). The best-fit model is obtained by comparing calculations with the estimated carbon isotope ratio of 93.3 at a reference altitude of 1,150 km (see Chapter 4.3.2). The most probable value of the drift velocity ratio is found to be $1.14^{+0.09}_{-0.07}$ at the exobase (placed at 1,500 km), implying that $^{13}\text{CH}_4$ molecules escape from Titan's atmosphere slightly faster than CH_4 molecules. However, such a result of enhanced escape of $^{13}\text{CH}_4$ (relative to CH_4) is not significant, since the value of the best-fit drift velocity at the exobase relies on my choice of the molecular diffusion coefficient. In the case when I adopt the profile of molecular diffusion coefficient for $^{13}\text{CH}_4$ 10% lower than the nominal choice (i.e. that scaled from the H_2 and CH_4 values according to Eqn. 5.4), I obtain a best-fit $^{13}\text{CH}_4$ drift velocity identical to that of CH_4 . Therefore, considering model uncertainties, my analysis of the carbon isotope ratio on Titan suggests that both CH_4 and $^{13}\text{CH}_4$ molecules roughly escape at the same speed, i.e. their flux ratio is about equal to the carbon isotope ratio at the exobase.

The vertical profile of the carbon isotope ratio inferred from the diffusion model

is given by the solid line in Fig. 5.12, matching the GCMS result and the INMS values derived both in this work and in the early analysis of Waite *et al.* (2005) based on the TA data. The model with a drift velocity ratio of 0.18 at the exobase, corresponding to Jeans escape but with the CH₄ flux still fixed as the non-thermal value of $3.04 \times 10^9 \text{ cm}^{-2} \text{ s}^{-1}$, is given by the dotted line for comparison. Such a model clearly underestimates the observed carbon isotope ratio in Titan's thermosphere, ruling out the possibility that CH₄ escapes much faster than its isotope in response to their different molecular masses.

Though HD is clearly identified in the INMS spectra by significant count rates in channel 3, the density determination of this species deserves some caution. On one hand, the broad background spectrum described in Chapter 3.5.1 appears to deviate from the presumed empirical form at the low-mass end (see Fig. 3.10). On the other hand, it is difficult to remove possible thruster firing contaminations in channel 3. In fact, ignoring all these potential uncertainties in data calibration, the D/H ratios inferred directly from counts in channels 2 and 3 are two orders of magnitude higher than the GCMS value (Niemann *et al.* 2005) and the results from remote-sensing observations (Coustenis *et al.* 1989, 2002, 2007) as well as theoretical predictions (Mousis *et al.* 2002). The effects of diffusive separation and H₂/HD escape are not strong enough to account for such a large difference. This may either imply that additional calibration of the channel 3 counts is required, or imply that some key physical/chemical mechanisms that control the thermospheric H/D ratio have been ignored. A full investigation of this issue will not be attempted in this work.

Finally, based on the SVD analysis, I can only put upper limits to the observed ³⁶Ar mixing ratios at all altitudes (see Table 5.1), due to the low signal-to-noise ratio of counts in channel 36. Combined with the ⁴⁰Ar measurements, an uninteresting lower limit of ~ 10 is derived for the argon isotope ratio, ⁴⁰Ar/³⁶Ar in Titan's thermosphere.

5.2.3 Minor species

In this section, I present my analysis of the abundances of heavy species in Titan's upper atmosphere. For these species, the dominant uncertainties are caused by the wall effects, which could be either simple adsorption/desorption processes or more complicated heterogeneous surface chemistry on the chamber walls (see Chapter 5.1). First, I will concentrate on the inbound measurements only, since the density profiles extracted from the outbound data show peculiar scale heights (i.e. comparable with or greater than the N_2 scale height), implying serious contamination by the wall effects during the outbound legs. Next, including both the inbound and outbound data, I adopt a simple model to correct for contamination by adsorption/desorption, assuming that no surface chemistry is involved. Such a model has been presented in Chapter 5.1, and in this section I will emphasize the results. The alternative scheme of wall effects through heterogeneous surface chemistry will not be considered here, since a correction for wall chemistry requires detailed information of the chemical reactions involved as well as an estimate of the abundances of the associated radicals in the ambient atmosphere (Vuitton *et al.* 2008).

I show in Fig. 5.13 the globally averaged mixing ratios of various minor species observed in Titan's upper atmosphere, obtained from the inbound measurements with the 'ideal' ram enhancement factor. No attempt has been made to correct for possible wall effects. The upper and lower panels present the distribution of various hydrocarbons and nitriles, respectively, as a function of altitude between 950 and 1,200 km. Leftward arrows in the figure indicate 3σ upper limits. Notice that upper limit mixing ratios obtained for the globally averaged distribution of a given minor species do not necessarily mean that all measurements from individual mass spectra are upper limits. In my analysis, upper limits are assigned to all cases in which more than half of the data points are right-censored, since in the statistical sense, the calculated mean value tends to be overestimated for a sample dominated by upper limits (Feigelson & Nelson 1985). The values of the mixing ratios for all minor species included in my spectral analysis are detailed in Table

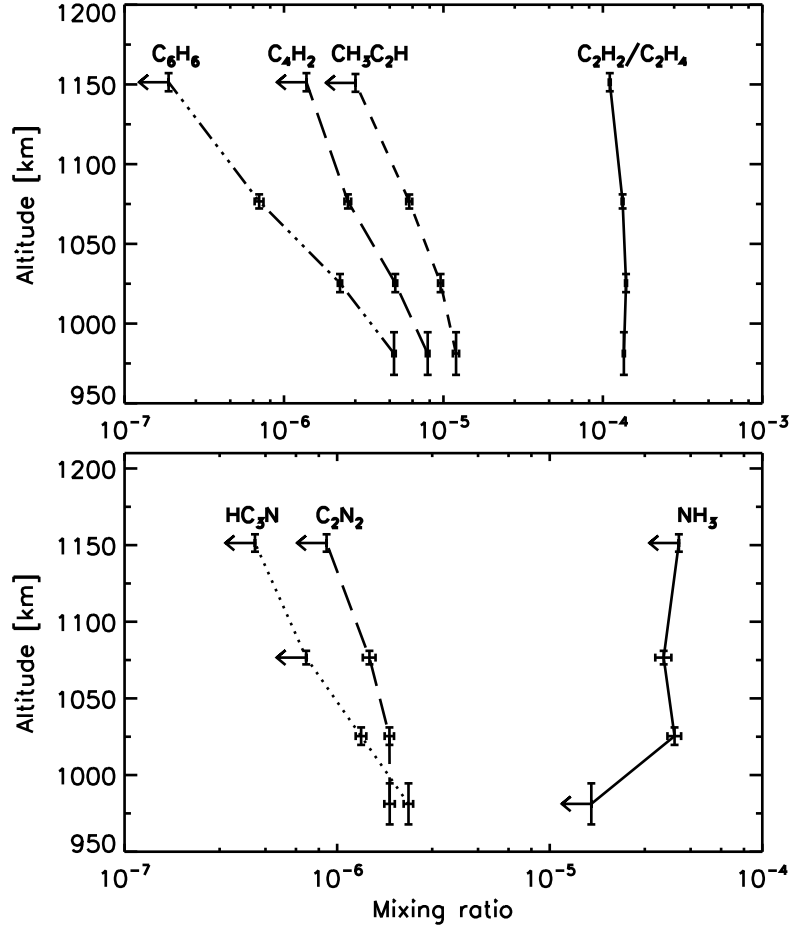


Figure 5.13 The globally averaged mixing ratios of various hydrocarbons and nitriles observed in Titan's upper atmosphere, as a function of altitude between 950 and 1,200 km. These mixing ratios are obtained by averaging over all inbound measurements, assuming ram pressure enhancement only. Leftward arrows indicate 3σ upper limits.

5.1, at four representative altitudes. A detailed comparison of the abundances of minor species between this study and previous works will be presented in Chapter 5.2.4. Here I notice that the typical mixing ratios for trace species given in Table 5.1 are $\sim 10^{-6} - 10^{-5}$. These values approximately correspond to a signal of 10 count per IP or $\sim 300 \text{ counts s}^{-1}$ for an individual measurement. Adopting a typical sensitivity of $5 \times 10^{-4} \text{ counts (cm}^{-3} \text{ s)}^{-1}$ and a typical ram enhancement factor of 70 for heavy species (taking into account ram pressure enhancement only), I get $300/(5 \times 10^{-4})/70 \approx 8 \times 10^3 \text{ cm}^{-3}$ for their typical densities, which correspond to a mixing ratio of $\sim 10^{-6} - 10^{-5}$ depending on altitude. Typical upper limits of mixing ratio can be as low as 10^{-7} , since integrating over several individual full mass scan helps to reduce the uncertainties caused by counting statistics.

The detection of several species in Titan's thermosphere, including C_2H_2 , C_2H_4 , HCN and HC_3N , has been reported by Vervack *et al.* (2004) based on the Voyager UVS solar occultation results. I have firm detections for three of them, except that the crosstalk near channel 28 prevents a reliable measurement of the HCN abundances (see Chapter 3.6).

Most of the minor species presented here have also been detected in Titan's stratosphere based on the recent Cassini/CIRS mid-infrared observations, including C_2H_2 , C_2H_4 , C_2H_6 , $\text{CH}_3\text{C}_2\text{H}$, C_3H_8 , C_4H_2 , C_6H_6 , HC_3N , C_2N_2 and CO_2 (Coustenis *et al.* 2007, Teanby *et al.* 2007a, b). Based on the INMS data, I have firm detections for most of them at much higher altitudes in Titan's thermosphere, except for C_3H_8 and CO_2 on which I am only able to put upper limits. However, as I have emphasized above, upper limit mixing ratios do not necessarily mean that all individual measurements are upper limits. Among all the 59 inbound mass spectra considered in this work, two of them show firm detections of CO_2 with a mean mixing ratio of 2.9×10^{-6} . For C_3H_8 , no firm detection is obtained for any individual spectrum, due to the low signal-to-noise ratio of counts in channel 43.

The detection of CH_3CN has been reported in the stratosphere from heterodyne ground-based spectroscopy (Bézard *et al.* 1993), but not revealed by the Cassini/CIRS data (Coustenis *et al.* 2007). The presence of $\text{C}_2\text{H}_3\text{CN}$ on Titan has

not been reported in any previous work, and only upper limit has been put (Marten *et al.* 2002, Coustenis *et al.* 2007). Based on the INMS data, both CH_3CN and $\text{C}_2\text{H}_3\text{CN}$ are not firmly detected in the thermosphere on a global average sense, indicated by upper limits at all altitudes. However, 9 individual inbound spectra give firm detections of CH_3CN , and the mean mixing ratio for these firm detections is 2.0×10^{-6} with a variation of 22%. For $\text{C}_2\text{H}_3\text{CN}$, only three inbound spectra give firm detections, with a mean mixing ratio of 5.4×10^{-7} and a variation of 36%.

No direct observation of NH_3 on Titan has been reported in previously works (in both the thermosphere and stratosphere), though this species was observed in laboratory experiments simulating the condition on this satellite (e.g. Bernard *et al.* 2003). Although NH_3 is likely to be a component of the spacecraft effluent, the thruster firing contamination may not be important here, since large excursions of signals in channel 17 are not seen, as opposed to the observations of channel 2 counts (see Fig. 3.7). Firm detection of NH_3 in a global average sense appears near 1,025 and 1,075 km, with a mixing ratio of $(3.9 \pm 0.3) \times 10^{-5}$ and $(3.4 \pm 0.3) \times 10^{-5}$ respectively. These measurements are much higher than the values predicted in existing photochemical models, (e.g. Wilson & Atreya 2004), indicating missing chemical pathways in previous works. As pointed out by Vuitton *et al.* (2007), heterogeneous chemistry on the surfaces of aerosol particles might be the solution. However, the interpretation of the above results deserves some caution. As shown in Fig. 5.3, the distribution of NH_3 along the spacecraft trajectory presents a large time offset, implying strong wall effects for this species. Though a simple adsorption/desorption model is used to describe the observed NH_3 chamber densities in Chapter 5.1, it is suspected that a full investigation of the NH_3 wall effects requires that surface chemistry be included, due to the relatively high abundances of N and H radicals in Titan's upper atmosphere. This is also motivated by measurements of the associated ion species in the OSI mode (Vuitton *et al.* 2007).

Finally, for the remaining three species, including C_4H_6 , C_7H_8 and H_2O , no firm detection can be made at any given altitude between 950 and 1,200 km. Especially, C_4H_6 and C_7H_8 is not detected at 3σ significance level in any individual inbound

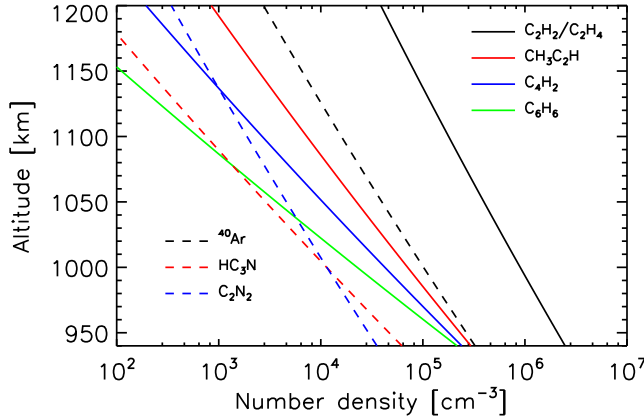


Figure 5.14 The power law fitting to the density distribution of various species in Titan's upper atmosphere, obtained by averaging over all inbound measurements and assuming ram pressure enhancement only. These profiles are used to remove vertical dependence of these species before investigating possible horizontal/diurnal variations (see Chapter 5.3 for details).

spectrum, though they are observed in some of the outbound spectra (however, see Vuitton *et al.* 2008 for a discussion on the wall effects of C_7H_8). For H_2O , two individual inbound spectra show firm detections. The mean H_2O mixing ratio of these firm detections is 3.5×10^{-5} with a variation of 16%. For comparison, Coustenis *et al.* (2003) reported an H_2O mixing ratio of 8×10^{-9} in Titan's stratosphere (near 400 km), based on observations with the Short Wavelength Spectrometer (SWS) onboard the Infrared Space Observatory (ISO). H_2O and CO_2 are the only two oxygen compounds that are included in my spectral analysis. The prediction of these species in photochemical model calculations requires either micrometeorite influx or surficial processes such as volcanic outgassing, and more recently, precipitation of O^+ ions motivated by Cassini Plasma Spectrometer (CAPS) measurements (Hörst *et al.* 2008 and references therein).

The globally averaged density distribution of each minor component detected in Titan's upper atmosphere can be reasonably described by a power law. These power laws are shown in Fig. 5.14, which will be used in Chapter 5.3 to investigate the horizontal/diurnal variations of these species in Titan's thermosphere. The scale heights implied by these power law fittings are sometimes different from the values

Table 5.2 Globally averaged mixing ratios of various minor species, both directly obtained from the inbound measurements assuming ram pressure enhancement and with possible effects of wall adsorption/desorption corrected. The correction is based on the possible values of adsorption probability and desorption time constant that are able to reproduce the time behavior of observed chamber densities. All mixing ratios are referred to an altitude of 1,077 km or 1,025 km, and the values at other altitudes can be obtained with the condition of diffusive equilibrium.

Species	z [km]	Uncorrected	Corrected	Comment
C ₂ H ₂ /C ₂ H ₄	1,077	1.3×10^{-4}	$(3^{+2}_{-1}) \times 10^{-4}$	Fig. 5.6
C ₂ H ₆	1,025	3.2×10^{-5}	$(7^{+4}_{-2}) \times 10^{-5}$	Assuming C ₂ H ₂ /C ₂ H ₄ values
CH ₃ C ₂ H	1,077	6.1×10^{-6}	$(2^{+3}_{-1}) \times 10^{-4}$	Fig. 5.6
C ₃ H ₈	1,077	$< 2.4 \times 10^{-6}$	$< 1 \times 10^{-5}$	Assuming CH ₃ C ₂ H values
C ₄ H ₂	1,077	2.5×10^{-6}	$(3^{+4}_{-1}) \times 10^{-5}$	Fig. 5.6
C ₄ H ₆	1,077	$< 1.7 \times 10^{-7}$	$< 2 \times 10^{-6}$	Assuming C ₄ H ₂ values
CH ₃ CN	1,077	$< 1.4 \times 10^{-6}$	$< 4 \times 10^{-5}$	Assuming HC ₃ N values
C ₂ H ₃ CN	1,077	$< 2.9 \times 10^{-7}$	$< 8 \times 10^{-6}$	Assuming HC ₃ N values
HC ₃ N	1,025	1.3×10^{-6}	$(2 \pm 1) \times 10^{-5}$	Fig. 5.6

inferred from diffusive equilibrium. On one hand, this may indicate that chemical constants are typically comparable with or smaller than the diffusion time for these species. On the other hand, as I have shown in Chapter 5.1, such a feature may also be associated with possible wall effects, since the realistic instrument response varies along the spacecraft trajectory.

Next, I present the abundances of various minor species in Titan's upper atmosphere, that are corrected for the effects of wall adsorption/desorption. The correction is based on the simple model presented in Chapter 5.1, which assumes a constant adsorption probability for any given species and a desorption time constant inversely proportional to the N₂ density in the INMS chamber. The correction for C₆H₆, C₇H₈, NH₃ and C₂N₂ will not be included here since heterogeneous surface chemistry on the chamber walls is suspected to be of more importance for these species (Vuitton *et al.* 2008, see also Chapter 5.1).

The possible range of adsorption probability and desorption time constant (referred to an N₂ chamber density of 10^{11} cm^{-3}) is shown in Fig. 5.6 for several species, from which I calculate their true atmospheric abundances with the realistic instrument response function. In practice, I throw random values of p_{ads} and $t_{\text{des}}^{(\text{ref})}$

that covers the region drawn in Fig. 5.6 for the given species. I then calculate the corresponding instrument response functions for different flybys and take averages. I have shown in Chapter 5.1 that the instrument response function for the inbound measurements not too close to C/A presents the smallest scattering for different flybys and different species (see Fig. 5.7). Therefore I use the realistic instrument response at 1,077 km, averaged over all flybys, to correct for the corresponding inbound measurements at the same altitude listed in Table 5.1. The corrected mixing ratios are given in Table 5.2, where the uncertainties represent the standard deviations of all corrected values calculated for different combinations of p_{ads} and $t_{\text{des}}^{(\text{ref})}$ (within the corresponding region shown in Fig. 5.6), as well as different flybys. For other species listed in Table 5.2, I assume that their possible values of p_{ads} and $t_{\text{des}}^{(\text{ref})}$ resemble those of a similar species for which these two parameters are reasonably well constrained by the data. In more detail, I adopt the $\text{C}_2\text{H}_2/\text{C}_2\text{H}_4$ values for C_2H_6 , the $\text{CH}_3\text{C}_2\text{H}$ values for C_3H_8 , the C_4H_2 values for C_4H_6 , and the HC_3N values for all other nitriles. For C_2H_6 and HC_3N , the corrected mixing ratios are given for an altitude of 1,025 km, where an exact determination (rather than an upper limit) is available. However, the instrument response shows a large scattering at this altitude, as shown in Fig. 5.7, and thus the uncertainties of the corrected mixing ratios tend to be large, especially for C_2H_6 . Since my simple adsorption/desorption model assumes that the atmospheric distribution for any species follows diffusive equilibrium, the mixing ratios for any species listed in Table 5.2 at other altitudes can be easily obtained from their scale heights.

As two examples, I show in Fig. 5.15 the distribution of $\text{CH}_3\text{C}_2\text{H}$ and HC_3N in Titan's upper atmosphere, between 950 and 1,200 km. The dashed and dotted lines give the inbound and outbound profiles, respectively. The solid lines are calculated from the corrected mixing ratios given in Table 5.2, assuming diffusive equilibrium. Fig. 5.15 shows that the true atmospheric abundances are significantly underestimated by both inbound and outbound measurements, when taking into account ram pressure enhancement alone. Typically, the inbound values underestimate the atmospheric abundances by a factor of ~ 20 -30. However, above some altitude level,

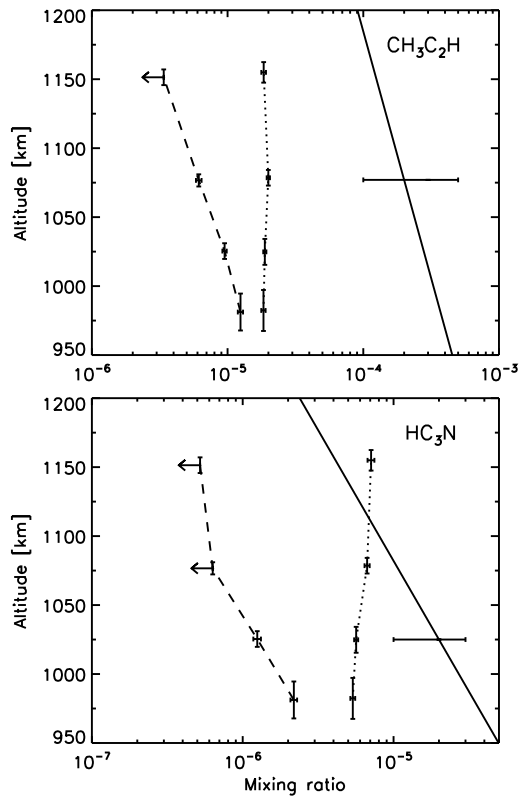


Figure 5.15 The globally averaged distribution of $\text{CH}_3\text{C}_2\text{H}$ (upper panel) and HC_3N (lower panel) in Titan's upper atmosphere. The dashed and dotted lines show the mixing ratio profiles averaged over all inbound and outbound measurements (assuming ram pressure enhancement only). The solid lines represent the profiles corrected for adsorption/desorption (see Sec 5.2.3.2 for details).

the outbound counts could overestimate the atmospheric abundances, as a consequence of the desorption of molecules accumulated on the chamber walls throughout the inbound legs. The behavior of the outbound profile depends critically on the desorption time constant, which may vary significantly for different species.

The above results on the true atmospheric abundances of various minor species in Titan's upper atmosphere are based on a simple model to describe the adsorption/desorption processes on the chamber walls. Such a model might be oversimplified for some species, e.g. C_6H_6 , C_7H_8 , NH_3 and C_2N_2 , for which wall surface chemistry is suspected to be of more importance (see Chapter 5.1). On the other hand, even in cases when the simple model does work, the possible values of the adsorption probability and desorption time constant may not be well constrained by the data, leading to considerable uncertainties associated with the correction for wall adsorption/desorption, as indicated in Table 5.2. A full investigation of the wall effects, including both adsorption/desorption and surface chemistry, will be attempted in follow-up studies. Lab experiments performed with the REU are probably required to figure out the details of the wall effects unambiguously.

5.2.4 Comparison with previous results

In this section, I compare the densities and/or mixing ratios of various neutral species based on my analysis to those given in previous works, including (1) the INMS results given by Waite *et al.* (2005) based on the TA data; (2) the early results based on the Voyager UVS solar occultation data (Vervack *et al.* 2004); and (3) the densities of several neutral species predicted from the INMS T5 observations in the OSI mode, based on a presumed ion-chemistry model (Vuitton *et al.* 2007).

First, I compare my results obtained directly from the inbound measurements (with no correction for possible wall effects) with those of Waite *et al.* (2005). Based on the INMS data acquired during the first Titan flyby, Waite *et al.* (2005) estimated the mixing ratios of several minor species with relatively high abundances. The C_2H_2 and C_2H_4 mixing ratios from Waite *et al.* (2005) are 1.9×10^{-4} and $(2.6 - 5.3) \times 10^{-4}$, at an altitude of $\sim 1,200$ km. This corresponds to a mixing ratio

of $(2.1-2.7) \times 10^{-4}$ for the *imaginary* species of $\frac{3}{4}n(\text{C}_2\text{H}_2) + \frac{1}{4}n(\text{C}_2\text{H}_4)$, about a factor of 2 higher than my value of 1.1×10^{-4} at a slightly lower altitude of 1,150 km. Their $\text{CH}_3\text{C}_2\text{H}$ mixing ratio of 3.9×10^{-6} is 40% higher than my value of 2.8×10^{-6} . The deviations between these measurements can be easily accounted for by horizontal and/or diurnal variations (see Chapter 5.3). Especially, I will present in Chapter 5.3.1 that meridional variations are tentatively identified in the sense that relatively heavy species such as $\text{CH}_3\text{C}_2\text{H}$ show enhanced mixing ratios at Titan's equatorial region. This is qualitatively consistent with the differences between the two works, since the TA trajectory covers low latitude regions near Titan's equator, while my results represent globally averaged measurements. However, the C_2H_6 mixing ratio given by Waite *et al.* (2005) is 1.2×10^{-4} at $\sim 1,200$ km, while my SVD analysis based on a much larger INMS sample only puts an upper limit of 1.8×10^{-5} . Such a considerable difference is likely due to the neglect of $^{15}\text{N}^{15}\text{N}$ in early analysis of the INMS data. For all the other minor species, Waite *et al.* (2005) declares upper limit mixing ratios of 5 ppm, consistent with my determinations. Therefore, both analyses, though based on completely different methods, reach similar results on the abundances of most minor species detected in Titan's upper atmosphere. However, it should be mentioned that the above comparison is based on densities uncorrected for any possible wall effect. In the case when processes such as adsorption/desorption are important, both results may significantly underestimate the true atmospheric abundances of some heavy species.

Previous results about the abundances of various neutral species in Titan's thermosphere have also been obtained from the Voyager UVS solar occultation observations (Smith *et al.* 1982, Vervack *et al.* 2004). The early analysis of Smith *et al.* (1982) only included N_2 , CH_4 and C_2H_2 , and their results were unable to match the UVS observations of Titan's dayglow emission (Strobel *et al.* 1982). More accurate re-analysis has been performed by Vervack *et al.* (2004), including density determination of N_2 , CH_4 , C_2H_2 , C_2H_4 , HCN , and HC_3N . The INMS data are complementary to the early Voyager UVS observations: (1) The INMS samples a relative higher altitude range in Titan's thermosphere, with a much better spatial

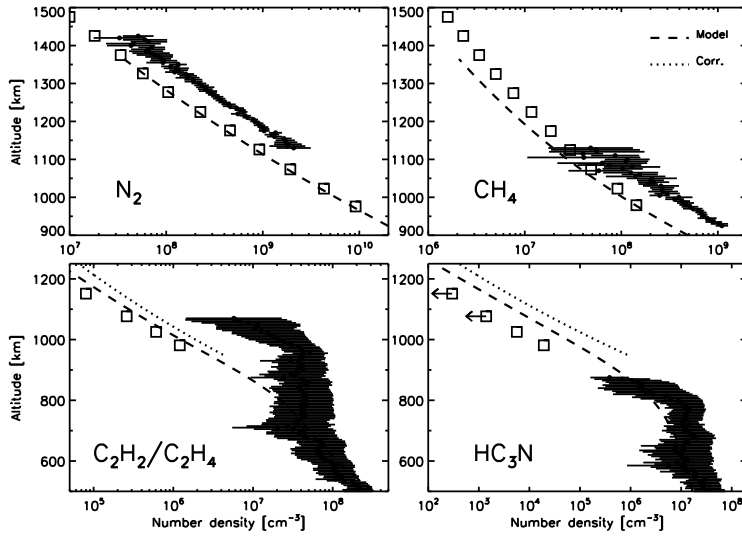


Figure 5.16 Comparison between Cassini/INMS and Voyager/UVS results of the distribution of neutral species in Titan's thermosphere. The open squares represent globally averaged mixing ratios from this work, combining data from 15 Titan fly-bys. These values are obtained by assuming ram pressure enhancement alone. The mixing ratio profiles for C_2H_2/C_2H_4 and HC_3N which are corrected for wall adsorption/desorption are shown by the dotted lines. The UVS results from Vervack *et al.* (2004) are given by the solid circles with large horizontal error bars, for comparison. Photochemical model calculations from Lavvas *et al.* (2008a, b) are shown with the dashed lines.

resolution; (2) The UVS and INMS data characterize conditions with high and low solar activities, respectively; (3) These data have different sources of uncertainty, in the sense that the interpretation of the UVS data is subject to blending between different atmospheric constituents in UV absorption, whereas the interpretation of the INMS data requires separation of the overlapping patterns in electron impact dissociative ionization.

Here I compare the INMS abundances of these species with the ingress results of Vervack *et al.* (2004), except for HCN which is not constrained by the INMS data due to crosstalk near channel 28 (see Chapter 3.6). The egress results of Vervack *et al.* (2004) are less reliable, due to the uncertainties in the solar reference spectra as well as a larger altitude range subtended by the projection of the Sun (Vervack

et al. 2004). The UVS density profiles for N_2 , CH_4 , $\text{C}_2\text{H}_2/\text{C}_2\text{H}_4$ and HC_3N are shown in Fig. 5.16, represented by the solid circles with large horizontal error bars. The INMS profiles are given by the open squares, obtained by averaging over all flybys and including inbound data only (assuming ram pressure enhancement). The leftward arrows indicate upper limits. For $\text{C}_2\text{H}_2/\text{C}_2\text{H}_4$ and HC_3N , I also show with the dotted lines their profiles corrected for wall adsorption/desorption. The dashed lines in Fig. 5.16 are adopted from the photochemical model calculations of Lavvas *et al.* (2008a, b), where I have scaled their total densities by a constant factor of 0.59 to match the INMS values. The UVS N_2 densities are about a factor of 2.5 higher than the INMS values, for overlapping altitude regions. Such a difference can be either due to uncertainties in absolute calibration or due to the long-term variations in Titan's upper atmosphere since the two missions cover a time span of over 20 years. The N_2 scale heights from both works are nearly identical, therefore giving similar values of thermospheric temperature (see Chapter 5.2.1). The CH_4 mixing ratios obtained from the UVS data are about 25% higher than the INMS values. Such a deviation cannot be due to different solar conditions, since the low solar activities appropriate for the INMS sample should lead to higher CH_4 mixing ratios as a result of large CH_4 photolysis rate. The difference in the $\text{C}_2\text{H}_2/\text{C}_2\text{H}_4$ mixing ratios is considerably larger. Compared with the direct inbound measurements (uncorrected for wall effects), the UVS values are higher by a factor of 20 and 13 at 980 km and 1025 km, respectively. Qualitatively, variations in solar activities may partly account for these differences, since a large CH_4 photolysis rate results in more efficient production of hydrocarbon molecules. Wall effects seem not strong enough to produce such a large difference, as indicated by the dotted line in the figure. Finally, no direct comparison can be made for HC_3N , since the altitude range probed by both instruments do not overlap.

Based on the INMS T5 data obtained in the OSI mode, Vuitton *et al.* (2007) derived the densities of various ion species in Titan's upper atmosphere, from which they were able to estimate the densities of related neutral species. These results, which rely on the details of the presumed ion-neutral chemistry model, can be com-

Table 5.3 Comparisons between the INMS mixing ratios obtained directly from the CSN mode and the values predicted from the ion abundances measured in the OSI mode. The OSI values are adopted from Vuitton *et al.* (2008) based on the INMS T5 measurements. The CSN values for both the inbound and outbound T5 measurements are given, along with the values corrected for wall adsorption/desorption. All densities are derived from the integrated mass spectrum between 1,030 and 1,200 km.

Species	CSN			OSI
	Inbound	Outbound	corrected	
C ₄ H ₂	$< 1 \times 10^{-6}$	5×10^{-6}	$< 1.2 \times 10^{-5}$	1×10^{-5}
CH ₃ CN	$< 2 \times 10^{-6}$	5×10^{-6}	$< 5.0 \times 10^{-5}$	3×10^{-6}
C ₂ H ₃ CN	$< 6 \times 10^{-7}$	2×10^{-6}	$< 1.6 \times 10^{-5}$	1×10^{-5}
HC ₃ N	$< 5 \times 10^{-7}$	2×10^{-6}	$< 1.3 \times 10^{-5}$	4×10^{-5}

pared with direct INMS measurements in the CSN mode. Such a comparison is detailed in Table 5.3, giving the INMS CSN densities obtained from direct SVD fits to both the inbound and outbound T5 spectra. The mixing ratios corrected for wall adsorption/desorption are based on the procedure described in Chapter 5.2.3. All mixing ratios listed in the table are for $\sim 1,100$ km, and most CSN values are upper limits at such a high altitude. I notice that the neutral abundances predicted by Vuitton *et al.* (2007) are systematically higher than direct inbound measurements in the CSN mode, by one order of magnitude (for C₄H₂) or two orders of magnitude (for HC₃N and C₂H₃CN). For some species (HC₃N and C₂H₃CN), the mixing ratios obtained from the outbound measurements are still lower by a significant amount. However, when corrected for possible effects of adsorption/desorption, the results from both works are consistent. This also suggests the possibility of correcting for possible wall effects based on a comparison between the INMS data obtained in the CSN and OSI modes. The INMS measurements in the OSI mode are not contaminated by wall effects, and the associated ion-neutral chemistry network is better understood compared with either the adsorption/desorption or the heterogeneous surface chemistry on the chamber walls.

5.3 Horizontal and diurnal variations

In this section, I investigate the neutral gas distribution with latitude, longitude and local solar time, aimed at identifying possible horizontal and/or diurnal variations in Titan's upper atmosphere.

Calculations based on the solar-driven Thermospheric Global Circulation Model (TGCM) have already inferred meridional and zonal winds in Titan's thermosphere, with speeds of order 100 m s^{-1} (Müller-Wodarg *et al.* 2008). Such a wind field is accompanied with both horizontal and diurnal variations of the atmospheric composition on Titan (Müller-Wodarg *et al.* 2002). Especially, the predicted accumulation of light species such as CH_4 near Titan's polar regions gets observational support from the INMS data (Müller-Wodarg *et al.* 2008). The thermospheric dynamics on Titan may also be driven by its interactions with Saturn's corotating plasma, which could deposit significant energy in Titan's upper atmosphere through electron/ion precipitation with a pattern that depends primarily on longitude rather than local solar time. In analogy to the solar-driven TGCM model, the interactions with the plasma environment may cause extra heating over limited ranges of longitude, drive large scale horizontal wind field, and induce redistribution of neutral gas in the thermosphere. The detailed picture of the interactions between Titan's atmosphere and Saturn's magnetosphere is still not well understood at this stage. Especially, the trajectories of heavy incident ions such as O^+ , N^+ and CH_4^+ are very complex due to their large gyroradii, and thus the energy deposit from these particles may deviate significantly from the ideal ramside (e.g. Luhmann 1996, Ledvina *et al.* 2000, Brecht *et al.* 2000). This is also true for light species in the ambient magnetosphere, such as electrons, as a result of the draped magnetic field lines (Gan *et al.* 1992).

As the dominant atmospheric constituent, the N_2 distribution provides information on the thermal structure in Titan's upper atmosphere, as described in Chapter 5.2.1. Preliminary results have been presented in De La Haye *et al.* (2007a) and Müller-Wodarg *et al.* (2008) with regards to the diurnal and horizontal variations of the thermospheric temperature. In this work, I investigate this problem further

Table 5.4 Thermospheric temperatures of Titan. ϕ , θ and t stand for latitude, longitude and local solar time, respectively. All temperatures are determined from the barometric fitting of the observed N_2 profiles averaged over the selected ranges of latitude, longitude or solar local time.

Bin definition	Temperature (K)
Global average	154.0 \pm 1.5
Low latitude, $0^\circ < \phi < 30^\circ$	156.8 \pm 1.4
Mid latitude, $30^\circ < \phi < 60^\circ$	154.1 \pm 1.5
High latitude, $60^\circ < \phi < 90^\circ$	147.2 \pm 1.5
Facing-Saturn side, $-45^\circ < \theta < 45^\circ$	154.7 \pm 1.5
Anti-Saturn side, $\theta > 135^\circ$ or $\theta < -135^\circ$	141.7 \pm 1.9
Magnetospheric ramside, $45^\circ < \theta < 135^\circ$	158.8 \pm 1.5
Magnetospheric wakeside, $-135^\circ < \theta < -45^\circ$	139.9 \pm 3.2
Dayside, $6 \text{ hr} < t < 18 \text{ hr}$	145.7 \pm 1.4
Nightside, $t < 6 \text{ hr}$ or $t > 18 \text{ hr}$	157.7 \pm 1.5

by dividing all density measurements of N_2 into several bins with different values of latitude, longitude as well as local solar time, and adopt the simple barometric model to estimate the corresponding temperature in each bin. All the model profiles are shown in Fig. 5.17. The details will be covered in the following sections. As a summary, I list all the derived temperature values in Table 5.4.

To investigate the horizontal/diurnal variations of neutral gas distribution on Titan, the simplest scheme is to divide all measurements for a given species into several bins with different ranges of latitude, longitude or local solar time. Comparisons between the average density profiles in these bins provide direct information on the horizontal/diurnal variations of the species under consideration. For CH_4 and H_2 , such a procedure is easily implemented, since the sampling of their densities, derived from the counts in their main channels, covers a large altitude range (from 950 to 1,500 km) and a high spatial resolution (~ 5.5 km) compared with most of the minor species (see also Fig. 2.1). This is also true for the N_2 distribution, used to infer the thermospheric temperature on Titan as described above. On the other hand, the density determination of most minor species relies on the SVD fits to the integrated mass spectra over certain altitude bins below 1,200 km. These species are therefore sparsely sampled, making it difficult to investigate their horizontal/diurnal variations with the procedure adopted for CH_4 and H_2 . Here I use

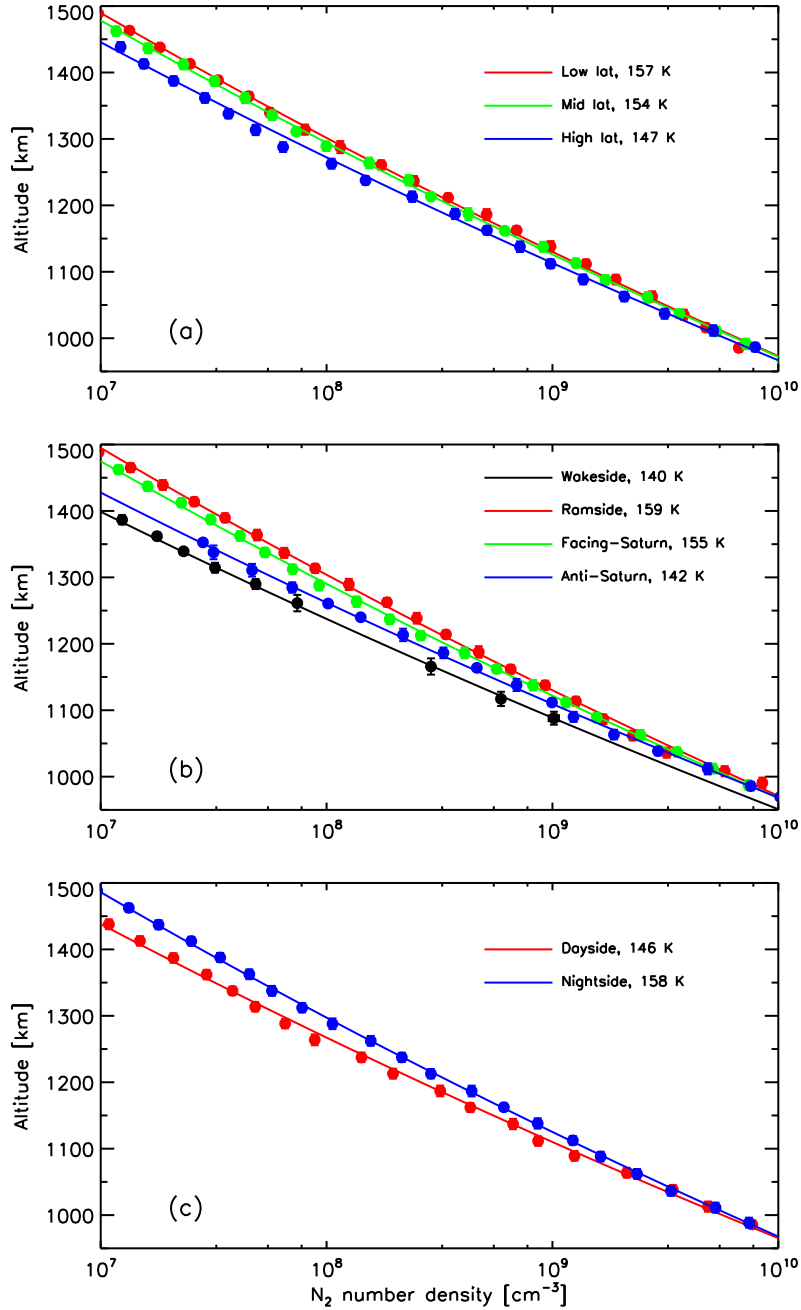


Figure 5.17 The barometric model fitting of the N_2 density distribution in Titan's upper atmosphere. Panel (a) shows the model fitting for three latitude bins over the northern hemisphere; panel (b) presents the N_2 distribution for four longitude bins; and panel (c) shows the average N_2 density profiles for the dayside and nightside, respectively. The figure implies that Titan's equatorial regions, magnetospheric ramside, as well as the nightside hemisphere are relatively warmer.

a more complicated procedure in which I correct for vertical variations by scaling all measurements of minor species to a common altitude level of 1,025 km. Such a scaling is based on the simple power law models shown in Fig. 5.14. The objective of such a procedure is to include as many individual measurements as possible, to enhance the statistical significance of my conclusions. However, the disadvantage is that the procedure introduces additional uncertainties inherent in the adopted model profiles for scaling.

To investigate the horizontal/diurnal variations of CH_4 and H_2 , comparisons should be made between density profiles as a function of pressure rather than altitude. This is aimed at removing possible effects of asymmetric atmospheric shape. Observational evidences for an asymmetric thermosphere on Titan have been reported by Müller-Wodarg *et al.* (2008). Based on an INMS sample similar to the one adopted here, they found a pronounced oblateness in Titan's thermosphere, with isobaric surfaces being ~ 45 km higher over the equator than at the north pole. Throughout this section, to examine the horizontal/diurnal variations of CH_4 and H_2 , I calculate pressure values from the ideal gas law with the measured total densities and a constant thermospheric temperature of 154 K (see Chapter 5.2.1). Though Titan's upper atmosphere is not strictly isothermal, the temperature variation of order $\sim 5\%$ (see below and Fig. 5.17) is too small to have any appreciable influence. For an investigation of the horizontal/diurnal variations of heavy species, I will not attempt to correct for possible atmospheric oblateness directly. In stead, I estimate a posteriori how significant the observed variations can be biased by this effect.

In Chapter 5.2.1, I use the diffusion model to describe the density distribution of CH_4 and H_2 . Though this is a valid procedure in a global average sense, it is not justified to apply the same model to the CH_4 and H_2 profiles obtained by averaging over a limited range of latitude, longitude and local solar time. This is because diffusion is coupled with the global circulation pattern in Titan's upper atmosphere which presents a vertical wind component of $\sim 100 \text{ m s}^{-1}$. Such a wind speed is greater than or comparable with the diffusion velocities of $1\text{--}30 \text{ m s}^{-1}$ for CH_4 and

10-200 m s⁻¹ for H₂, estimated from the best-fit fluxes given in Chapter 5.2.1 in a global average sense. To investigate quantitatively the horizontal/diurnal variations of CH₄ and H₂ diffusion/escape, the full three-dimensional kinetic model should be adopted.

In this section, I present my analysis of the variations of temperature and CH₄/H₂ mixing ratio with latitude (Chapter 5.3.1), longitude (Chapter 5.3.2) and local solar time (Chapter 5.3.3), followed by the horizontal/diurnal variations of heavy species (Chapter 5.3.4). Finally, I conclude with an assessment of the observed variations in Chapter 5.3.5.

5.3.1 Meridional variations

The meridional variation of the N₂ distribution can be used to infer the horizontal thermal structure in Titan's upper atmosphere. This has been investigated by Müller-Wodarg *et al.* (2008) based on their empirical model of Titan's thermosphere, constructed from a large INMS sample nearly identical to the one adopted here. In their work, a two-dimensional temperature field was derived by integrating the hydrostatic equation downward at each latitude and then calculating temperature from the ideal gas law (see also Müller-Wodarg *et al.* 2006). Such a temperature field is characterized by warmer equatorial regions and cooler polar regions, consistent with predictions of solar heating models (Müller-Wodarg *et al.* 2008). Here, I divide the INMS sample into three latitude bins, at 0°-30°N, 30°-60°N and 60°-90°N respectively. I use the simple barometric relation to fit the average N₂ distribution in each bin, and the best-fit thermospheric temperature decreases from 156.8 ± 1.5 K for the low latitude bin, to 154.1 ± 1.5 K for the mid latitude bin, and to 147.2 ± 1.4 K for the high latitude bin. Therefore both works, though based on different procedures of deriving temperature, reach a consistent result that the equatorial regions in Titan's thermosphere appear to be warmer and the polar regions are cooler, with a temperature difference between the equator and north pole of ~ 10 K. The model profiles for different latitude bins are shown in Fig. 5.17a.

Similarly, I investigate the CH₄ and H₂ density profiles averaged over the lati-

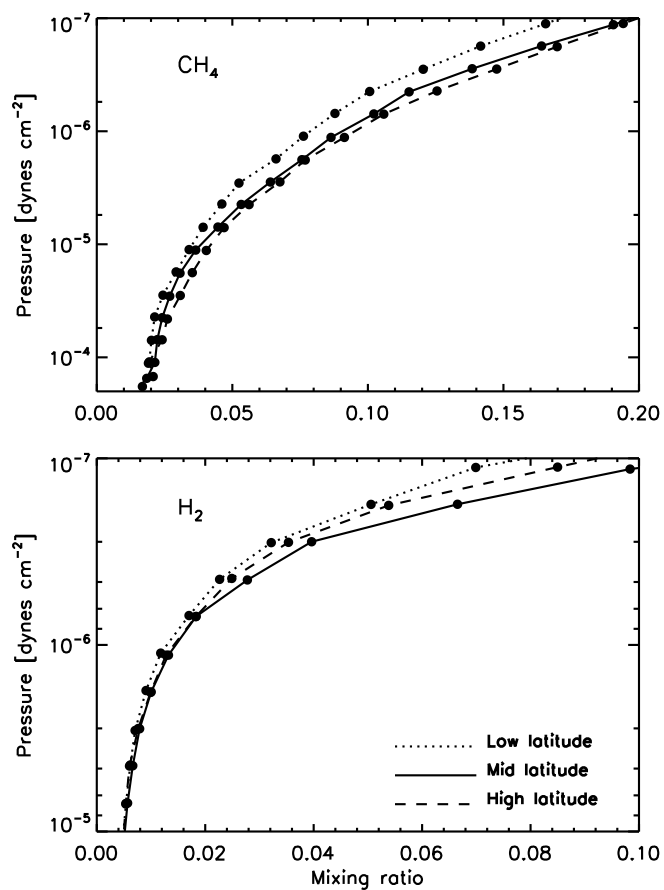


Figure 5.18 The average profiles of CH_4 mixing ratio in Titan's upper atmosphere for three latitude bins, defined as 0° - 30°N for the low latitude bin, 30°N - 60°N for the mid latitude bin and 60°N - 90°N for the high latitude bin. The figure shows depletion of CH_4 near the equator and accumulation of CH_4 near the north pole. The meridional variation of H_2 shows a more complicated pattern, with enhanced abundances at mid latitudes.

tude bins defined above. Differences between these profiles are clearly seen in Fig. 5.18. The CH_4 distribution shows accumulation near the polar regions and depletion near the equatorial regions, confirming the results of Müller-Wodarg *et al.* (2008). The difference in the observed CH_4 mixing ratios between the equatorial and polar regions is about 20% at a pressure level of $\sim 1.7 \times 10^{-7}$ dynes cm^{-2} (or near Titan's exobase). Such a feature has been interpreted as upwelling motion near the equator and downwelling motion near the north pole, in response to the horizontal transport by thermospheric winds (Müller-Wodarg & Yelle 2002, Müller-Wodarg *et al.* 2003). Meridional variation is also observed for H_2 , as shown in the lower panel of Fig. 5.18. However, the observed H_2 mixing ratio peaks at mid latitudes, and decreases toward both the equator and north pole. Near the exobase, the average H_2 mixing ratio for the mid latitude bin is about 20% higher than the polar value and 30% higher than the equatorial value. Such a feature is likely to be associated with the rapid thermal escape and large ballistic flow of H_2 in Titan's exosphere. Clearly, escape tends to enhance depletion near the equator but counteract accumulation near the north pole. As mentioned above, a thorough investigation of this issue requires a three-dimensional modeling of the global circulation pattern in Titan's thermosphere that also includes the effect of escape.

From Fig. 5.18, the magnitude of meridional variations of both CH_4 and H_2 decreases at low altitudes or high pressure levels. Especially, no variation with latitude appears to be present for H_2 below $\sim 2 \times 10^{-6}$ dynes cm^{-2} (at $\sim 1,300$ km). On the contrary, the meridional variation of CH_4 is observable down to 1×10^{-4} dynes cm^{-2} (at $\sim 1,000$ km).

The meridional variations presented above are obtained from the neutral gas distribution over Titan's northern hemisphere, where the majority of the INMS measurements adopted in this work were made. Without constraints from measurements in the southern hemisphere, symmetry is usually assumed about Titan's equator (e.g. Müller-Wodarg *et al.* 2008). Although the INMS sample contains two flybys (T36 and T37) that probe Titan's southern hemisphere, the sample coverage is still too limited to allow robust conclusions to be made with regards to the

differences between Titan's northern and southern hemispheres. A thorough investigation of this issue can be attempted with the release of data to be obtained in the extended Cassini mission.

5.3.2 Zonal variations

I first investigate possible zonal variation of the thermospheric temperature by considering the N_2 distribution averaged in different longitude bins. Here, I consider four longitude sectors, one for $-45^\circ < \theta < 45^\circ$ (facing-Saturn side), one for $\theta > 135^\circ$ or $\theta < -135^\circ$ (anti-Saturn side), one for $-135^\circ < \theta < -45^\circ$ (magnetospheric wake-side), and one for $45^\circ < \theta < 135^\circ$ (magnetospheric ramside). The most probable thermospheric temperatures obtained from barometric fitting in these bins are 154.7 ± 1.5 K (for the facing-Saturn side), 141.7 ± 1.9 K (for the anti-Saturn side), 139.9 ± 3.2 K (for the wakeside) and 158.8 ± 1.5 K (for the ramside), respectively. These values are also listed in Table 5.4, and the model fits are shown in Fig. 5.17b. The above analysis implies that the magnetospheric ramside and facing-Saturn side of Titan appear to be warmer than the wakeside and anti-Saturn side. This may imply extra heating of Titan's upper atmosphere through precipitation of energetic electrons/ions preferentially over the ramside and facing-Saturn side. The temperature on the facing-Saturn side is close to the global average value of 154 K given in Chapter 5.2.1. However, this does not necessarily have any physical implication since the INMS sample preferentially select measurements made on this side (see Fig. 2.1). I also notice that Titan's wakeside is poorly sampled, with measurements below 1,100 km and between 1,170 and 1,250 km not available as shown in Fig. 5.17b. Therefore the interpretation of a cooler wakeside on Titan deserves some caution (see also Chapter 5.3.5 below).

Next I investigate the zonal variations of the CH_4 and H_2 distribution, using their abundances obtained directly from counts in the main channels between 950 and 1,500 km. Only measurements made over the northern hemisphere are included, to avoid possible asymmetry about the equator (see above). The CH_4 profiles averaged over the four longitude sectors defined above are shown in the upper panel

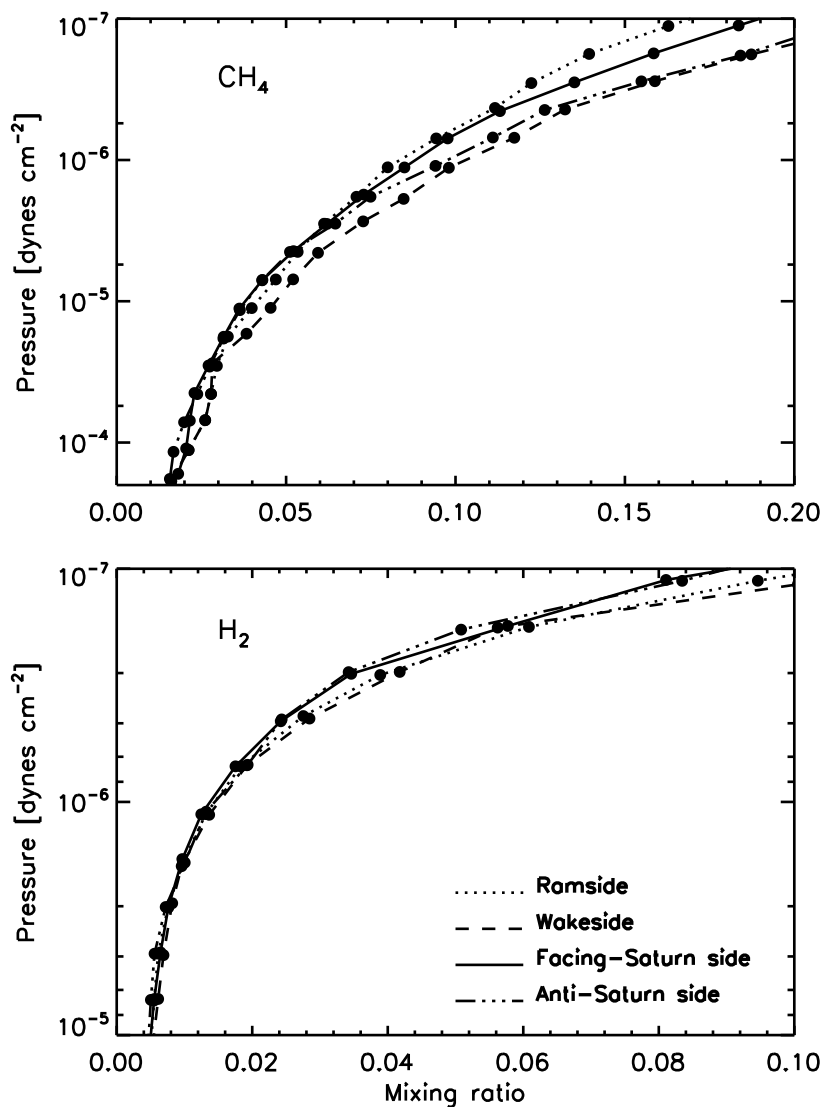


Figure 5.19 The average profiles of CH_4 and H_2 mixing ratios in Titan's upper atmosphere for four longitude sectors, denoted as the magnetospheric ramside and wakeside, as well as the facing-Saturn side and anti-Saturn side, each spanning a longitude range of 90° . For CH_4 , the figure shows depletion at Titan's ramside and facing-Saturn side, as well as accumulation at the wakeside and anti-Saturn side. The zonal variation of H_2 shows a more complex pattern.

of Fig. 5.19. From the figure, CH_4 appears to be depleted at both the ramside and facing-Saturn side, but accumulated at the wakeside and anti-Saturn side. Such a trend is clearly seen above $1 \times 10^{-6} \text{ dynes cm}^{-2}$ (at $\sim 1,350 \text{ km}$). Along with the variation of temperature with longitude described above, the observed zonal variation of CH_4 distribution can be accommodated with the scenario of plasma-driven thermospheric dynamics, in which light species always present depletion in warmer regions (ramside and facing-Saturn side) and accumulation in cooler regions (wakeside and anti-Saturn side).

As shown in the lower panel of Fig. 5.19, significant zonal variation is also observed for H_2 , suggesting accumulation at both the ramside and wakeside. Clearly, the zonal variations of CH_4 and H_2 do not show a similar pattern. Analogous to the observed meridional variation of H_2 , it is likely that both escape and large ballistic flows in the exosphere have significant effects, leading to more complicated horizontal structures for H_2 (both meridional and zonal). In addition, all H_2 profiles appear to be identical below $\sim 2 \times 10^{-6} \text{ dynes cm}^{-2}$ (at $\sim 1,300 \text{ km}$). I note that the meridional variation of the same species becomes absent at about the same level (see Fig. 5.18).

5.3.3 Diurnal variations

In this section, I investigate possible diurnal variations of thermal structure and gas distribution in Titan's upper atmosphere. Based on the INMS data acquired during the TA, TB and T5 flybys, De La Haye *et al.* (2007a) found a thermospheric temperature of $\sim 5 \text{ K}$ higher at night than at dusk on Titan. Here I extend the analysis to a much larger INMS sample. I divide all N_2 density measurements into two sectors, one for the dayside and the other one for the nightside. The barometric fitting of the N_2 density profiles, averaged over all flybys but constrained within the two selected sectors, are shown in Fig. 5.17c. For the dayside N_2 distribution, I obtain a best-fit temperature of $145.7 \pm 1.4 \text{ K}$, while for the nightside, I get $157.7 \pm 1.5 \text{ K}$. With significantly improved statistics, my analysis confirms the result of De La Haye *et al.* (2007a) that Titan's sunlit side presents a lower thermospheric

temperature. Such a trend is clearly in opposite to the predictions of any solar-driven model.

I further examine the diurnal variations of CH_4 and H_2 distribution in Titan's upper atmosphere. Solar-driven TGCM models predict horizontal thermospheric winds of $\sim 100 \text{ m s}^{-1}$ (Müller-Wodarg *et al.* 2008). Since the associated dynamical time constant (of order 10^5 s) is much shorter than the photochemical time constants of CH_4 and H_2 , the horizontal wind field may produce accumulation of these light species on Titan's nightside. On the other hand, if the horizontal winds are primarily driven by the ambient plasma, such a feature may be absent.

The CH_4 and H_2 density profiles averaged over the dayside and nightside hemispheres are shown in Fig. 5.20. Clear diurnal variations are seen, with both species depleted at the nightside and accumulated at the dayside. Such a feature can be accommodated with the temperature difference between the dayside and nightside hemispheres described above, in the sense that the warmer side is always associated with depletion of light species, and the cooler side associated with accumulation. However, the diurnal variations observed for these species are contradictory to the predictions of solar-driven models, in which light species are depleted at the dayside and accumulated at the nightside. I will return to this issue in Chapter 5.3.5.

5.3.4 Horizontal/diurnal variations of heavy species

In Chapter 5.2.3, I present my analysis of the abundances of various hydrocarbons, nitriles and oxygen compounds in Titan's upper atmosphere, both in terms of the direct inbound measurements adopting the 'ideal' ram enhancement factor and in terms of the corrected values taking into account the processes of adsorption/desorption on the chamber walls. In this section, I describe my investigation of the horizontal/diurnal variations of these minor species, based on the values directly obtained from the inbound measurements. A similar investigation based on the values corrected for wall effects will not be discussed here, since the values of the adsorption probability and desorption time constant are not well constrained in this study (see Fig. 5.6), and thus the uncertainties of the corrected abundances are

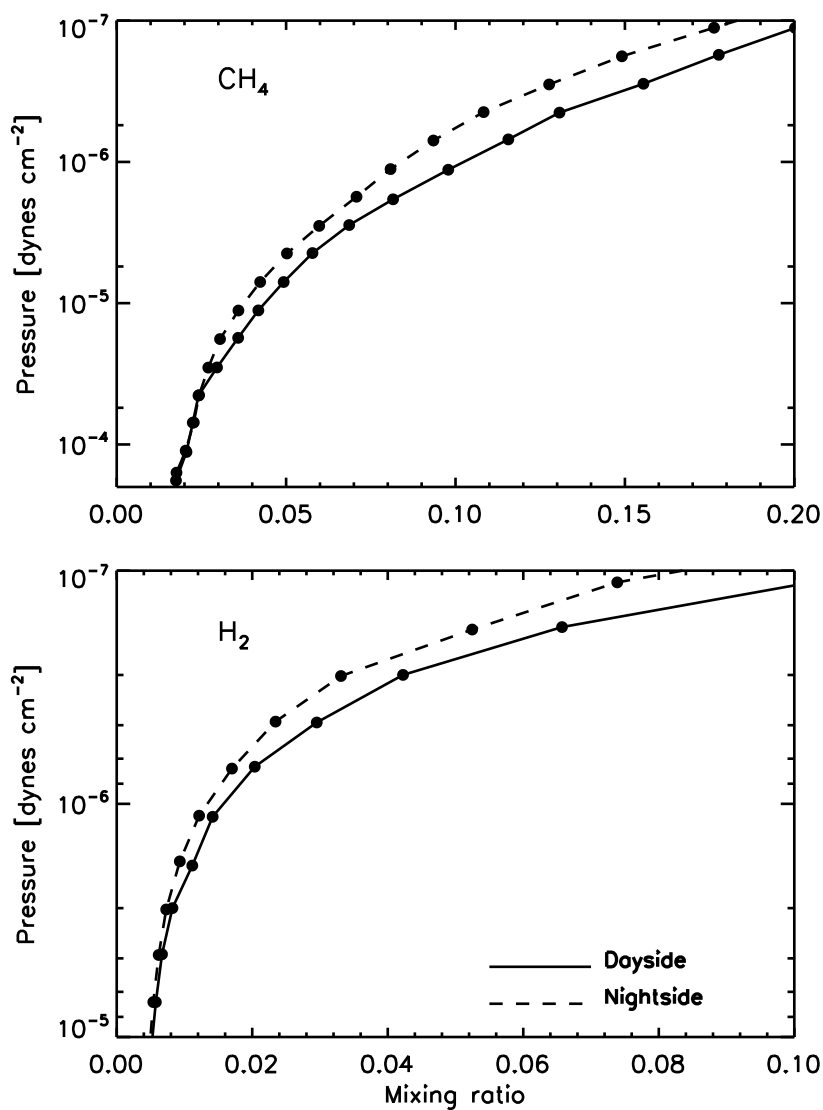


Figure 5.20 The average profiles of CH_4 and H_2 mixing ratios for Titan's dayside and nightside hemispheres. For both species, depletion over the nightside and accumulation over the dayside can be observed.

large. In fact, I find that for some combination of the adsorption probability and desorption time constant, significant horizontal/diurnal variations are present for the corrected abundances of several species, while the same feature becomes absent for other choices of p_{ads} and $t_{\text{des}}^{(\text{ref})}$. Despite of this difficulty, I will present in Chapter 5.3.5 a qualitative assessment of the observed variations of heavy species, taking into account possible wall effects.

Based on the direct inbound measurements, the meridional variations of several representative minor species are shown in Fig. 5.21, including ^{40}Ar , $\text{C}_2\text{H}_2/\text{C}_2\text{H}_4$, C_4H_2 , C_6H_6 , HC_3N and $\text{CH}_3\text{C}_2\text{H}$. Downward arrows indicate 3σ upper limit measurements. Here the analysis is restricted to the northern hemisphere, due to the incomplete latitude coverage in the southern hemisphere. All measurements have been scaled to a common altitude of 1,050 km based on the simple power law fitting shown in Fig. 5.14. These scaled mixing ratios are shown by the open circles in Fig. 5.21. For comparison, direct INMS measurements based on SVD fits between 1,025 and 1,075 km are overplotted with the solid circles. All species shown in Fig. 5.21 are heavier than N_2 , and have smaller scale heights. In general, their meridional variations show depletion at high latitudes, consistent with the prediction of subsidence near polar regions driven by horizontal wind field in Titan's thermosphere. The same feature is also confirmed for C_2N_2 , which is not shown in the figure. However, it is interesting to note that no significant meridional variation is observed for ^{40}Ar , which is an inert species and whose distribution is controlled by dynamics and diffusion only.

More quantitatively, I calculate the rank order correlation coefficients for each heavy species, based on the model independent Kendall's- τ test (Press *et al.* 1992). The correlation coefficients between absolute latitude and mixing ratio are listed in Table 5.5, along with the significance levels of their deviations from zero, representing null hypothesis. Upper limits are not included in evaluating the correlation coefficients. From Table 5.5, except for ^{40}Ar , all species show some trend of anti-correlation with latitude, at more than 3σ significance level. As mentioned above, such a behavior is consistent with the prediction of subsidence near polar regions

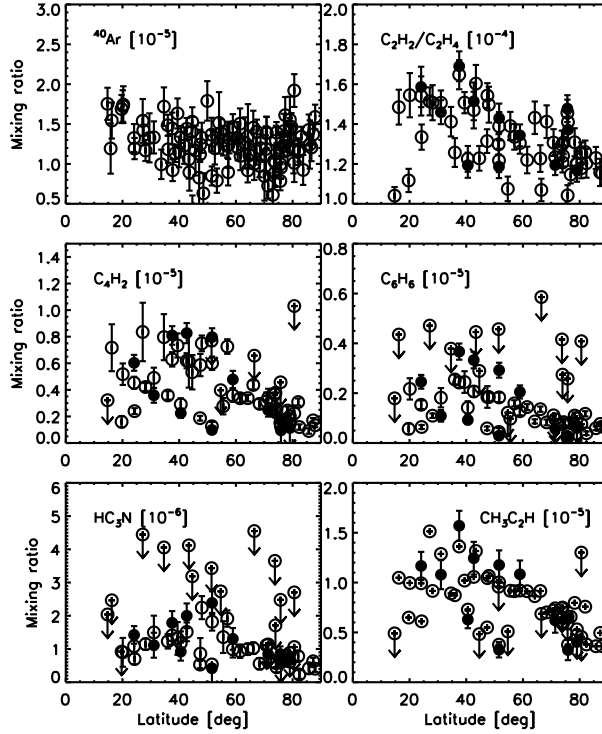


Figure 5.21 The meridional variations of several representative minor species in Titan's upper atmosphere. All measurements have been scaled to a common altitude of 1,050 km. These scaled mixing ratios are given by the open circles. For comparison, the solid circles represent the directly measured mixing ratios between 1,025 and 1,075 km based on SVD fits. Downward arrows indicate 3σ upper limit measurements. All species, except for ^{40}Ar , show some signature of depletion near polar regions. The mixing ratios presented in the figure are obtained by assuming ram pressure enhancement, and no correction for wall adsorption/desorption is made.

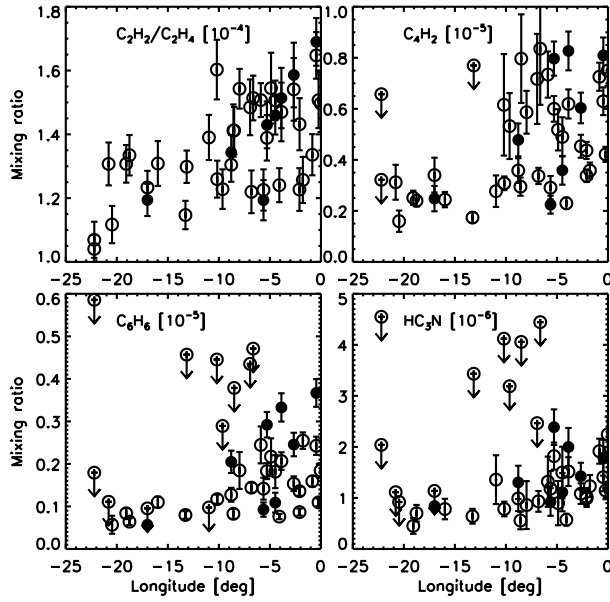


Figure 5.22 The zonal variations of several heavy species in Titan’s upper atmosphere. Drawing conventions are the same as Fig. 5.21. These species show a trend of accumulation toward zero longitude. However, such a feature is likely to be an observational bias caused by wall effects (see Chapter 5.3.5 for details).

by solar-driven TGCM models (Müller-Wodarg *et al.* 2008).

Next I investigate the zonal variations of heavy species. In analogy to the observed zonal variations of CH_4 distribution (see Chapter 5.3.2), the plasma-driven thermospheric dynamics on Titan may also induce accumulation/depletion of heavy species over limited ranges of longitude. Two possibilities are explored here, assuming that energy deposit through precipitating ions/electrons primarily take place at the facing-Saturn side or magnetospheric ramside of Titan. These two choices are suggested by the observed zonal variations of thermospheric temperature as well as CH_4 distribution. For the first case, I perform Kendall’s- τ tests between the derived mixing ratios and absolute longitude values, $|\theta|$. The corresponding correlation coefficients are listed in the 3rd column of Table 5.5, which shows that most heavy species are accumulated near zero longitude. However, the same trend is not observed for the inert species, ^{40}Ar . For the second case, I calculate the correlation

coefficients between mixing ratios and $|\theta - 90^\circ|$. These coefficients are given in the 4th column of Table 5.5, suggesting no zonal variation for all heavy species.

According to the above analysis, significant zonal variations for the distribution of heavy species are presented in terms of a trend of accumulation near zero longitude, except for ^{40}Ar . This feature is shown in Fig. 5.22 for several representative species (restricted to regions between -25° and 0°), with all mixing ratios scaled to a common altitude level of 1,050 km. At the face value, accumulation of heavy species near zero longitude can be accommodated with the scenario of plasma-driven dynamics in Titan's upper atmosphere with precipitation of energetic electrons/ions primarily on the facing-Saturn side of Titan. However, such a conclusion deserves some skepticism, since the observed zonal variations of heavy species primarily rely on data obtained near zero longitude, as shown in Fig. 2.1. Constraining the analysis to inbound measurements further reduces the sample size, covering mostly the longitude range between -30° and 0° . For heavy species, very few measurements are available on either the anti-Saturn side or the magnetospheric ramside and wakeside, making it difficult to justify the observed trend over a larger scale. In fact, what is most surprising is that the zonal variations of heavy species are present over such a small longitude range that covers less than 10% of the entire surface of Titan. However, I will show in Chapter 5.3.5 that these observed zonal variations are likely to be contaminated by the wall effects.

Finally, I perform Kendall's- τ test for possible diurnal variations of heavy species. The corresponding correlation coefficients are given in Table 5.5, calculated between the mixing ratio and $|h - 12|$ where h is the local solar time in hour. No significant correlation or anti-correlation is found for any species.

5.3.5 Reliability check of the observed horizontal/diurnal variations

In the previous sections, I discuss possible horizontal and diurnal variations of the thermal structure and neutral gas distribution in Titan's upper atmosphere above 950 km. However, the sample distribution with respect to latitude, longitude and local solar time may not be independent. This may introduce observational biases

Table 5.5 Kendall's- τ correlation coefficients. The numbers in the parenthesis are the significance levels of the Kendall's- τ correlation coefficients that deviate from a null hypothesis. The correlation coefficients are calculated between mixing ratio and latitude in the northern hemisphere (meridional), between mixing ratio and absolute longitude relative to the facing-Saturn side, $|\theta|$ or the ideal ramside, $|\theta - 90^\circ|$ (zonal), and between mixing ratio and $|h - 12|$, where h is the local solar time in hr (diurnal).

Species	Meridional	Zonal		Diurnal
	ϕ	$ \theta $	$ \theta - 90^\circ $	$ h - 12 $
C ₂ H ₂ /C ₂ H ₄	-0.37 (3.8)	-0.35 (3.9)	-0.17 (2.0)	+0.15 (1.6)
CH ₃ C ₂ H	-0.56 (5.2)	-0.42 (4.1)	-0.03 (0.3)	+0.18 (1.8)
C ₄ H ₂	-0.40 (3.7)	-0.55 (5.4)	-0.23 (2.3)	+0.11 (1.1)
C ₆ H ₆	-0.36 (3.0)	-0.43 (3.7)	-0.08 (0.7)	+0.05 (0.4)
HC ₃ N	-0.38 (3.0)	-0.58 (4.9)	-0.06 (2.7)	+0.13 (1.1)
C ₂ N ₂	-0.34 (3.0)	-0.36 (3.3)	-0.13 (1.2)	+0.10 (0.9)
⁴⁰ Ar	-0.10 (1.5)	-0.09 (1.3)	+0.13 (2.0)	+0.13 (2.1)

to the analysis of horizontal/diurnal variations, which have to be examined carefully when interpreting the data. For example, in the case when daytime measurements also preferentially select measurements made over the magnetospheric ramside, then in principle we cannot distinguish between the solar-driven model and the plasma-driven model (assuming precipitation of energetic ions/electrons is primarily on the ramside).

The observed horizontal/diurnal variations of heavy species are subject to some additional uncertainties. First, in my analysis, I scale their local densities with the simple power laws (see Fig. 5.14). Such a procedure introduces additional uncertainties into the observed variations, associated with the deviation of the true distribution from the power law. Second, strictly speaking, the power-law scaling to a common altitude of 1,050 km rather than a common pressure level implicitly assumes that Titan's thermosphere is spherically symmetric. However, such an assumption may not be valid (Müllwer-Wodarg *et al.* 2008) and the observed horizontal variations of heavy species might be contaminated by the actual atmospheric shape. Finally, as mentioned above, though it is difficult to investigate the variations of heavy species based on the abundances corrected for wall adsorption/desorption (since the parameters, p_{ads} and $t_{\text{des}}^{(\text{ref})}$, are usually not well constrained), the possible contamination of the observed variations by wall effects has to be assessed at least

in a qualitative sense.

First, I investigate whether the observed horizontal/diurnal variations of heavy species are reliable. These variations can be summarized as depletion near polar regions and accumulation toward zero longitude, but no apparent correlation with local solar time. The density determination for these species relies exclusively on the SVD analysis of inbound data, and only measurements below 1,200 km are considered.

Based on the Kendall's- τ test, I find that the sample distribution in latitude, longitude and local solar time is independent. This implies that the horizontal/diurnal variations of heavy species revealed by the INMS data are not very likely to be biased by selective sampling with respect to these parameters.

In terms of the meridional variations of heavy species, the effect of thermospheric oblateness (Müller-Wodarg *et al.* 2008) is a major concern. Qualitatively, the isobaric surfaces near the equator are higher, implying an overestimate of the heavy species abundances at low latitudes as shown in Fig. 5.21, since I scale all measurements to the same altitude rather than a common pressure level when discussing the horizontal/diurnal variations (see above). Fig. 5.13 shows that the mixing ratio of the *imaginary* species, $\frac{3}{4}n(\text{C}_2\text{H}_2) + \frac{1}{4}n(\text{C}_2\text{H}_4)$, remains roughly constant between 950 and 1,200 km, due to the fact that its scale height is close to the N_2 scale height. Therefore, the observed $\text{C}_2\text{H}_2/\text{C}_2\text{H}_4$ depletion near the north pole may not be significantly affected by the atmospheric shape. In the other extreme case, C_6H_6 presents the strongest altitude dependence in Fig. 5.13. The C_6H_6 scale height is roughly 28 km based on the power law fitting shown in Fig. 5.14, and the scale height of the background atmosphere is ~ 65 km. These give a 60% difference in the C_6H_6 mixing ratio over a vertical extent of 45 km, corresponding to the altitude difference along the isobar between the equator and north pole (Müller-Wodarg *et al.* 2008). From Fig. 5.21, the C_6H_6 depletion at the north pole appears to be more than a factor of 4, compared with the measurements made near the equator. Therefore, the effect of thermospheric oblateness may not be strong enough to offset the observed meridional variation of C_6H_6 . Similar calculations performed to

other species give a mixing ratio difference of 6% for $\text{C}_2\text{H}_2/\text{C}_2\text{H}_4$, 17% for C_2H_6 and C_2N_2 , 33% for $\text{CH}_3\text{C}_2\text{H}$, 39% for C_4H_2 and 27% for HC_3N . By comparing with Fig. 5.21, the analysis above suggests that my previous conclusion on the general depletion of heavy species near Titan's north pole may not be strongly affected by the atmospheric shape. However, it should be born in mind that the above analysis assumes an altitude difference of 45 km along the isobar between the equator and north pole (Müller-Wodarg *et al.* 2008). Whether or not the observed meridional variation can be counteracted by the effect of atmospheric oblateness is sensitive to the choice of this value, especially for those species with strong altitude dependence. Based on the observed N_2 distribution shown in Fig. 5.17a, I can roughly estimate an altitude difference between the equator and north pole of $\sim 30\text{--}40$ km along the isobar, not too far from the value given by Müller-Wordag *et al.* (2008). I find that in the extreme case of C_6H_6 , the meridional variation may no longer be present, even if the actual altitude difference along the isobar is only 25% higher than the value of Müller-Wordag *et al.* (2008). In contrast, the meridional variation of $\text{C}_2\text{H}_2/\text{C}_2\text{H}_4$ is still discernible, even if isobaric surfaces are hundreds of km higher at the equator than at the north pole (which is unrealistic). Considering this, I have more confidence with the observed depletion of $\text{C}_2\text{H}_2/\text{C}_2\text{H}_4$ near Titan's north pole, whose mixing ratios do not strongly vary with altitude.

Next, I check for possible biases caused by wall effects. I find that longitude is correlated with time from C/A at 7.5σ significance level, estimated from the Kendall's- τ test. This implies that measurements made near zero longitude also concentrate near C/A when the contamination by wall effects becomes less serious. This can be easily seen from Fig. 5.7, which shows that along the inbound portion of the spacecraft trajectory, the realistic instrument response increases toward the 'ideal' ram enhancement factor near C/A. This also implies that the mixing ratios obtained from direct SVD fits to the inbound mass spectra near C/A are closer to the true atmospheric values, while those away from C/A are likely to be more serious underestimates. I have shown in Chapter 5.3.4 that the mixing ratios of heavy species tend to increase toward zero longitude, which according to the analysis here,

might simply be an observational bias caused by wall adsorption/desorption. The fact that zonal variation is not observed for the ^{40}Ar distribution further supports this point, since wall effect is not involved for this species (see Fig. 5.1). The same argument may not hold for the meridional variations of heavy species, since the spacecraft approaches Titan from a wide range of latitude covering the whole northern hemisphere and part of the southern hemisphere, with the sample distribution in latitude independent of time from C/A.

In the context of wall effects, the observed meridional variations of two species, C_6H_6 and C_2N_2 are likely subject to contamination by the heterogeneous surface chemistry on the chamber walls (see Chapter 5.1). Without a detailed modeling of the wall surface chemistry, it is not possible to predict their mixing ratios in the ambient atmosphere, and therefore the interpretation of the observed meridional variations of these two species deserves caution. Fortunately, as mentioned in Chapter 5.1, surface chemistry may not be important for other heavy species that are analyzed here, and the simple processes of adsorption/desorption on the chamber walls may only invalidate the observed zonal variations, with the conclusion on their meridional variations (depletion near the north pole) remaining unaffected.

Finally, the simple power law fitting shown in Fig. 5.14 contributes to additional uncertainties in the observed horizontal/diurnal variations of heavy species. Based on the scattering of the globally averaged densities around the best-fit power relation, I estimate for each heavy species the uncertainty associated with the simple power law fitting, characterized by a mean fractional variation. The largest uncertainty appears for C_6H_6 , with a fractional variation of 6%. I examine 5,000 random realizations, each adopting a power law profile randomly fluctuated by 6% on average around the best-fit relation shown in Fig. 5.14. These random power laws are used to scale the observed C_6H_6 mixing ratios to a common altitude of 1,050 km. I then perform Kendall's- τ test on these random samples, to investigate possible meridional variation of C_6H_6 . I find that 98% of the random realizations show evidences for the depletion of C_6H_6 at more than 3σ significance level. By applying such an analysis to all heavy species, I conclude that the results on the horizon-

tal/diurnal variations of heavy species are not strongly affected by the uncertainties associated with the simple power law fitting.

I further check the reliability of the horizontal/diurnal variations of the distribution of light species as well as temperature, presented in Chapter 5.3.1-5.3.3. Here the contamination by atmospheric shape is not a concern for the observed CH_4 and H_2 variations, since throughout my analysis, I investigate their profiles as a function of pressure rather than altitude. Also, no model dependent scaling is applied to these light species, indicating that the additional uncertainties associated with average vertical profile fitting is not a worry either. Along with the insignificance of wall effects for these abundant species, the potential source of uncertainty comes from selective sampling with respect to latitude, longitude and local solar time. For the variations of light species, I will concentrate on CH_4 only, since I have mentioned above that the variations of H_2 present a more complex pattern, probably due to the rapid thermal escape as well as large ballistic flow in Titan's exosphere for this species.

First, I notice that the dayside hemisphere discussed in Chapter 5.3.3 also preferentially selects high latitude measurements with a distribution peaking at $\sim 75^\circ\text{N}$, as shown in the lower panel of Fig. 5.23. This indicates that the observed diurnal temperature variation, represented by a warmer nightside on Titan, may simply be a side-effect of the meridional variation due to biased samplings of the dayside and nightside hemispheres. Similarly, the observed diurnal variation of CH_4 , as shown in Fig. 5.20, might be explained by the same argument, since the dayside hemisphere where enhanced mixing ratios are observed for CH_4 is coincident with high latitude regions where accumulation of light species is expected.

I also find that the latitude distribution in different longitude sectors are not exactly identical, as shown in the upper panel of Fig. 5.23. On one hand, both the wakeside and anti-Saturn side of Titan significantly overlap with high latitude regions. Especially, all measurements over the wakeside are made near 80°N . This implies that the lower thermospheric temperature, as well as CH_4 accumulation, obtained for these longitude sectors may simply reflect an observational bias due

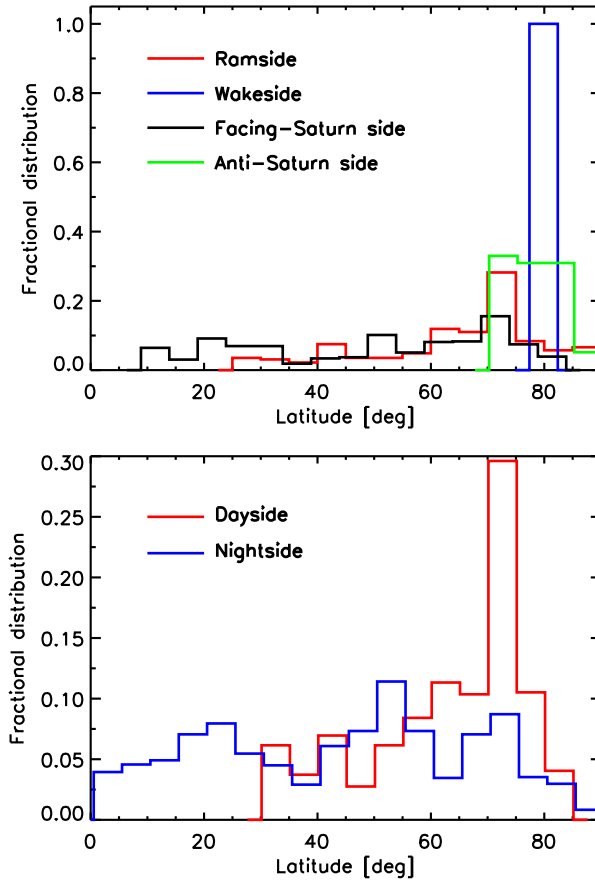


Figure 5.23 Upper panel: A comparison between the latitude distribution for Titan's ramside, wakeside, facing-Saturn side and anti-Saturn side. Both the wakeside and anti-Saturn side are strongly biased toward high latitude regions. Lower panel: the latitude distribution for Titan's dayside and nightside hemispheres. The dayside sector preferentially selects measurements made near polar regions.

to the fact that Titan's polar regions are cooler. On the other hand, Titan's ramside covers the entire northern hemisphere, suggesting that the observations of a warmer ramside on Titan are probably realistic, as compared with the global average temperature. Also notice that from Fig. 5.23, the ramside sector has some preferences for selecting measurements made at high latitudes, though such a bias is not significant. However, even with such a selective sampling taken into account, my conclusion with regards to Titan's ramside is still valid, since the meridional variations tend to counteract (rather than enhance) the observed zonal variations, implying that the effects of a warmer ramside with CH_4 depletion are probably more striking than those shown in Fig. 5.17b and 5.19.

The above analysis is based on an inherent assumption that the meridional variations of temperature and CH_4 distribution presented in Chapter 5.3.1 are real physical features (e.g. Müller-Wodarg *et al.* 2008). In principle, it is also possible to accommodate the observed variations into an alternative scenario in which Titan's wakeside and anti-Saturn side are cooler. With such an assumption, the lower temperature obtained near the north pole turns out to be an observational bias due to restricted sampling. A third possibility is that a cooler dayside in Titan's thermosphere is a real feature (though may not be physically motivated), and the observations of both cooler polar regions and cooler wakeside or anti-Saturn side are observational biases. Probably the only tentative conclusion that can be made directly based on the INMS sample is that Titan's ramside is warmer than global average, with some evidence for CH_4 depletion.

The analysis of the horizontal/diurnal variations presented here is aimed at identifying whether the thermal structure and gas distribution in Titan's upper atmosphere is driven by solar EVU photons or by precipitating ion/electrons from the ambient plasma. As I have mentioned above, the former suggests a pattern that varies with local solar time, while the latter suggests a pattern that varies with longitude. For the meridional variations, the solar-driven model predicts a warmer equator with CH_4 depletion (Müller-Wodarg *et al.* 2000, 2003), which is also revealed by my analysis here. However, the meridional variations are not easily pre-

dicted in the framework of plasma-driven models, since whether the precipitation of electrons/ions is preferentially near the equatorial or polar regions is not firmly established. While my analysis does suggest tentatively that Titan's ramside appears to be warmer than the global average with some signature of CH₄ depletion, a solid assessment of the importance of plasma-driven energetics and dynamics in Titan's upper atmosphere requires a full investigation that reconciles all the observed horizontal/diurnal variations. For example, one need to answer the question whether the observation of cooler polar regions on Titan is simply a side-effect of cooler wakeside and anti-Saturn side, or is a realistic feature as predicted by solar-driven TGCM models. In the latter case, the energetics and dynamics in Titan's thermosphere is driven by both solar EUV photons and precipitating electrons/ions from the ambient plasma.

To disentangle the couplings between different models, the key might be additional information on Titan's thermosphere obtained near the equator and simultaneously on the wakeside or anti-Saturn side. Such a dataset does exist, though in Titan's southern hemisphere: Below 1,500 km, the T37 flyby covers Titan's low latitude regions near 20°S, over Titan's wakeside and anti-Saturn side, as well as during the daytime. The barometric fitting of the N₂ densities obtained from the T37 data gives a very low temperature of 137.0 ± 1.5 K, consistent with plasma-driven models but contradictory to the solar-driven models. However, as emphasized by Müller-Wodarg *et al.* (2008), the interpretation of observed density profiles from any individual flyby deserves caution and may be significantly biased by variations along the spacecraft trajectory. In addition, Titan's thermosphere may not be symmetric about the equator. To summarize, the restricted sampling of the available INMS data does not allow a firm conclusion on the realistic horizontal/diurnal variations to be made at the present time.

CHAPTER 6

DISTRIBUTION OF MOLECULAR HYDROGEN IN TITAN'S EXOSPHERE

In Chapter 5.2.1, I present an analysis of the H_2 distribution in Titan's thermosphere (below the exobase), which reveals that the diffusion model fitting implies a best-fit H_2 flux of $1.3 \times 10^{10} \text{ cm}^{-2} \text{ s}^{-1}$, referred to the surface. In this chapter, I extend the analysis of the H_2 distribution on Titan to regions at altitudes as high as 6,000 km, far above the exobase. The investigation here will rely exclusively on the globally averaged distribution in Titan's exosphere, and possible horizontal/diurnal variations will not be discussed.

In Fig. 6.1, I compare the inbound and outbound H_2 density profiles, determined directly from counts in channel 2 and averaged over all flybys in the sample. Above the exobase, the outbound H_2 densities are systematically higher than the inbound densities, with the deviation increasing at high altitudes. This is an indication of the importance of wall effects, as discussed above in Chapter 5.1, and therefore my analysis in this chapter will only include inbound measurements. In contrast, the wall effects become unimportant in Titan's thermosphere and therefore both inbound and outbound measurements are considered in Chapter 5.2.1.

In Titan's exosphere, the collisions between constituents are so rare that the problem becomes essentially one within the domain of the kinetic theory of free-streaming particles under the influence of Titan's gravity (Fahr & Shizgal 1983). The traditional exospheric model is based on a simple collisionless approach first proposed by Öpik & Singer (1961) and Chamberlain (1963), in an attempt to investigate the structure of the terrestrial exosphere. In such a model, the velocity distribution above the exobase is assumed to be a truncated Maxwellian, and particle densities can be directly calculated by integrating over the appropriate regions of the momentum space. Other choices of the velocity distribution at the exobase have also been investigated, such as the analytic power law and the κ -distribution

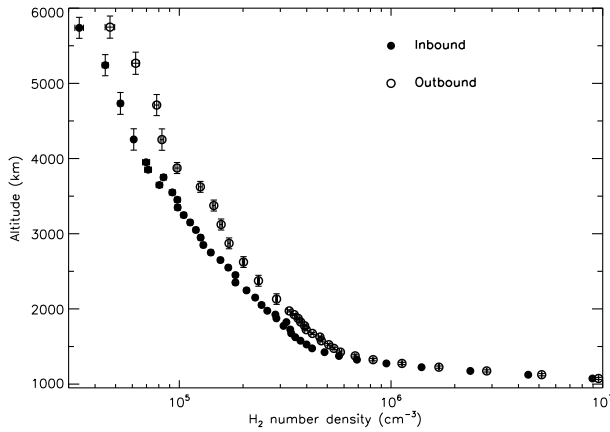


Figure 6.1 The global average H₂ distribution with $\pm 1 \sigma$ uncertainties, in Titan's thermosphere and exosphere, as a function of altitude. The solid circles are for inbound densities, and the open circles for outbound. Comparison between the average inbound and outbound H₂ profiles indicates that the wall effect is important for H₂ above the exobase, but not below. My analysis in this chapter relies exclusively on the inbound data.

(e.g. De La Haye *et al.* 2007).

The escape of H₂ on Titan has been suggested to be mostly thermal and limited by diffusion (Hunten 1973, Bertaux & Kockarts 1983). Conventionally, the thermal escape flux in planetary atmospheres is given by the Jeans formula. However, Yelle *et al.* (2006) observed an escape flux significantly larger than the Jeans value, through an analysis of the H₂ distribution in Titan's thermosphere. The Yelle *et al.* analysis is based on the data acquired during the first close encounter of Cassini with Titan (known in project parlance as TA), and in chapter 5.2.1 I have shown that the analysis here based on a much larger sample generally confirms the Yelle *et al.* result.

Simple one-dimensional modeling is presented in Chapter 6.1, to describe the H₂ distribution at altitudes between 1,500 and 6,000 km. In Chapter 6.2, I describe possible modifications of the simple exospheric model, considering in detail loss processes for H₂ and the energy balance in the transition region between the thermosphere and exosphere. Chapter 6.3 is devoted to understanding the escape of H₂

on Titan, in which I adopt a non-Maxwellian velocity distribution in the 13-moment approximation to calculate the thermal escape flux.

6.1 Preliminary model of H₂ distribution in Titan's exosphere

To model the H₂ distribution above Titan's exobase, I adopt a kinetic approach based on the solution of the collisionless Boltzmann equation (Chamberlain & Hunten 1987). Following the idea originally conceived by Öpik & Singer (1961) and Chamberlain (1963), any particle in the exosphere naturally falls into one of four categories based on orbital characteristics, i.e. ballistic, satellite, escaping, and incoming hyperbolic particles. At any given point in the exosphere, each of the above types occupies an isolated region in the momentum space. Ballistic and escaping particles intersect the exobase, with velocities either smaller or greater than the escape velocity. These two categories represent particles which are directly injected from the thermosphere. On the other hand, satellite particles have perigees above the exobase, and therefore have a purely exospheric origin. Because in any collisionless model, there is no mechanism to establish a steady population of satellite particles, this category is excluded from my calculations. The incoming hyperbolic particles, which obviously require an external origin, are also excluded.

Assuming a Maxwellian velocity distribution function (VDF) at the exobase, Liouville's theorem implies that the VDF for H₂ molecules above this level is also Maxwellian, but truncated to include only regions in the momentum space occupied by either ballistic or escaping particles with trajectories intersecting the exobase. The H₂ densities in the exosphere can be determined by integrating over the Maxwellian VDF within the truncated regions. Analytical results for these integrations can be found in Chamberlain (1963). The model exospheric profile only depends on the density and temperature of H₂ at the exobase, which are treated as two free parameters in the model fitting. The most probable values of these parameters are found to be $n_{\text{exo}} = (4.34 \pm 0.02) \times 10^5 \text{ cm}^{-3}$ and $T_{\text{exo}} = 151.2 \pm 2.2 \text{ K}$, where the exobase is placed at an altitude of 1,500 km. Although the definition of the

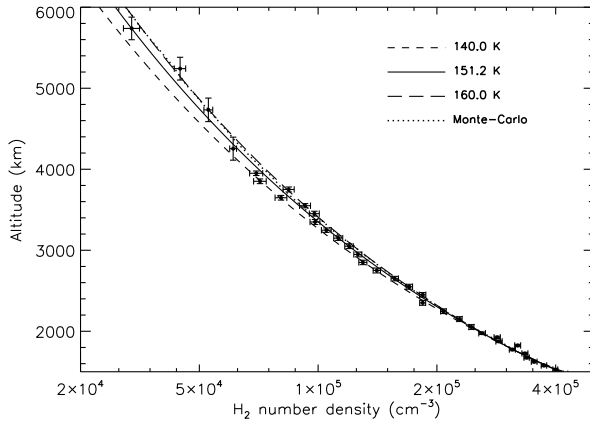


Figure 6.2 The H_2 density profiles calculated with the collisionless model, assuming a truncated Maxwellian VDF for exospheric particles. Different lines correspond to different choices of the exobase temperature, with the solid line representing the most probable value of 151.2 K. The dotted line shows the exospheric H_2 profile calculated from collisionless Monte-Carlo simulations, including Saturn’s gravitational influence. An exobase height of 1,500 km is adopted. The models are overplotted on the INMS measurements averaged over all flybys in the sample.

exobase level is itself subject to uncertainty, the results presented in this section are not sensitive to the exact choice, as a result of the large H_2 scale height ($\sim 1,000$ km near the exobase). However, I will show in Chapter 6.3 that a more realistic exobase height is $\sim 1,600$ km, which has important implication on the derived thermal escape flux.

The exospheric H_2 distribution calculated from such a collisionless model is shown in Fig. 6.2, overplotted on the INMS data. Different profiles correspond to different choices of the exobase temperature, with the solid line representing the most probable value of 151.2 ± 2.2 K, consistent with the N_2 temperature of 154 K within 2σ (see Chapter 5.2.1). The dotted line shows the exospheric H_2 profile calculated from collisionless Monte-Carlo simulations, taking into account Saturn’s gravitational influence (see Chapter 6.3.1 for details).

6.2 Thermal effect and external loss processes of H_2

The previous section shows that the simple collisionless model reasonably describes the observations of H_2 in Titan's exosphere. Here I investigate two physical mechanisms that may potentially modify the exospheric H_2 distribution: (1) the thermal disequilibrium between H_2 and N_2 caused by escape; and (2) the external loss processes of H_2 above Titan's exobase. I will show below that neither of the mechanisms has a substantial influence on the H_2 distribution. However, taking into account the actual thermal structure may have important implications in interpreting the observed H_2 escape, which will be discussed in Chapter 6.3.3.

6.2.1 Temperature decrement for H_2 near Titan's exobase

Early observations of the terrestrial exosphere have shown a significant temperature decrement for atomic H, as large as ~ 100 K near the exobase (Atreya *et al.* 1975). To interpret this, Fahr (1976) has suggested that a correct description of the exospheric model must satisfy energy continuity, in addition to momentum and particle conservation. This condition requires that the energy loss due to particle escape be balanced by an appropriate energy supply through thermal conduction, which is naturally associated with a temperature gradient for the escaping component (Fahr 1976, Fahr & Weidner 1977). For Titan, such a thermal effect implies a temperature difference between the background N_2 gas at T_0 and the diffusing H_2 gas at $T < T_0$. However, this effect should be assessed quantitatively, such that the calculated temperature reduction for H_2 does not contradict the INMS observations. In the previous section, we have already seen that the H_2 gas is approximately in thermal equilibrium with N_2 , as indicated by the closeness of their temperatures near the exobase.

To investigate the thermal effect, I adopt a 13-moment approximation to the kinetic theory, which has been extensively used in modeling the terrestrial polar wind (Lemaire *et al.* 2007, Tam *et al.* 2007). In such an approximation, the

Boltzmann energy transport equation is given by Schunk & Nagy (2000) as

$$\frac{1}{r^2} \frac{d}{dr} (r^2 \Phi_E) = 3k \frac{m}{m_0} n \nu (T_0 - T) - mn \nu \left(\frac{F}{n} \right)^2, \quad (6.1)$$

where $F = F_s(R/r)^2$ is the local H_2 flux with F_s adopted as the most probable value derived from the diffusion equation (R is Titan's radius), m and m_0 are the molecular masses of H_2 and N_2 , T and T_0 are their temperatures of which the latter is fixed as 154 K. The quantity, ν in Eqn. 6.1 is the H_2 - N_2 neutral collision frequency, which is related to the diffusion coefficient, D , in Eqn. 5.3 through $\nu D = kT/m$ (Schunk & Nagy 2000). Φ_E represents the local energy flux, given as

$$\Phi_E = mF(c_p T + \frac{u^2}{2} - \frac{GM}{r}) - \kappa \frac{dT}{dr} - \frac{4}{3} \eta u \left(\frac{du}{dr} - \frac{u}{r} \right), \quad (6.2)$$

where $c_p = (5/2)(k/m) = 1.03 \times 10^8 \text{ ergs K}^{-1} \text{ g}^{-1}$ is the specific heat of H_2 at constant pressure, G is the gravitational constant, M is Titan's mass, $u = F/n$ is the drift velocity of H_2 , κ and η are the thermal conductivity and the viscosity coefficient. I adopt $\kappa = 1.1 \times 10^4 \text{ ergs cm}^{-1} \text{ K}^{-1}$ and $\eta = 5.5 \times 10^{-5} \text{ g cm}^{-1} \text{ s}^{-1}$ for the appropriate temperature (Rowley *et al.* 2003). The first term on the RHS of Eqn. 6.2 corresponds to the intrinsic energy flux of H_2 , with contributions from the internal energy, the bulk kinetic energy and the gravitational energy added together. The other two terms represent the energy transfer through thermal conduction and viscosity. The derivation of Eqn. 6.2 is provided in the appendix. Eqn. 6.1 characterizes the local energy balance for H_2 on Titan. The equation includes the effect of energy transfer from N_2 to H_2 through neutral collisions given by the RHS (the meanings of the two terms will be addressed below). The effects of thermal conduction, viscosity, as well as adiabatic cooling due to H_2 outflow are included in the divergence term on the LHS of Eqn. 6.1.

I solve Eqn. 6.1 for the H_2 thermal structure at altitudes between 1,000 and 2,500 km. Boundary conditions have to be specified to complete the problem, including one for T and one for dT/dr . I assume that the H_2 and N_2 gases are in thermal equilibrium at the lower boundary, i.e. $T = T_0 = 154 \text{ K}$ at 1,000 km. The boundary condition for the temperature gradient is determined by the requirement

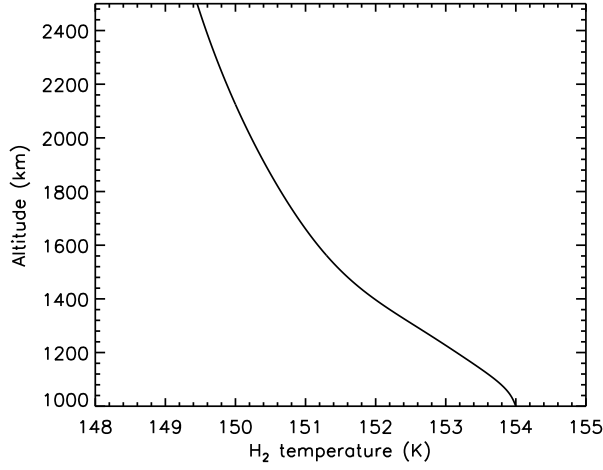


Figure 6.3 The thermal structure for the diffusing H₂ component on Titan, calculated from Eqn. 6.1 and satisfying energy flux continuity at the upper boundary. The model predicts a modest temperature decrement of ~ 2.5 K for H₂ from the lower boundary to the exobase.

of energy continuity at the upper boundary, which can be expressed as

$$\Phi_E = 2\pi \int_{v_{\text{esc}}}^{\infty} v^2 dv \int_0^1 d \cos \theta f(v, \theta) \left(\frac{1}{2} m v^2 - \frac{GMm}{r} \right) v \cos \theta, \quad (6.3)$$

where v_{esc} is the escape velocity at the upper boundary and $f(v, \theta)$ is the VDF for H₂ molecules, which is assumed to be independent of the azimuthal angle but allows for dependence on the polar angle. The simplest scheme is to adopt the drifting Maxwellian distribution. However, the realistic VDF for H₂ molecules at the upper boundary is not strictly Maxwellian. To correct for this, I adopt the VDF for H₂ molecules in the 13-moment approximation. The appropriate form of such a distribution function will be presented in Chapter 6.3. Here, I emphasize that both the drifting Maxwellian and the 13-moment VDF depend on the values of some unknown parameters at the upper boundary (e.g. temperature and drift velocity). This requires that Eqn. 6.1, 6.2 and 6.3 be solved in an iterative manner to ensure self-consistency.

Fig. 6.3 presents the calculated thermal structure for the diffusing H₂ component, which predicts an H₂ temperature of 151.5 K at 1,500 km, or a temperature

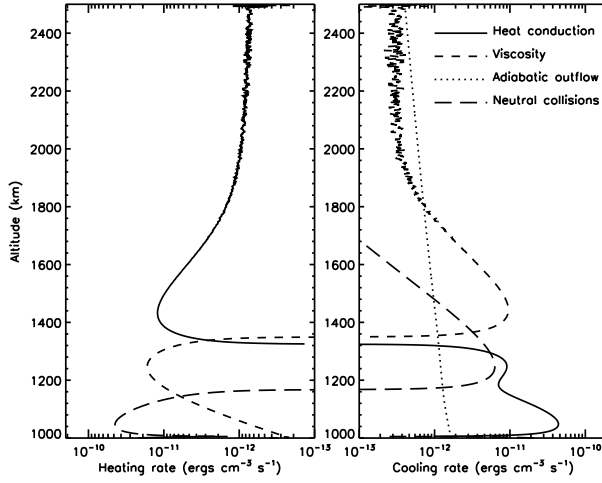


Figure 6.4 The relative magnitudes of various terms in the 13-moment energy equation (Eqn. 6.1). Different lines represent the energy gain/loss rates associated with different mechanisms, including thermal conduction (solid), viscosity (short-dashed), adiabatic outflow (dotted), and $\text{H}_2\text{-N}_2$ neutral collisions (long-dashed).

decrement of 2.5 K. This is consistent with the INMS observations, which give a most probable exobase H_2 temperature of 151.2 K based on the collisionless Chamberlain approach (see Chapter 6.1). However, the predicted thermal effect is too small to get firm supports from the data, since the uncertainties in the temperature determination are considerably larger. A similar calculation in the 13-moment approximation has been carried out by Boqueho & Blelly (2005) on various neutral components in the Martian atmosphere, which shows that the thermal structure of relatively light species such as O present a modest temperature decrement of order 1 K near the exobase (see their Fig. 6.7), comparable to my results.

I show in Fig. 6.4 the relative magnitudes of various terms in Eqn. 6.1 which represent the energy gain/loss rates associated with heat conduction (solid), viscosity (short-dashed), adiabatic outflow (dotted), as well as $\text{H}_2\text{-N}_2$ neutral collisions (long-dashed). Heating and cooling terms are shown in the left panel and right panel, respectively. First, I notice that though the background N_2 gas is warmer than H_2 , neutral collisions between the two components do not necessarily mean 'heating'. The energy transfer through collisions is represented by the RHS of Eqn. 6.1, which

consists of two terms. The first term characterizes the energy transfer due to random motion of the colliding particles, which always acts to heat the H_2 gas. The second term shows that the bulk diffusive motion of H_2 through the stationary N_2 gas is decelerated by their mutual interactions, acting as a cooling mechanism. Whether the net effect of neutral collisions is heating or cooling depends on the relative magnitudes of these two mechanisms. According to my model calculations, the effect of neutral collisions between H_2 and N_2 is heating below $\sim 1,160$ km and cooling above. The effect of thermal conduction can be either heating (above $\sim 1,320$ km) or cooling (below $\sim 1,320$ km), which is always an important energy term in the local energy budget, except near 1,300 km. The effect of viscosity also switches between heating and cooling (at an altitude of $\sim 1,350$ km). Finally, adiabatic outflow is always a cooling mechanism, and is important above $\sim 1,800$ km. Fig. 6.4 shows that well below the exobase, the energy gain through neutral collisions is primarily balanced by energy loss through thermal conduction. However, well above the exobase, the local energy budget is a balance between energy gain through thermal conduction and energy loss through both viscous dissipation and adiabatic outflow. In the transition region between the thermosphere and exosphere, the energy budget is more complicated and an individual energy term may switch between heating and cooling as mentioned above.

The energy budget of H_2 implied in the 13-moment model is more complicated than that described in early works (Fahr 1976, Fahr & Weidner 1977), in which the thermal structure of the diffusing component was obtained by assuming equality between the escaping energy flux, Φ_{esc} and the conductive heat flux. This corresponds to a simplified case of the boundary condition given by Eqn. 6.3, which ignores both the intrinsic and viscous energy fluxes. To examine the relative magnitudes of various energy fluxes, I show in Fig. 6.5 different terms from the RHS of Eqn. 6.2 as a function of altitude. The dotted, short-dashed and long-dashed lines represent the conductive heat flux, the viscous energy flux, and the intrinsic energy flux, respectively. The total energy flux is shown by the thick solid line in Fig. 6.5, along with the condition of energy flux continuity (given by the thin solid line).

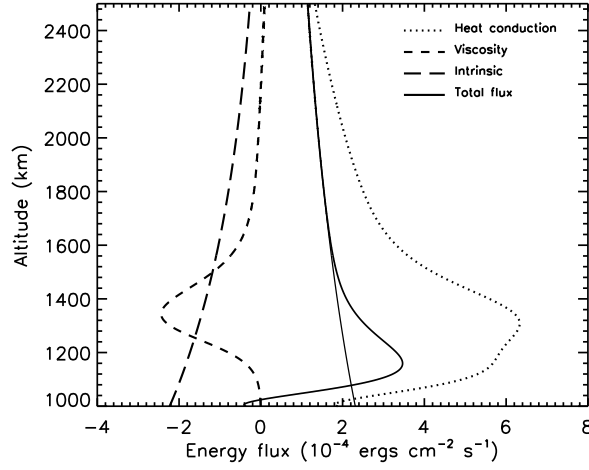


Figure 6.5 The relative magnitudes of various energy fluxes, including the conductive heat flux (dotted), the viscous energy flux (short-dashed), and the intrinsic energy flux (long-dashed) which combines the internal energy, the gravitational energy, as well as the bulk kinetic energy. The total energy flux is given by the thick solid line, which tends to follow the condition of energy flux continuity (given by the thin solid line) above $\sim 1,600$ km.

Above $\sim 1,600$ km, the total energy flux tends to scale as $1/r^2$, implying negligible effects of neutral collisions according to Eqn. 6.1. Correspondingly, the exobase of Titan can be placed at $\sim 1,600$ km based on Fig. 6.5. At this altitude, the total downward energy flux counteracts roughly 50% of the upward conductive heat flux, indicating that the neglect of intrinsic and viscous energy fluxes in the early works is not justified here. The exobase height of $\sim 1,600$ km implied by the variation of total energy flux is higher than the traditional choice of $\sim 1,400$ - $1,500$ km estimated from a comparison between the atmospheric scale height and mean free path. The implication of this result on the thermal escape flux will be discussed in Chapter 6.3.

Finally, I mention that although the thermal effect for H_2 on Titan is not significant, in terms of the absolute value of the temperature decrement, I will show in Chapter 6.3 that the associated heat flux provides an important modification to the velocity distribution of H_2 molecules. In fact, the consequence of the non-

Maxwellian VDF for the escape flux is so large that it may completely invalidate the Jeans formula.

6.2.2 External loss of H₂ in Titan's exosphere

Titan's exosphere is subject to solar EUV radiation, and is, most of the time, within Saturn's magnetosphere. The exospheric distribution of H₂ on Titan may therefore be affected by its interactions with either solar photons or magnetospheric particles through external loss processes. These processes include photoionization and photodissociation, electron impact ionization, as well as charge transfer reactions with energetic protons/ions in the magnetosphere.

Whether a particular loss process appreciably influences the exospheric H₂ distribution relies on a comparison between the corresponding loss timescale and the dynamical time of H₂ molecules spending above the exobase, following their own orbits. To investigate this, I draw a random sample of $\sim 22,000$ particles from the Maxwellian distribution with a temperature of 154 K. The trajectories of these particles, assumed to be injected from Titan's exobase in random upward directions, are calculated and averaged. For ballistic particles, the inferred mean dynamical time increases from 1×10^3 s (on ascending trajectories) and 9×10^3 s (on descending trajectories) at an altitude of 2,000 km, to 7×10^3 s (ascending) and 5×10^4 s (descending) at 6,000 km. The mean dynamical time for escaping particles varies from 5×10^2 s at 2,000 km to 3×10^3 s at 6,000 km. Averaged over all particle types and weighted by their number fractions, the total mean dynamical time is found to be 5×10^3 s at 2,000 km and 2×10^4 s at 6,000 km. Clearly, any external loss process is more efficient at depleting particles on ballistic trajectories, with relatively long dynamical timescales.

Assuming that a particular loss process is characterized by a constant timescale of τ_{loss} , the H₂ density distribution can be calculated by

$$n(r) = n_{\text{exo}} e^{-(\lambda_{\text{exo}} - \lambda)} [\zeta'_{\text{bal}}(\lambda) + \zeta'_{\text{esc}}(\lambda)], \quad (6.4)$$

where $\lambda = (GMm)/(kT_{\text{exo}}r)$ and λ_{exo} is the value at the exobase with $r_{\text{exo}} =$

4075.5 km. For simplicity, I have implicitly assumed a Maxwellian velocity distribution and adopted $T = T_{\text{exo}} = 154$ K at all altitudes above the exobase. Taking into account the non-Maxwellian VDF as well as the actual thermal structure should not alter my results significantly. In Eqn. 6.4, ζ'_{bal} and ζ'_{esc} are the partition functions for ballistic and escaping particles, which take into account the loss processes. Extending the formalism of Chamberlain (1963) to include loss processes, I express the partition functions as

$$\zeta'_{\text{bal}}(\lambda) = \frac{2}{\pi^{1/2}} \left[\int_0^{\xi_1} d\xi \int_0^{\chi_1} d\chi e^{-\xi^2 - \chi - \frac{t(\lambda, \xi, \chi)}{\tau_{\text{loss}}}} + \int_{\xi_1}^{\lambda^{1/2}} d\xi \int_0^{\chi_2} d\chi e^{-\xi^2 - \chi - \frac{t(\lambda, \xi, \chi)}{\tau_{\text{loss}}}} \right], \quad (6.5)$$

$$\zeta'_{\text{esc}}(\lambda) = \frac{1}{\pi^{1/2}} \left[\int_{\xi_1}^{\lambda^{1/2}} d\xi \int_{\chi_2}^{\chi_1} d\chi e^{-\xi^2 - \chi - \frac{t(\lambda, \xi, \chi)}{\tau_{\text{loss}}}} + \int_{\lambda^{1/2}}^{\infty} d\xi \int_0^{\chi_1} d\chi e^{-\xi^2 - \chi - \frac{t(\lambda, \xi, \chi)}{\tau_{\text{loss}}}} \right], \quad (6.6)$$

where $t(\lambda, \xi, \chi)$ is the dynamical time required by a particle to travel from the exobase to a given point in the exosphere, following its own orbit. The integration limits in Eqn. 6.5 and 6.6 are given by $\chi_1 = \lambda^2(\lambda_{\text{exo}} - \lambda + \xi^2)/(\lambda_{\text{exo}}^2 - \lambda^2)$, $\chi_2 = \lambda - \xi^2$, and $\xi_1 = \lambda(1 - \lambda/\lambda_{\text{exo}})$ (Chamberlain & Hunten 1987). The exponential factor of $\exp[-t(\lambda, \xi, \chi)/\tau_{\text{loss}}]$ represents the probability that an H_2 molecule survives the loss process under consideration. $t(\lambda, \xi, \chi)$ can be calculated by

$$t^+(\lambda, \xi, \chi) = \frac{GMm}{kT_{\text{exo}}v_{\text{th}}} \int_{\lambda}^{\lambda_{\text{exo}}} \frac{d\lambda}{\lambda^2(\xi^2 + \lambda)^{1/2}} \quad (6.7)$$

for $\xi > 0$ and

$$t^-(\lambda, \xi, \chi) = 2 \frac{GMm}{kT_{\text{exo}}v_{\text{th}}} \int_{\lambda_{\text{exo}}}^{\lambda_{\text{m}}} \frac{d\lambda}{\lambda^2(\xi^2 + \lambda)^{1/2}} - t^+(\lambda, \xi, \chi) \quad (6.8)$$

for $\xi < 0$, where $v_{\text{th}} = (2kT_{\text{exo}}/m)^{1/2}$ is the thermal velocity of H_2 at the exobase, and λ_{m} corresponds to the maximum radius reached by an H_2 molecule along its orbit (only for ballistic particles). Eqn. 6.7 and 6.8 correspond to the situations in which the H_2 molecule is on the ascending and descending portions of its trajectory, respectively. Escaping particles do not have descending trajectories, and should be excluded from Eqn. 6.8.

I show in Fig. 6.6 the model H_2 profiles calculated from Eqn. 6.4-6.8, overplotted on the INMS measurements. Different lines represent different choices of the

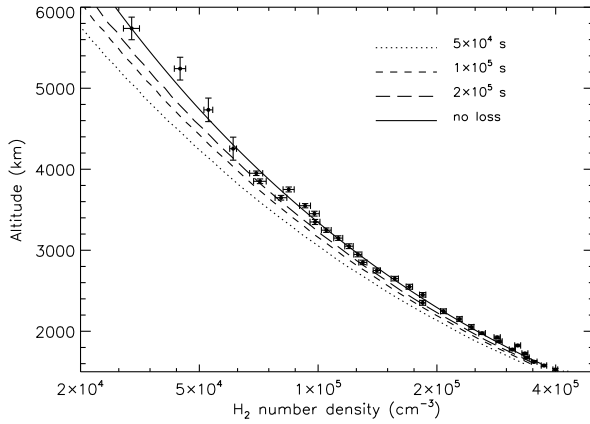


Figure 6.6 The model H_2 density profiles calculated with different values of the constant timescale for H_2 loss, assuming an exobase temperature of 154 K. The models are overplotted on the INMS data for comparison. The solid line corresponds to the case with no external loss mechanism.

constant loss timescale, τ_{loss} , with the solid one giving the reference case with no external H_2 loss. Fig. 6.6 indicates that a loss timescale of order 10^5 s is required to have an appreciable effect on the observed exospheric H_2 distribution. I show below that all reasonable loss processes of H_2 have typical timescales much longer than $\sim 10^5$ s, therefore the exospheric distribution of H_2 molecules cannot be significantly modified by these loss processes.

Photoionization and photodissociation

H_2 molecules are ionized by solar EUV photons with energy above 15.4 eV. Assuming an exosphere that is optically thin to the solar EUV radiation, the photoionization timescale, t_{ion} can be calculated from

$$t_{\text{ion}}^{-1} = \int \pi \tilde{F}_{\odot}(\tilde{\lambda}) \tilde{\sigma}_{\text{ion}}(\tilde{\lambda}) d\tilde{\lambda}, \quad (6.9)$$

where $\tilde{\lambda}$ is the wavelength, $\tilde{\sigma}_{\text{ion}}(\tilde{\lambda})$ is the photoionization cross section of H_2 molecules, and $\pi \tilde{F}_{\odot}(\tilde{\lambda})$ is the solar spectral irradiance. I adopt the analytic formulae for H_2 photoionization cross section from Yan *et al.* (1998), which combines experimental results at low energies and theoretical calculations at high energies.

For the solar EUV irradiance, I adopt the sounding rocket measurements made on Nov. 3, 1994, appropriate for solar minimum conditions during solar cycle 22 (Woods *et al.* 1998). The corresponding F10.7 cm flux is 86 at 1 AU, comparable with the average value of 77 for the INMS sample. With the solar irradiances scaled to the value at Titan, Eqn. 6.9 gives $t_{\text{ion}} = 8.8 \times 10^6$ s.

H₂ molecules are also destroyed through dissociation by solar EUV photons at energies between the Lyman continuum and Ly α . Destruction of H₂ by photodissociation is accomplished through the Solomon process, i.e. upward transitions to electronic excited states followed by spontaneous decays to the vibrational continuum of the ground state (e.g. Abgrall *et al.* 1992). I adopt the parameters for individual transitions in the Lyman and Werner bands published by Abgrall *et al.* (1992), and the spontaneous radiative dissociation rate from Abgrall *et al.* (2000). The photodissociation timescale, t_{dis} can then be expressed as

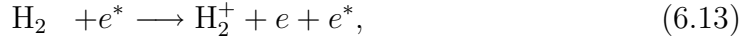
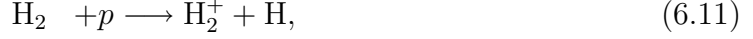
$$t_{\text{dis}}^{-1} = 8.85 \times 10^{-6} \sum_{ij} \pi \tilde{F}_{\odot} (\tilde{\lambda}_{ij}) \tilde{f}_{ij} \tilde{P}_j \tilde{\lambda}_{ij}^2 \text{ s}^{-1}, \quad (6.10)$$

where i and j refer to the lower and upper state of an electronic transition, \tilde{f}_{ij} and $\tilde{\lambda}_{ij}$ are the f -value and central wavelength of the corresponding transition, \tilde{P}_j is the probability that an H₂ molecule at the electronic excited state j spontaneously decays to the vibrational continuum of the ground state. Here $\pi \tilde{F}_{\odot}$ is in units of photons s⁻¹ cm⁻² Å⁻¹, and $\tilde{\lambda}_{ij}$ in units of Å. The summation is over all dipole-allowed transitions in the Lyman and Werner bands. In obtaining Eqn. 6.10, I have also assumed a Doppler line profile, and the integrated results are independent of the adopted exobase temperature. I estimate from Eqn. 6.10 an H₂ photodissociation timescale of $t_{\text{dis}} = 7.2 \times 10^6$ s.

Interactions with Saturn's magnetosphere

Titan has a non-existent or very weak intrinsic magnetic field, and its exosphere is, most of the time, directly subject to bombardment by energetic ions/protons and electrons in Saturn's corotating plasma. Here I investigate the interactions between Titan's exospheric H₂ molecules and Saturn's magnetosphere through the following

processes,



where p is proton and e^* is energetic electron. Rather than integrating over the full energy distribution of the incident fluxes, I approximate the timescale, t_i for each of the above reactions by

$$t_i^{-1} \approx n_i \tilde{\sigma}_i(E_i) \left(\frac{2E_i}{m_i} \right)^{1/2}, \quad (6.14)$$

where i stands for either proton, electron, or singly ionized oxygen, n_i , E_i , and m_i are the density, energy, and particle mass of species i , and $\tilde{\sigma}_i(E_i)$ is the cross section for reaction between i and H_2 at incident energy E_i .

To calculate t_i , I adopt results from the extended plasma model for Saturn, constructed based on the data from Voyager 1 and 2 plasma (PLS) experiments (Richardson & Sittler 1990, Richardson 1995). I use model parameters obtained at $L \approx 20$ to represent plasma conditions close to Titan's orbit around Saturn. For protons, I use $n_p = 0.1 \text{ cm}^{-3}$ and $E_p = 50 \text{ eV}$; for O^+ , I use $n_{\text{O}^+} = 0.13 \text{ cm}^{-3}$ and $E_{\text{O}^+} = 280 \text{ eV}$ (Richardson 1995). The electron energy distribution in Saturn's outer magnetosphere is characterized by a cold thermal component and a hot suprathermal component (Sittler *et al.* 1983). For hot electrons, I use $n_{e,\text{hot}} = 0.019 \text{ cm}^{-3}$ and $E_{e,\text{hot}} = 600 \text{ eV}$ (Richardson 1995). The cold thermal electron component is highly time variable, and the temperature variation is anti-correlated with the density variation (Sittler *et al.* 1983). Here I use values from Voyager 1 inbound measurements made at $L \approx 15$ (Day 317 10:29), with $n_{e,\text{cold}} = 0.4 \text{ cm}^{-3}$ and $E_{e,\text{cold}} = 21 \text{ eV}$ (Sittler *et al.* 1983). The cross sections for reactions 13-15 are adopted as $\tilde{\sigma}_p = 2.0 \times 10^{-16} \text{ cm}^{-2}$ at an incident energy of 48 eV (McClure 1966); $\tilde{\sigma}_{\text{O}^+} = 8.1 \times 10^{-16} \text{ cm}^{-2}$ at 300 eV (Nutt *et al.* 1979); $\tilde{\sigma}_{e,\text{cold}} = 3.3 \times 10^{-17} \text{ cm}^{-2}$ at 21 eV and $\tilde{\sigma}_{e,\text{hot}} = 3.6 \times 10^{-17} \text{ cm}^{-2}$ at 600 eV (Kim *et al.* 1994). With these values, I estimate the characteristic timescales for reactions 13-15 as $t_p \approx 5.1 \times 10^9 \text{ s}$, $t_{\text{O}^+} \approx 1.6 \times 10^9 \text{ s}$, $t_{e,\text{hot}} \approx 1.0 \times 10^9 \text{ s}$, and $t_{e,\text{cold}} \approx 2.8 \times 10^8 \text{ s}$.

Table 6.1 Characteristic timescales of H_2 . The dynamical timescale refers to the mean time required by particles with different orbital characteristics to reach an altitude of 4,000 km, assuming they are injected in random upward directions and satisfy the Maxwellian VDF with a temperature of 154 K.

Process	t_{loss} (s)	Note
Photoionization	9×10^6	solar minimum
Photodissociation	7×10^6	solar minimum
Electron impact ionization	1×10^9	hot electrons
	3×10^8	cold electrons
Charge transfer	5×10^9	$\text{H}_2 + p \longrightarrow \text{H}_2^+ + \text{H}$
	2×10^9	$\text{H}_2 + \text{O}^+ \longrightarrow \text{H}_2^+ + \text{O}$
Dynamical timescale	4×10^3	upward ballistic
	3×10^4	downward ballistic
	2×10^3	escaping

To summarize, I list all the relevant timescales in Table 6.1. Various external loss processes have characteristic timescales between 7×10^6 s and 5×10^9 s, which are much longer than the dynamical time of H_2 molecules above the exobase. This indicates that the exospheric distribution of H_2 on Titan is not significantly modified by these loss processes.

6.3 Escape of H_2 on Titan

I have shown in Chapter 5.2.1 that the H_2 escape flux inferred from the diffusion model is about a factor of 3 higher than the Jeans value, implying an enhanced escape of H_2 on Titan. This flux enhancement could of course suggest that non-thermal processes may play an important role. The non-thermal escape of nitrogen neutrals from this satellite has been extensively studied in previous works. A total loss rate of non-thermal N atoms was estimated to be $< 10^{25} \text{ s}^{-1}$ based on Voyager/UVS observations of airglow emissions (Strobel *et al.* 1992), consistent with the more recent value of $8.3 \times 10^{24} \text{ s}^{-1}$ based on Cassini/INMS observations (De La Haye *et al.* 2007). The production of suprathermal nitrogen neutrals might be contributed by collisional dissociation and dissociative ionization, atmospheric sput-

tering by magnetospheric ions and pickup ions, as well as photochemical processes (e.g. Lammer & Bauer 1993, Cravens *et al.* 1997, Shematovich *et al.* 2001, 2003, Michael *et al.* 2005). Non-thermal escape also dominates over thermal escape for most other planetary atmospheres in the solar system. However, due to the rapid thermal escape of H_2 on Titan, it has long been proposed that non-thermal escape of H_2 is not important for this satellite (Hunten 1973, Bertaux & Kockarts 1983).

6.3.1 Saturn’s gravitational influence

The escape of H_2 on Titan is complicated by the potential influence of Saturn’s gravity. McDonough & Brice (1973) first proposed the possibility that particles escaping from Titan may be captured by Saturn’s strong gravitational field and form into a toroidal cloud near Titan’s orbit (see also Smyth 1981, Hilton & Hunten 1988). Here, I investigate to what extent the escape of H_2 on Titan can be influenced by Saturn’s gravity.

As Saturn’s gravity is taken into account, all H_2 molecules with trajectories reaching above the Hill sphere (roughly at 20 Titan radii) are able to escape from the satellite, since these particles would be progressively perturbed by Saturn’s gravity and eventually end up orbiting with either the planet or the satellite. This implies that the actual H_2 flux at the Hill sphere should include both upward ballistic flow and escaping flow.

To estimate this effect, a Monte-Carlo simulation is performed to numerically integrate the trajectories of test particles in a collisionless exosphere. The test particles start the simulation at the altitude of Titan’s exobase with a velocity vector randomly selected from the upward flux of a Maxwellian distribution with a temperature of 154 K (Brinkmann 1970). The trajectories of the test particles are then integrated forward with an adaptive step-size Bulirsch-Stoer routine according to the equations of motion for the circular restricted three-body problem, with Titan and Saturn treated as the perturbing bodies. The particles are followed until they either return to the exobase or reach the outer boundary of the simulation with a kinetic energy greater than Titan’s gravitational potential. The H_2 density

profile above Titan's exobase calculated from the Monte-Carlo simulation is shown as the dotted line in Fig. 6.2. Its difference with the traditional collisionless model calculated with the same exobase temperature (given by the solid line), is completely due to the inclusion of Saturn's gravitational influence. The H_2 flux is calculated in spherical bins over Titan using the trajectories of one million test particles. I find that Saturn's gravitational influence causes the flux in the simulation to be 23% higher than the Jeans value. This demonstrates that Saturn's gravity is only responsible for a small fraction of the enhanced escape of H_2 on Titan.

6.3.2 Effect of diffusive motion

The conventional way to calculate the thermal escape flux on planetary atmospheres is to use the Jeans formula, which is based on an integration of the Maxwellian distribution for all escaping particles. A preliminary correction to the Jeans flux can be obtained by noting that the non-zero escape flux is naturally associated with the bulk diffusive motion for the escaping component (e.g. Chamberlain & Campbell 1967). Therefore the VDF at Titan's exobase should be taken as a drifting Maxwellian distribution, with the form

$$f_5 = n_{\text{exo}} \left(\frac{m}{2\pi kT} \right)^{3/2} \exp \left(-\frac{m\vec{c}^2}{2kT} \right), \quad (6.15)$$

where $\vec{c} = \vec{v} - \vec{u}$ is the random velocity with \vec{u} being the drift velocity. The subscript '5' is used to emphasize that the drifting Maxwellian is essentially the 5-moment approximation to the full kinetic model, as compared with the 13-moment approximation introduced in Chapter 6.2.1.

I integrate Eqn. 6.15 over all escaping particles at the exobase, with a temperature of 154 K and a bulk velocity of $1.3 \times 10^4 \text{ cm s}^{-1}$ from the diffusion model. This gives an H_2 flux of $6.2 \times 10^9 \text{ cm}^{-2} \text{ s}^{-1}$, more than a factor of 2 smaller than the value derived from the diffusion model. Therefore taking into account the bulk motion does not help to interpret the required flux enhancement.

6.3.3 Non-Maxwellian feature of the velocity distribution function

A useful technique for obtaining approximate expressions for the VDF is to choose the drifting Maxwellian distribution as the 0th order function and expanding the real VDF in a complete orthogonal series (Schunk & Nagy 2000). In the 13-moment approximation, the expansion is truncated to include velocity moments up to the heat flux vector and stress tensor. Such a truncated series expansion has the form

$$\frac{f_{13}}{f_5} = 1 - \frac{m\eta}{kTp} \left(\frac{du}{dr} - \frac{u}{r} \right) \left(c_r^2 - \frac{c^2}{3} \right) + \left(1 - \frac{mc^2}{5kT} \right) \frac{m\kappa}{kTp} \frac{dT}{dr} c_r, \quad (6.16)$$

where p is the partial pressure of H_2 , c_r is the radial component of the random velocity, and other quantities have been defined in Eqn. 6.1, 6.2 and 6.15. The last two terms on the RHS of Eqn. 6.16 represent contributions from viscosity and thermal conduction, respectively.

Thermal escape flux can be obtained by integrating Eqn. 6.16 over all particles with kinetic energy exceeding the gravitational potential. An inherent assumption in this procedure is that the region above the level for performing such an integration is completely collision-free, therefore any particle injected from that level with $v > v_{\text{esc}}$ is able to escape without a further collision to alter its trajectory. The lowest choice of this level can be estimated as $\sim 1,600$ km from the vertical variation of energy flux shown in Fig. 6.5. Here I apply Eqn. 6.16 to a range of altitudes between 1,600 and 2,500 km, with all physical parameters such as temperature and heat flux adopted from the 13-moment calculations in Chapter 6.2.1. The mean thermal escape flux calculated at these levels is $1.1 \times 10^9 \text{ cm}^{-2} \text{ s}^{-1}$ referred to Titan's surface, with a variation of $\sim 20\%$ depending on the exact altitude where the integration over Eqn. 6.16 is performed.

The 13-moment approximation provides a further correction to the thermal escape flux calculated from either the widely-used Jeans formula or the drifting Maxwellian distribution. The H_2 flux calculated in such an approximation is a factor of 2.4 higher than the Jeans value. Considering the minor enhancement due to Saturn's gravity (see Chapter 6.3.1), the large H_2 flux of $1.4 \times 10^{10} \text{ cm}^{-2} \text{ s}^{-1}$ on Titan, as inferred from the diffusion model, could be interpreted by thermal escape

alone, and non-thermal processes are not required.

The correction to the Jeans flux based on the 13-moment approximation comes primarily from the effect of thermal conduction. To investigate the contribution of thermal conduction alone, I run the 13-moment model with the viscosity term ignored in both Eqn. 6.1 and Eqn. 6.16. This gives a similar thermal structure of H_2 and an H_2 escape flux very close to the value obtained in the full 13-moment approximation.

I show in Fig. 6.7 the 13-moment VDF calculated from Eqn. 6.16 (normalized by the drifting Maxwellian), as a function of vertical and horizontal velocities (scaled by either the local thermal velocity or the local escape velocity). The upper panel represents the VDF at the lower boundary of 1,000 km, which shows that the velocity distribution of H_2 molecules is close to Maxwellian, representing a situation with near thermal equilibrium between H_2 and N_2 . With increasing altitude, the deviation from the Maxwellian VDF becomes significant, which is clearly seen in the lower panel of Fig. 6.7, calculated at my upper boundary of 2,500 km. Several features can be identified: (1) Compared with the drifting Maxwellian, the 13-moment VDF presents a depletion of particles with $v < -v_{\text{esc}}$, corresponding to an absence of incoming hyperbolic particles. This is expected for any exospheric model since the collision frequency at such high altitudes is too low to allow a steady population of incoming hyperbolic particles to be established. (2) The 13-moment VDF shows an enhanced population of particles with $v > v_{\text{esc}}$, especially along the radial direction. These particles are expected to carry the conductive heat flux required by the local energy budget.

The implications of the results presented here deserve some further concern. First, I notice that the continuity of escape flux is satisfied exactly in the traditional Jeans formalism, since the upward and downward ballistic flows are in perfect balance, with the integration over escaping particles alone giving the accurate total flux. However, this is not exactly true in the 13-moment approximation. The values of the thermal escape flux derived at different altitudes (between 1,600 km and 2,500 km) but all referred to the surface show some variation at about 20% level, im-

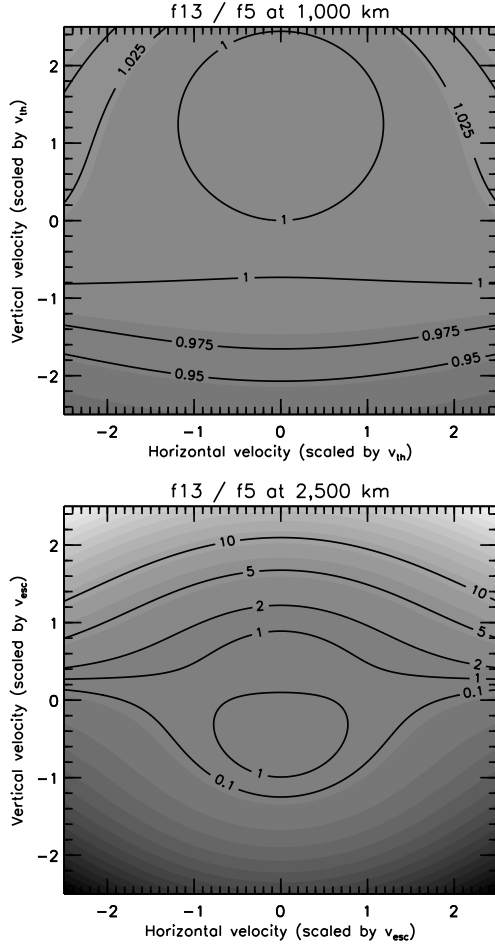


Figure 6.7 The full two-dimensional velocity distribution in the 13-moment approximation (scaled by the drifting Maxwellian), plotted as a function of horizontal and radial velocities (scaled by either the local thermal velocity or the local escape velocity). Several representative contours are drawn. The upper panel and lower panel show the velocity distribution at 1,000 km and 2,500 km, respectively. Departure from Maxwellian is clearly seen at high altitudes.

plying that the continuity of escape flux is not perfectly satisfied. More specifically, the integration over all escaping particles gives an estimate of the thermal escape flux of $\sim 9 \times 10^9 \text{ cm}^{-2} \text{ s}^{-1}$ at 1,600 km and $\sim 1.3 \times 10^{10} \text{ cm}^{-2} \text{ s}^{-1}$ at 2,500 km, where both flux values are referred to the surface. Such a feature of imperfect continuity of escape flux is related to the collisional nature of the 13-moment model, which allows transitions between ballistic and escaping particles in the exosphere in response to rare collisions. In such a model, the perfect balance between upward and downward ballistic flows is clearly not ensured, and the integration over escaping particles gives a representation of the thermal loss rate, rather than an exact physical value.

Second, the traditional exobase level is placed at 1,400-1,500 km for Titan, based on a comparison between the local scale height and mean free path. Here an inherent assumption is that all gas components are stationary. However, the H_2 gas is escaping with a considerable bulk velocity, which contributes to an additional collisional term in the energy equation (the 2nd term on the RHS of Eqn. 6.1). This term, representing the deceleration of bulk motion by molecular diffusion, helps to raise the actual exobase level by several hundreds km. I notice that with this term ignored, the total energy flux shows vanishing divergence at $\sim 1,450$ km, consistent with the traditional choice of the exobase height. The choice of the exobase level has important effects on the derived thermal escape rate. In fact, when integrating Eqn. 6.16 over all escaping particles at an altitude of 1,500 km, I obtain a flux value about 17% higher than the Jeans value. However, the flux calculated at this altitude does not necessarily mean any realistic physical flux, since the effect of neutral collisions is not negligible as I emphasized above. At higher altitudes where collisions can be safely ignored and the procedure of integrating the VDF over all escaping particles is justified, the perturbation of the VDF by thermal conduction becomes strong enough to raise the thermal escape flux significantly above the Jeans value.

Finally, in the traditional collisionless model, calculating the thermal escape flux at altitudes above the exobase relies on the integration of the Maxwellian VDF over a truncated region of the momentum space, to include only escaping particles that intersect the exobase. In fact, it is through this procedure of truncation that

Table 6.2 Thermal escape of H_2 on Titan, where F_s denotes the H_2 escape flux, referred to Titan's surface, and R denotes the H_2 escape rate, equal to the escape flux multiplied by Titan's surface area.

$F_s^{(a)}$ ($\text{cm}^{-2} \text{s}^{-1}$)	$R^{(b)}$ (s^{-1})	Note
1.4×10^{10}	1.2×10^{28}	inferred from data
4.5×10^9	3.8×10^{27}	Jeans escape
5.4×10^9	4.5×10^{27}	Jeans escape including Saturn's gravity
6.2×10^9	5.2×10^{27}	drifting Maxwellian
1.1×10^{10}	9.2×10^{27}	13-moment

the continuity of escape flux in the traditional Jeans formalism is naturally satisfied. However, such a truncation is not necessary in the 13-moment model, since escaping particles reaching any level above the exobase may come from all directions as a result of rare collisions in the exosphere. The 13-moment VDF that smoothly occupies the entire momentum space is a more realistic representation of the actual velocity distribution, as compared with the truncated Maxwellian in the collisionless model.

In a recent work by Strobel (2007), the thermal escape process on Titan was investigated by solving the hydrodynamic equations for a single component N_2 atmosphere, which gave a hydrodynamic escape rate of $4.5 \times 10^{28} \text{amu s}^{-1}$ (the sum of H_2 and CH_4 escape), restricted by power limitations. Assuming that the ratio between individual loss rates is equal to the corresponding limiting flux ratio, Strobel (2007) obtained an H_2 loss rate of $5.3 \times 10^{27} \text{s}^{-1}$, or an H_2 flux of $6.3 \times 10^9 \text{cm}^{-2} \text{s}^{-1}$, referred to Titan's surface. This indicates that by treating the thermal escape process as hydrodynamic rather than stationary (as implicitly assumed in the Jeans formula), the derived H_2 escape rate exceeds the Jeans value by a significant amount, similar to my results obtained from the 13-moment model.

However, the approach followed by Strobel (2007) is quite different from that adopted here, in the sense that he assumed constant composition and worked entirely in the fluid, rather than the kinetic regime. Escape in Strobel's model is

due entirely to bulk outflow of the atmosphere whereas in my calculations escape is driven primarily by the perturbations to the VDF due to the heat flow. The primary effect of bulk outflow is to raise the exobase to a higher level at $\sim 1,600$ km, where the perturbation of the VDF by thermal conduction becomes strong enough to have an appreciable effect on the thermal escape rate. In terms of perturbations to the VDF, the heat flow is more important than the bulk velocity. On the other hand, Strobel (2007) did carefully treat the energy balance in the upper thermosphere and argued that it is the energetics that causes the large loss rates and the breakdown of Jeans escape. In that sense, his results are consistent with those found here, not only quantitatively, but also in terms of the importance of energy continuity to the molecular escape rate. The characters of Strobel's fluid solutions are determined by requiring energy continuity and that the energy escape flux be consistent with the mass escape flux. These requirements coupled with the Navier-Stokes equations imply an escape rate significantly greater than Jeans escape. The same requirement on consistency between mass and energy escape also appears in my calculations, in which the boundary condition on the energy flux forces a negative temperature gradient. The associated heat flux alters the VDF and thereby enhances the escape rate in the kinetic description. It is worth restating that one of the fundamental assumptions in Jeans escape is that the atmospheric energetics is unaffected by escape. In both Strobel's approach and ours, it is the effect of the escape process on the atmospheric energetics that causes the high escape rates and the failure of Jeans escape. What is most surprising is that Jeans escape fails for such small values of the energy flux. An energy flux corresponding to a temperature drop across the transition region of several Kelvin causes more than a factor of 2 increase in the escape flux. It appears important to determine under what conditions the Jeans escape formula can reliably be used.

Finally, I summarize all the relevant fluxes in Table 6.2, in which column 1 gives the thermal escape fluxes calculated in various ways (all referred to Titan's surface), and column 2 the corresponding escape rates. A complete interpretation of the enhanced escape has to rely on a proper consideration of both bulk outflow and

thermal conduction. The former controls the exact level of the exobase, while the latter drives significant departures from the Maxwellian so that the actual thermal escape rate is significantly higher than the Jeans value. In a more general context, enhanced escape induced by bulk outflow and thermal conduction is expected to be a common feature for planetary atmospheres. The 13-moment kinetic model presented in this thesis will be applied to other planetary systems in follow-up studies.

CHAPTER 7

CONCLUDING REMARKS

In this thesis, I present an in-depth study of the neutral gas distribution in Titan's thermosphere above 950 km, combining the INMS data in the CSN mode acquired during 15 Titan flybys. The sample adopted in this work preferentially selects measurements made over Titan's northern hemisphere, toward the facing-Saturn side, and exclusively at solar minimum conditions.

Corrections and calibrations for various instrumental effects are performed carefully, including correction for possible saturation in the high gain counter, calibration between the FU and REU sensitivities, subtraction of background counts as well as counts from residual gases in the INMS antechamber, correction for thruster firing contamination in channel 2, as well as correction for ram pressure enhancement. Since there is no robust way to correct for crosstalk near channel 28, counts in channel 27 are ignored in our analysis, and as a consequence, it is difficult to constrain the abundances of HCN in the ambient atmosphere.

Determination of the densities of neutral constituents in Titan's upper atmosphere is complicated by the fact that the counts in a particular mass channel are likely to be contributed by more than one species. In order to untangle these overlapping cracking patterns between different species, I adopt the technique of Singular Value Decomposition (SVD) which constrains the densities of all species simultaneously (Press *et al.* 1992). Various tricks are adopted in the SVD analysis to minimize the coupling between different species, the number of free parameters in the fit, as well as uncertainties of the derived densities. These include (1) calculating the densities of N_2 and $^{14}\text{N}^{15}\text{N}$ directly from counts in channels 14, 28 and 29, which are then used to fix the densities of $^{15}\text{N}^{15}\text{N}$ according to the observed nitrogen isotope ratios; (2) treating the combination of C_2H_2 and C_2H_4 as an *imaginary* species, in the form of $\frac{3}{4}n(\text{C}_2\text{H}_2) + \frac{1}{4}n(\text{C}_2\text{H}_4)$; (3) determining the $^{13}\text{CH}_4$ densities

from the presumed carbon isotope ratio, taking into account diffusion separation as well as escape; and (4) adopting a scheme in which whether a given species is included in the SVD fit depends on its signal-to-noise ratio in one of its main channels. An additional mathematical difficulty inherent in the SVD decomposition is that occasionally the best-fit densities of some species are negative. To avoid this, I adjust the solution by adding a linear combination of the column vectors associated with the two smallest singular values, and the final solution is identified with the minimum χ^2 value in the parameter space where densities of all species are positive.

With the procedures described above, I divide the whole sample into 114 individual mass spectra, obtained by averaging over different altitude bins for any given flyby. Inbound and outbound measurements are treated separately. Error analysis shows that for relatively abundant species such as CH_4 , H_2 and $\text{C}_2\text{H}_2/\text{C}_2\text{H}_4$, uncertainties due to sensitivity calibration are the dominant sources of error, whereas for most minor species, those due to counting statistics are more important.

For most neutral species in Titan's upper atmosphere, the density measurements show clear asymmetry about C/A, in the sense that density enhancement is always observed during the outbound legs. This can be interpreted as a result of wall effects, which can be either adsorption/desorption of incoming molecules or heterogeneous surface chemistry on the chamber walls. The wall effect has also been used to argue for the detection of NH_3 based on the INMS data. I propose a simple model to describe the processes of adsorption/desorption, assuming a constant adsorption probability and a desorption time constant inversely proportional to the N_2 density in the INMS chamber. Such a model provides a reasonable description of the observed chamber densities (as a function of time from C/A) for several heavy species, and suggests that both the inbound and outbound measurements tend to underestimate the true atmospheric abundances by as large as an order of magnitude, when taking into account ram pressure enhancement alone. However, in most cases, possible values of the adsorption probability and desorption time constant are not well constrained, leading to relatively large uncertainties of the true atmospheric abundances implied by the model. For several species, including C_6H_6 , C_7H_8 , NH_3

and C_2N_2 , the simple model of adsorption/desorption may not be valid since heterogeneous surface chemistry on the chamber walls might be of more importance, due to the relatively high abundances of the associated radicals in the ambient atmosphere (Vuitton *et al.* 2008). For N_2 , CH_4 , H_2 and ^{40}Ar , the wall effects are negligible, since the average inbound and outbound profiles are nearly identical. I use both the inbound and outbound data in our analysis of the distribution of N_2 , CH_4 , H_2 and ^{40}Ar (as well as their isotopes) in Titan's upper atmosphere. For other minor species, I present both their abundances directly obtained from the inbound measurements adopting the 'ideal' ram enhancement factor (see Table 4), and their abundances corrected for wall adsorption/desorption (see Table 5).

I perform an analysis of the globally averaged density distribution of N_2 , CH_4 and H_2 in Titan's upper atmosphere between 950 and 1,500 km. An eddy profile given by Yelle *et al.* (2008) is adopted in the diffusion model fitting. The barometric model fitting of the N_2 profile gives a best-fit thermospheric temperature of 154.0 ± 1.5 K, consistent with previous determination (Vervack *et al.* 2004, Yelle *et al.* 2006, Cui *et al.* 2008). The average CH_4 and H_2 profiles are each described by the diffusion model, which constrains their most probable fluxes as $(3.04^{+0.06}_{-0.10}) \times 10^9 \text{ cm}^{-2} \text{ s}^{-1}$ and $(1.29 \pm 0.01) \times 10^{10} \text{ cm}^{-2} \text{ s}^{-1}$, referred to Titan's surface. I fit the observed $^{14}\text{N}^{15}\text{N}$ distribution with a diffusion equilibrium model throughout Titan's atmosphere from the surface to the exobase. The best-fit nitrogen isotope ratio at the surface is estimated to be 131.6 ± 0.2 , about half the terrestrial value. This is nearly 30% lower than the Huygens/GCMS result of 183 ± 5 (Niemann *et al.* 2005). The carbon isotope ratio at 1,100-1,200 km is estimated to be 93.3 ± 0.1 from the counts in channel 17 obtained during the inbound legs, ignoring the contribution from NH_3 . Combining the GCMS value of 82.3 ± 1 , I fit the observations of carbon isotope ratio with a diffusion model allowing for escape. The drift velocity ratio of CH_4 and $^{13}\text{CH}_4$ at the exobase is treated as a free parameter. Considering the uncertainties in the adopted molecular diffusion coefficients, the model fitting suggests that both CH_4 and $^{13}\text{CH}_4$ molecules escape from Titan's exobase at roughly the same speed, in contrast to the Jeans case which requires that $^{13}\text{CH}_4$ escapes with a speed only

18% of the CH_4 value.

Among all the other minor species included in our spectral analysis, I have firm detections of C_2H_2 , C_2H_4 , C_2H_6 , $\text{CH}_3\text{C}_2\text{H}$, C_4H_2 , C_6H_6 , HC_3N , C_2N_2 and NH_3 , especially below 1,050 km. However, the detection of NH_3 in Titan's upper atmosphere deserves some caution, since a significant fraction of the observed NH_3 molecules might be those formed on the chamber walls from N and H radicals in the ambient atmosphere. Upper limits are put for C_3H_8 , C_4H_6 , C_7H_8 , CH_3CN , $\text{C}_2\text{H}_3\text{CN}$, H_2O and CO_2 , in a global average sense. The abundances of heavy hydrocarbons and nitriles derived directly from the inbound data are systematically higher than the values predicted from the ion-neutral chemistry model with ion densities obtained from the INMS data in the OSI mode (Vuitton *et al.* 2007). However, with reasonable corrections for wall adsorption/desorption, both works reach consistent results.

The INMS data also show some signature of horizontal/diurnal variations of temperature and neutral gas distribution in Titan's thermosphere, which can be summarized as follows: (1) The equatorial regions appear to be warmer, and present some evidences for the depletion of light species such as CH_4 as well as accumulation of all heavy species except for ^{40}Ar . The effect of atmospheric oblateness, as suggested by Müller-Wodarg *et al.* (2008), may not be strong enough to counteract the observed meridional variations. The meridional variation of H_2 shows a more complex pattern, with enhanced mixing ratios present at mid latitudes. (2) The magnetospheric ramside and facing-Saturn side of Titan appear to be warmer, accompanied with CH_4 depletion. The zonal variation of H_2 seems to present a different pattern. No reliable zonal variation of heavy species can be concluded. (3) Titan's nightside hemisphere appears to be warmer than the dayside, and shows depletion of light species including both CH_4 and H_2 . No diurnal variation is observed for heavy species.

While some of the above variations might be interpreted by either the solar-driven models or plasma-driven models, a physical scenario that reconciles all the observed horizontal/diurnal variations in a consistent way is not easy, which re-

quires a careful evaluation of the effect of restricted sampling. Especially, I notice that the available INMS measurements made near the north polar regions also preferentially select Titan's wakeside and anti-Saturn side, as well as Titan's dayside hemisphere. This implies that from a pure observational point of view, it is not likely to distinguish between a cooler north pole, a cooler wakeside or anti-Saturn side, and a cooler dayside. The meridional variations of thermospheric temperature and CH₄ distribution reported by Müller-Wodarg *et al.* (2008) are confirmed by this study based on different methods, though the present INMS sample may not be able to tell whether this is a real physical feature or biased observation due to selective sampling. However, the conclusion that Titan has a warmer ramside along with some evidence for CH₄ depletion is likely to be real. Such a feature suggests that precipitation of energetic ions/electrons from Saturn's corotating plasma may deposit significant energy into Titan's upper atmosphere, raising the local temperature, driving horizontal winds, and causing redistribution of neutral gas. The observed horizontal (both meridional and zonal) variations of H₂ present a further complication, in which the effects of rapid thermal escape and large ballistic flow in the exosphere may also be important.

The H₂ flux is higher than the Jeans value by a factor of ~ 3 . To interpret this, I adopt a kinetic model in which the orthogonal series expansion in the 13-moment approximation defines a non-Maxwellian VDF that includes the effects of both thermal conduction and viscosity. Integrating over such a VDF for all escaping particles at a range of altitudes above the exobase gives a mean H₂ flux of $1.1 \times 10^{10} \text{ cm}^{-2} \text{ s}^{-1}$ referred to the surface, with an uncertainty of $\sim 20\%$ associated with the exact altitude level (between 1,600 and 2,500 km) where the integration is performed. Below 1,600 km, the effect of collisions between H₂ and N₂ cannot be ignored, and the integration of the VDF over all escaping particles to estimate the thermal escape flux is not justified. The escape flux implied by the 13-moment model is significantly higher than the Jeans value and roughly matches the flux inferred from the diffusion equation. The 13-moment model interprets the enhanced escape as a result of the accumulation of H₂ molecules on the high energy portion

of the VDF, primarily associated with the conductive heat flux. In this work, the enhanced escape of H_2 on Titan is still thermal in nature. Non-thermal processes are not required to interpret the loss of H_2 on Titan. In contrast, the Jean flux of CH_4 on Titan is tiny, and the interpretation of CH_4 escape (with a flux of $3 \times 10^9 \text{ cm}^{-2} \text{ s}^{-1}$ referred to the surface) still requires non-thermal mechanisms (De La Haye *et al.* 2007a, b, Yelle *et al.* 2008).

APPENDIX A

Energy density and flux in the 13-moment approximation

In the 13-moment approximation, the continuity, momentum and energy equations for a diffusing neutral component can be expressed as

$$\frac{\partial n}{\partial t} + \frac{\partial}{\partial x_i}(nu_i) = 0, \quad (\text{A.1})$$

$$mn\left(\frac{\partial u_i}{\partial t} + u_j \frac{\partial u_i}{\partial x_j}\right) + \frac{\partial p}{\partial x_i} + \frac{\partial \tau_{ji}}{\partial x_j} - mng_i = \frac{\delta M_i}{\delta t}, \quad (\text{A.2})$$

$$\frac{3}{2} \frac{\partial p}{\partial t} + \frac{3}{2} u_i \frac{\partial p}{\partial x_i} + \frac{5}{2} p \frac{\partial u_i}{\partial x_i} + \frac{\partial q_i}{\partial x_i} + \tau_{ij} \frac{\partial u_i}{\partial x_j} = \frac{\delta E}{\delta t}, \quad (\text{A.3})$$

where n , p , u_i , q_i , τ_{ij} are the density, pressure, drift velocity vector, heat flux vector and stress tensor of the neutral species, with $i, j = 1, 2, 3$ characterizing components along the three orthogonal spatial coordinates (x_i), and $\delta M_i/\delta t$ and $\delta E/\delta t$ are the momentum and energy integrals (Schunk & Nagy 2000). Here, for repeated indices, the Einstein summation convention is assumed. Eqn. A3 can be recast as

$$\frac{3}{2} \frac{\partial p}{\partial t} + \frac{5}{2} \frac{\partial}{\partial x_i}(pu_i) - u_i \frac{\partial p}{\partial x_i} + \frac{\partial q_i}{\partial x_i} + \tau_{ij} \frac{\partial u_i}{\partial x_j} = \frac{\delta E}{\delta t}. \quad (\text{A.4})$$

Using Eqn. A2 to eliminate $u_i \partial p / \partial x_i$, we get

$$\begin{aligned} \frac{3}{2} \frac{\partial p}{\partial t} + \frac{5}{2} \frac{\partial}{\partial x_i}(pu_i) + mn \frac{\partial}{\partial t} \left(\frac{1}{2} u^2 \right) + mnu_i u_j \frac{\partial u_i}{\partial x_j} + u_i \frac{\partial \tau_{ji}}{\partial x_j} \\ - mnu_i g_i + \frac{\partial q_i}{\partial x_i} + \tau_{ij} \frac{\partial u_i}{\partial x_j} = \frac{\delta E}{\delta t} + u_i \frac{\delta M_i}{\delta t}, \end{aligned} \quad (\text{A.5})$$

where $u^2 = u_i u_i$. The gravity term in Eqn. A5 can be expressed as

$$\begin{aligned} -mnu_i g_i &= -mnu_i \frac{\partial}{\partial x_i} \left(\frac{GM}{r} \right) \\ &= -\frac{\partial}{\partial x_i} \left(\frac{GMm}{r} nu_i \right) + \frac{GMm}{r} \frac{\partial}{\partial x_i} (nu_i) \\ &= -\frac{\partial}{\partial x_i} \left(\frac{GMm}{r} nu_i \right) - \frac{GMm}{r} \frac{\partial n}{\partial t}, \end{aligned} \quad (\text{A.6})$$

where $r = (x_i x_i)^{1/2}$, M is the planet mass, G is the gravitational constant, and we have used Eqn. A1 to eliminate $\partial(nu_i)/\partial x_i$ in the last equality. The term, $mn u_i u_j (\partial u_i / \partial x_j)$ in Eqn. A5 can be recast as

$$mn u_i u_j \frac{\partial u_i}{\partial x_j} = \frac{\partial}{\partial x_j} (mn u^2 u_j) - u^2 \frac{\partial}{\partial x_j} (mn u_j) - mn u_i u_j \frac{\partial u_i}{\partial x_j}, \quad (\text{A.7})$$

which gives

$$\begin{aligned} mn u_i u_j \frac{\partial u_i}{\partial x_j} &= \frac{\partial}{\partial x_j} \left(\frac{1}{2} mn u^2 u_j \right) - \frac{1}{2} u^2 \frac{\partial}{\partial x_j} (mn u_j) \\ &= \frac{\partial}{\partial x_j} \left(\frac{1}{2} mn u^2 u_j \right) + \frac{1}{2} m u^2 \frac{\partial n}{\partial t}. \end{aligned} \quad (\text{A.8})$$

Finally, we write $u_i (\partial \tau_{ji} / \partial x_j)$ as

$$u_i \frac{\partial \tau_{ji}}{\partial x_j} = \frac{\partial}{\partial x_j} (u_i \tau_{ji}) - \tau_{ji} \frac{\partial u_i}{\partial x_j}. \quad (\text{A.9})$$

Using Eqn. A6, A8 and A9, Eqn. A5 can be expressed as

$$\begin{aligned} \frac{\delta E}{\delta t} + u_i \frac{\delta M_i}{\delta t} &= \frac{\partial}{\partial t} \left(\frac{3}{2} p + \frac{1}{2} mn u^2 - \frac{GMm}{r} n \right) \\ &+ \frac{\partial}{\partial x_j} \left(\frac{5}{2} p u_j + \frac{1}{2} mn u^2 u_j + u_i \tau_{ji} - \frac{GMm}{r} n u_j + q_j \right), \end{aligned} \quad (\text{A.10})$$

where we have used the fact that τ_{ij} is symmetric.

We further recast Eqn. A10 as

$$\frac{\partial \epsilon}{\partial t} + \frac{\partial}{\partial x_j} (\phi_j + u_i \tau_{ji} + q_j) = \frac{\delta E}{\delta t} + u_i \frac{\delta M_i}{\delta t}. \quad (\text{A.11})$$

Clearly, ϵ and ϕ_j represent the energy density and energy flux, with the definitions of

$$\epsilon = mn \left(c_v T + \frac{1}{2} u^2 - \frac{GM}{r} \right), \quad (\text{A.12})$$

$$\phi_j = mn u_j \left(c_p T + \frac{1}{2} u^2 - \frac{GM}{r} \right), \quad (\text{A.13})$$

where we have replaced p by nkT with k being the Boltzmann constant and T being the gas temperature, $c_v = (3/2)(k/m)$ and $c_p = (5/2)(k/m)$ are the specific heat

capacities at constant volume and pressure. The terms, $u_i\tau_{ji}$ and q_j in Eqn. A11 represent energy fluxes associated with viscous dissipation and thermal conduction, respectively. Assuming spherical symmetry, we can express the radial components of these energy fluxes as

$$(q_i)_r = -\kappa \frac{dT}{dr}, \quad (\text{A.14})$$

$$(u_i\tau_{ji})_r = -\frac{4}{3}\eta u \left(\frac{du}{dr} - \frac{u}{r} \right), \quad (\text{A.15})$$

where κ is the thermal conductivity and η the viscosity coefficient.

REFERENCES

- [1] Abgrall, H., Le Bourlot, J., Pineau Des Forets, G., Roueff, E., Flower, D. R., & Heck, L., 1992. Photodissociation of H_2 and the H/H_2 transition in interstellar clouds, *Astro. Astrophys.*, 253, 525.
- [2] Abgrall, H., Roueff, E., & Drira, I., 2000. Total transition probability and spontaneous radiative dissociation of B, C, B' and D states of molecular hydrogen, *Astro. Astrophys. Suppl.*, 141, 297.
- [3] Atreya, S. K., Hays, P. B., & Nagy, A. F., 1975. Doppler profile measurements of the geocoronal hydrogen Balmer alpha line, *J. Geophys. Res.*, 80, 635.
- [4] Atreya, S. K., Adams, E. Y., Niemann, H. B., Demick-Montelara, J. E., Owen, T. C., Fulchignoni, M., Ferri, F., & Wilson, E. H., 2006. Titan's methane cycle, *Planet. Space Sci.*, 54, 1177, doi:10.1016/j.pss.2006.05.028.
- [5] Banks, P. M., & Kockarts, G., 1973. *Aeronomy*, Academic, San Diego, Calif.
- [6] Banaszkiewicz, M., Lara, L. M., Rodrigo, R., Lòpez-Moreno, J. J., & Molina-Cuberos, G. J., 2000. A coupled model of Titan's atmosphere and ionosphere, *Icarus*, 147, 386, doi:10.1006/icar.2000.6448.
- [6] Bertaux, J. L., & Kockarts, G., 1983. Distribution of molecular hydrogen in the atmosphere of Titan, *J. Geophys. Res.*, 88, 8716.
- [7] Bernard, J. -M., Coll, P., Coustenis, A., & Raulin, F., 2003. Experimental simulation of Titans atmosphere: Detection of ammonia and ethylene oxide, *Planet. Space Sci.*, 51, 1003, doi:10.1016/S0032-0633(03)00131-4.
- [8] Bézard, B., Coustenis, A., & McKay, C. P., 1995. Titans stratospheric temperature asymmetry: A radiative origin? *Icarus*, 113, 267, doi:10.1006/icar.1995.1023.
- [9] Bird, M. K., Dutta-Roy, R., Asmar, S. W., & Rebold, T. A., 1997. Detection of Titan's Ionosphere from Voyager 1 Radio Occultation Observations, *Icarus*, 130, 426, doi:10.1006/icar.1997.5831.
- [10] Brecht, S. H., Luhmann, J. G., & Larson, D. J., 2000. Simulation of the Saturnian magnetospheric interaction with Titan, *J. Geophys. Res.*, 105, 13119, doi:10.1029/1999JA900490
- [11] Brinkmann, R. T., 1970. Departures from Jeans' escape rate for H and He in the Earth's atmosphere, *Planet. Space Sci.*, 18, 449.

- [12] Broadfoot, A. L., Sandel, B. R., Shemansky, D. E., Holberg, J. B., Smith, G. R., Strobel, D. F., McConnell, J. C., Kumar, S., Hunten, D. M., Atreya, S. K., Donahue, T. M., Moos, H. W., Bertaux, J. L., Blamont, J. E., Pomphrey, R. B., & Linick, S., 1981. Extreme ultraviolet observations from Voyager 1 encounter with Saturn, *Science*, 212, 206.
- [13] Chamberlain, J. W., 1963. Planetary coronae and atmospheric evaporation, *Planet. Space Sci.*, 11, 901.
- [14] Chamberlain, J. W., & Campbell, F. J., 1967. Rate of evaporation of a non-Maxwellian atmosphere, *Astrophys. J.*, 149, 687.
- [15] Chamberlain, J.W., & Hunten, D.M., 1987. Theory of planetary atmospheres: an introduction to their physics and chemistry. In: Donn, W.L. (Eds.), *Internat. Geophys. Ser.* 36, Academic Press, San Diego, CA.
- [16] Chapman, S., & Cowling, T. G., 1970. The mathematical theory of non-uniform gases, 3rd ed., Cambridge Univ. Press, Cambridge, UK.
- [17] Coates, A. J., Crary, F. J., Lewis, G. R., Young, D. T., Waite, J. H., & Sittler, E. C., 2007. Discovery of heavy negative ions in Titan's ionosphere, *Geophys. Res. Lett.*, 34, L24S05, doi:10.1029/2007GL030919.
- [18] Coustenis, A., Bézard, B., & Gautier, D., 1989. Titan's atmosphere from Voyager infrared observations: I. The gas composition of Titan's equatorial region, *Icarus*, 80, 54, doi:10.1016/0019-1035(89)90161-9.
- [19] Coustenis, A., Bézard, B., & Gautier, D., 1989. Titans atmosphere from Voyager Infrared Observations: II. The CH₃D abundance and D/H ratio from the 9001200 cm⁻¹ spectral region, *Icarus*, 82, 67, doi:10.1016/0019-1035(89)90024-9.
- [20] Coustenis, A., Salama, A., Schulz, B., Ott, S., Lellouch, E., Encrenaz, T. H., Gautier, D., & Feuchtgruber, H., 2003. Titan's atmosphere from ISO mid-infrared spectroscopy, *Icarus*, 161, 383, doi:10.1016/S0019-1035(02)00028-3.
- [21] Coustenis, A., Achterberg, R. K., Conrath, B. J., Jennings, D. E., Marten, A., Gautier, D., Nixon, C. A., Flasar, F. M., Teanby, N. A., Bézard, B., Samuelson, R. E., Carlson, R. C., Lellouch, E., Bjoraker, G. L., Romani, P. N., Taylor, F. W., Irwin, P. G., Fouchet, T., Hubert, A., Orton, G. S., Kunde, V. G., Vinatier, S., Mondellini, J., Abbas, M. M., & Courtin, R., 2007. The composition of Titans stratosphere from Cassini/CIRS mid-infrared spectra, *Icarus*, 189, 35, doi:10.1016/j.icarus.2006.12.022.
- [22] Cui, J., Yelle, R. V., & Volk, K., 2008. The distribution and escape of molecular hydrogen in Titan's thermosphere and exosphere, *J. Geophys. Res.*, submitted.

- [23] Cravens, T. E., Keller, C. N., & Ray, B., 1997. Photochemical sources of non-thermal neutrals for the exosphere of Titan, *Planet. Space Sci.*, 45, 889, doi:10.1016/S0032-0633(97)00064-0.
- [24] Cravens, T. E., Robertson, I. P., Waite, J. H., Jr., Yelle, R. V., Kasprzak, W. T., Keller, C. N., Ledvina, S. A., Niemann, H. B., Luhmann, J. G., McNutt, R. L., Ip, W.-H., De La Haye, V., Müller-Wodarg, I. C. F., Wahlund, J.-E., Anicich, V. G., & Vuitton, V., 2006. Composition of Titan's ionosphere, *Geophys. Res. Lett.*, 33, L07105, doi:10.1029/2005GL025575.
- [25] De La Haye, V., Waite, J. H., Jr., Johnson, R. E., Yelle, R. V., Cravens, T. E., Luhmann, J. G., Kasprzak, W. T., Gell, D. A., Magee, B., Leblanc, F., Michael, M., Jurac, S., & Robertson, I. P., 2007a. Cassini INMS data in Titan's upper atmosphere and exosphere: observation of a suprathermal corona, *J. Geophys. Res.*, 112, A07309, doi:10.1029/2006JA012222.
- [26] De La Haye, V., Waite, J. H., Jr., Cravens, T. E., Nagy, A. F., Johnson, R. E., Lebonnois, S., & Robertson, I. P., 2007b. Titan's corona: The contribution of exothermic chemistry, *Icarus*, 191, 236, doi:10.1016/j.icarus.2007.04.031.
- [27] Fahr, H. J., 1976. Reduced hydrogen temperatures in the transition region between thermosphere and exosphere, *Ann. Geophys.*, 32, 277.
- [28] Fahr, H. J., & Weidner, B., 1977. Gas evaporation from collision-determined planetary exospheres, *MNRAS*, 180, 593.
- [29] Fahr, H. J., & Shizgal, B., 1983. Modern exospheric theories and their observational relevance, *Rev. Geophys. and Space Phys.*, 21, 75.
- [30] Feigelson, E. D., & Nelson, P. I., 1985. Statistical methods for astronomical data with upper limits: I. Univariate distributions, *Astrophys. J.*, 293, 192, doi:10.1086/163225.
- [31] Fox, J. L., & Yelle, R. V., 1997. Hydrocarbon ions in the ionosphere of Titan, *Geophys. Res. Lett.*, 24, 2179.
- [32] Hanley, H. J. M., Sengers, J. V., & Ely, J. F., 1976. 14th Int. Conf. on Thermal Conductivity (Storrs, Conn., June 1975), Klemens, P.G., & Chu, T.K., Eds. (Plenum Press N.Y., 1976), p. 383.
- [33] Gan, L., Keller, C. N., & Cravens, T. E., 1992. Electrons in the ionosphere of Titan, *J. Geophys. Res.*, 97, 12137.
- [34] Hilton, D. A., & Hunten, D. M., 1988. A partially collisional model of the Titan hydrogen torus, *Icarus*, 73, 248.

- [35] Hörst, S. M., Vuitton, V., & Yelle, R. V., 2008. The origin of oxygen species in Titan's atmosphere, *J. Geophys. Res.*, submitted.
- [36] Hunten, D. M., 1972. The atmosphere of Titan, *Comments Astrophys. Space Phys.* 4, 149.
- [37] Hunten, D. M., 1973. The escape of H_2 from Titan, *J. Atmos. Sci.*, 30, 726.
- [38] Ip, W. -H., 1990. Titan's upper ionosphere. *Astrophys. J.*, 362, 354, doi:10.1086/169271.
- [39] Kim, Y. K., & Rudd, M. E., 1994. Binary-encounter-dipole model for electron-impact ionization, *Phys. Rev. A*, 50, 3954.
- [40] Lammer, H., & Bauer, S. J., 1993. Atmospheric mass loss from Titan by sputtering, *Planet. Space Sci.*, 41, 657.
- [41] Lebonnois, S., Bakes, E. L. O., & McKay, C. P., 2003. Atomic and molecular hydrogen budget in Titan's atmosphere, *Icarus*, 161, 474.
- [42] Ledvina, S. A., Cravens, T. E., Salman, A., & Kecskemety, K., 2000. Ion trajectories in Saturn's magnetosphere near Titan, *Adv. Space Res.*, 26, 1691, doi:10.1016/S0273-1177(00)00075-2.
- [43] Lemaire, J. F., Peterson, W. K., Chang, T., Schunk, R. W., Barakat, A. R., Denars, H. G., & Khazanov, 2007. History of kinetic polar wind models and early observations, *J. Atmos. Solar-Terrestrial Phys.*, 69, 1,901.
- [44] Luhmann, J. G., 1996. Titan's ion exosphere wake: A natural ion mass spectrometer? *J. Geophys. Res.*, 101, 29387, doi: 10.1029/96JE03307.
- [45] Johnson, R. E., 1994. Plasma-induced sputtering of an atmosphere, *Space Sci. Rev.*, 69, 215, doi:10.1007/BF02101697.
- [46] Kasprzak, W. T., Hedin, A. E., Niemann, H. B., & Spencer, N. W., 1980. Atomic nitrogen in the upper atmosphere of Venus, *Geophys. Res. Lett.*, 7, 106.
- [47] Keller, C. N., Cravens, T. E., & Gan, L., 1992. A model of the ionosphere of Titan, *J. Geophys. Res.*, 97, 12117.
- [48] Lammer, H., & Bauer, S. J., 1993. Atmospheric mass loss from Titan by sputtering, *Planet. Space Sci.*, 41, 657, doi:10.1016/0032-0633(93)90049-8.
- [49] Lammer, H., Stumptner, W., & Bauer, S. J., 1998. Dynamic escape of H from Titan as consequence of sputtering induced heating, *Planet. Space Sci.*, 46, 1207, doi:10.1016/S0032-0633(98)00050-6.

- [50] Lara, L. M., Lellouch, E., Lòpez-Moreno, J. J., & Rodrigo, R., 1996. Vertical distribution of Titan's atmospheric neutral constituents, *J. Geophys. Res.*, 101, 23261, doi:10.1029/96JE02036.
- [51] Lara, L. M., Banaszkiewicz, M., Rodrigo, R., & Lòpez-Moreno, J. J., 2002. The CH₄ density in the upper atmosphere of Titan, *Icarus*, 158, 191, doi:10.1006/icar.2002.6861.
- [52] Lavvas, P. P., Coustenis, A., & Vardavas, I. M., 2008a. Coupling photochemistry with haze formation in Titans atmosphere, Part I: Model description, *Planet. Space Sci.*, 56, 27, doi:10.1016/j.pss.2007.05.026.
- [53] Lavvas, P. P., Coustenis, A., & Vardavas, I. M., 2008b. Coupling photochemistry with haze formation in Titans atmosphere, Part II: Results and validation with Cassini/Huygens data, *Planet. Space Sci.*, 56, 67, doi:10.1016/j.pss.2007.05.027.
- [54] Lebonnois, S., Bakes, E.L.O., & McKay, C.P., 2003. Atomic and molecular hydrogen budget in Titan's atmosphere, *Icarus*, 161, 474, doi:10.1016/S0019-1035(02)00039-8.
- [55] Lellouch, E., Hunten, D. M., Kockarts, G., & Coustenis, A., 1990. Titan's thermosphere profile, *Icarus*, 83, 308, doi:10.1016/0019-1035(90)90070-P.
- [56] Lunine, J. I., Yung, Y. L., & Ralph, D. L., 1999. On the volatile inventory of Titan from isotopic abundances in nitrogen and methane, *Planet. Space Sci.*, 47, 1291, doi:10.1016/S0032-0633(99)00052-5.
- [57] Mason, E. A., & Marrero, T. R., 1970. The diffusion of atoms and molecules. In: Bates, D.R., Esterman, I. (Eds.), *Advances in Atomic and Molecular Physics*, Academic Press, San Diego, CA, pp. 155.
- [58] McClure, G. W., 1966. Electron transfer in proton-hydrogen-atom collisions: 2-117 keV. *Phys. Rev.*, 148, 47.
- [59] McDonough, T. R., & Brice, N. M., 1973. New Kind of Ring Around Saturn, *Nature*, 242, 513.
- [60] Michael, M., Johnson, R. E., Leblanc, F., Liu, M., Luhmann, J. G., & Schematovich, V. I., 2005. Ejection of nitrogen from Titan's atmosphere by magnetospheric ions and pick-up ions, *Icarus*, 175, 263, doi:10.1016/j.icarus.2004.11.004.
- [61] Michael, M., & Johnson, R. E., 2005. Energy deposition of pickup ions and heating of Titan's atmosphere, *Planet. Space Sci.*, 53, 1510, doi:10.1016/j.pss.2005.08.001.

- [62] Molina-Cuberos, G. J., Schwingenschuh, K., Lòpez-Moreno, J. J., Rodrigo, R., Lara, L. M., & Anicich, V., 2002. Nitriles produced by ion chemistry in the lower ionosphere of Titan, *J. of Geophys. Res.*, 107, 5099, doi:10.1029/2000JE001480.
- [63] Mousis, O., Gautier, D., & Coustenis, A., 2002. The D/H ratio in methane in Titan: origin and history, *Icarus*, 159, 156, doi:10.1006/icar.2002.6930.
- [64] Müller-Wodarg, I. C. F., Yelle, R. V., Mendillo, M., Young, L. A., & Aylward, A. D., 2000. The thermosphere of Titan simulated by a global three-dimensional time-dependent model, *J. Geophys. Res.*, 105, 20833, doi:10.1029/2000JA000053.
- [65] Müller-Wodarg, I. C. F., & Yelle, R. V., 2002. The effect of dynamics on the composition of Titan's upper atmosphere, *Geophys. Res. Lett.*, 29, 54, doi:10.1029/2002GL016100.
- [66] Müller-Wodarg, I. C. F., Yelle, R. V., Mendillo, M. J., & Aylward, A. D., 2003. On the global distribution of neutral gases in Titan's upper atmosphere and its effect on the thermal structure, *J. Geophys. Res.*, 108, 1453, doi:10.1029/2003JA010054.
- [67] Müller-Wodarg, I. C. F., R. V. Yelle, Borggren, N., & Waite, J. H., Jr., 2006. Waves and horizontal structures in Titan's thermosphere, *J. Geophys. Res.*, 111, A12315, doi:10.1029/2006JA011961.
- [68] Müller-Wodarg, I. C. F., Yelle, R. V., Cui, J., & Waite, J. H., Jr., 2008. Horizontal structure and dynamics of Titan's thermosphere, *J. Geophys. Res.*, submitted.
- [69] Ness, N. F., Acuna, M. H., & Behannon, K. W., 1982. The induced magnetosphere of Titan, *J. Geophys. Res.*, 87, 1369.
- [70] Niemann, H. B., Atreya, S. K., Bauer, S. J., Carignan, G. R., Demick, J. E., Frost, R. L., Gautier, D., Haberman, J. A., Harpold, D. N., Hunten, D. M., Israel, G., Lunine, J. I., Kasprzak, W. T., Owen, T. C., Paulkovich, M., Raulin, F., Raaen, E., & Way, S. H., 2005. The abundances of constituents of Titan's atmosphere from the GCMS instrument on the Huygens probe, *Nature*, 438, 779, doi:10.1038/nature04122.
- [71] Nutt, W. L., McCullough, R. W., & Gilbody, H. B., 1979. Electron capture by 04-13 keV C^+ , N^+ and O^+ ions in H and H_2 , *J. Phys. B: Atom. Molec. Phys.*, 12, L157.
- [72] Öpik, E. J., & Singer, S. F., 1961. A study of hydrogen diffusion in the earth's upper atmosphere near the critical level, *Phys. Fluids*, 4, 221.

- [73] Press, W. H., Teukolsky, S. A., Vetterling, W. T., & Flannery, B. P., 1992. *Numerical Recipes in C: The Art of Scientific Computing*, 2nd ed., Cambridge University Press, Cambridge, U.K., pp. 681-688.
- [74] Richardson, J. D., & Sittler, E. C., Jr., 1990. A plasma density model for Saturn based on Voyager observations, *J. Geophys. Res.*, 95, 12019.
- [75] Richardson, J. D., 1995. An extended plasma model for Saturn, *Geophys. Res. Lett.*, 22, 1177.
- [76] Rishbeth, H., Yelle, R. V., & Mendillo, M., 2000. Dynamics of Titan's thermosphere, *Planet. Space Sci.*, 48, 51, doi:10.1016/S0032-0633(99)00076-8.
- [77] Rowley, R. L., Wilding, W. V., Oscarson, J. L., Yang, Y., 2003. *Physical and thermodynamic properties of pure chemicals: core edition plus supplements 113*. Taylor & Francis, New York.
- [78] Schunk, R. W., & Nagy, A. F., 2000. Ionospheres: physics, plasma physics, and chemistry. In: Dressler, A.J., Houghton, J.T., Rycroft, M.J. (Eds.), *Cambridge Atmo. Space Sc. Ser.*, Cambridge University Press, Cambridge, U.K., pp. 104-147.
- [79] Shematovich, V. I., Tully, C., & Johnson, R. E., 2001. Suprathermal nitrogen atoms and molecules in Titan's corona, *Adv. Space Res.*, 27, 1875, doi:10.1016/S0273-1177(01)00268-X.
- [80] Shematovich, V. I., Johnson, R. E., Michael, M., & Luhmann, J. G., 2003. Nitrogen loss from Titan, *J. Geophys. Res.*, 108, 5086, doi:10.1029/2003JE002096.
- [81] Sittler, E. C., Jr., Ogilvie, K. W., Jr., & Scudder, J. D., 1983. Survey of low-energy plasma electrons in Saturn's magnetosphere: Voyagers 1 and 2, *J. Geophys. Res.*, 88, 8847.
- [82] Smith, G. R., Strobel, D. F., Broadfoot, A. L., Sandel, B. R., Shemansky, D. E., & Holberg, J. B., 1982. Titan's upper atmosphere - Composition and temperature from the EUV solar occultation results, *J. Geophys. Res.*, 87, 1351.
- [83] Smyth, W. H., 1981. Titan's hydrogen torus, *Astrophys. J.*, 246, 344.
- [84] Strobel, D. F., & Shemansky, D. E., 1982. EUV emission from Titan's upper atmosphere - Voyager 1 encounter, *J. Geophys. Res.*, 87, 1361.
- [85] Strobel, D. F., Summers, M., and Zhu, X., 1992. Titan's upper atmosphere: structure and ultraviolet emissions, *Icarus*, 100, 512, doi:10.1016/0019-1035(92)90114-M.

- [86] Strobel, D. F., 2007. Titan's hydrodynamically escaping atmosphere, *Icarus*, in press.
- [87] Tam, S. W. Y., Chang, T., & Pierrard, V., 2007. Kinetic modeling of the polar wind, *J. Atmos. Solar-Terrestrial Phys.*, 69, 1984.
- [88] Teanby, N. A., Irwin, P. G. J., de Kok, R., Nixon, C. A., Coustenis, A., Bézard, B., Calcutt, S. B., Bowles, N. E., Flasar, F. M., Fletcher, L., Howett, C., & Taylor, F. W., 2007a. Latitudinal variations of HCN, HC₃N, and C₂N₂ in Titan's stratosphere derived from Cassini CIRS data, *Icarus*, 181, 243, doi:10.1016/j.icarus.2005.11.008.
- [89] Teanby, N. A., Irwin, P. G. J., de Kok, R., Vinatier, S., Bézard, B., Nixon, C. A., Flasar, F. M., Calcutt, S. B., Bowles, N. E., Fletcher, L., Howett, C., & Taylor, F. W., 2007b. Vertical profiles of HCN, HC₂N, and C₂H₂ in Titan's atmosphere derived from Cassini/CIRS data, *Icarus*, 186, 364, doi:10.1016/j.icarus.2006.09.024.
- [90] Toubanc, D., Parisot, J. P., Brillet, J., Gautier, D., Raulin, F., & McKay, C. P., 1995. Photochemical modeling of Titan's atmosphere, *Icarus*, 113, 2, doi:10.1006/icar.1995.1002.
- [91] Vervack, R. J., Sandel, B. R., & Strobel, D. F., 2004. New perspectives on Titan's upper atmosphere from a reanalysis of the Voyager 1 UVS solar occultations, *Icarus*, 170, 91, doi:10.1016/j.icarus.2004.03.005.
- [92] Vuitton, V., Yelle, R. V., & Anicich, V. G., 2006. The Nitrogen Chemistry of Titan's Upper Atmosphere Revealed, *Astrophys. J.*, 647, 175, doi:10.1086/507467.
- [93] Vuitton, V., Yelle, R. V., & McEwan, M. J., 2007. Ion chemistry and N-containing molecules in Titan's upper atmosphere, *Icarus*, 191, 722, doi:10.1016/j.icarus.2007.06.023.
- [94] Vuitton, V., Yelle, R. V., & Cui, J., 2008. Formation and distribution of benzene on Titan, *J. Geophys. Res.*, in press.
- [95] Waite, J. H., Jr., Lewis, W. S., Kasprzak, W. T., Anicich, V. G., Block, B. P., Cravens, T. E., Fletcher, G. G., Ip, W.-H., Luhmann, J. G., McNutt, R. L., Niemann, H. B., Thorpe, R. L., Walter, E. M., & Yelle, R. V., 2004. The Cassini Ion and Neutral Mass Spectrometer (INMS) investigation, *Space Sci. Rev.*, 114, 113, doi:10.1007/s11214-004-1408-2.
- [96] Waite, J. H., Jr., Niemann, H., Yelle, R. V., Kasprzak, W. T., Cravens, T. E., Luhmann, J. G., McNutt, R. L., Ip, W.-H., Gell, D., De La Haye, V., Muller-Wordag, I. C. F., Magee, B., Borggren, N., Ledvina, S., Fletcher, G., Walter, E., Miller, R., Scherer, S., Thorpe, R., Xu, J., Block, B., & Arnett, K., 2005. Ion

- Neutral Mass Spectrometer results from the first flyby of Titan, *Science*, 308, 982, doi:10.1126/science.1110652.
- [97] Wilson, E. H., & Atreya, S. K., 2004. Current state of modeling the photochemistry of Titan's mutually dependent atmosphere and ionosphere, *J. Geophys. Res.*, 109, E06002, doi:10.1029/2003JE002181.
- [98] Woods, T. N., Rottman, G. J., Bailey, S. M., Solomon, S. C., & Worden, J. R., 1998. Solar Extreme Ultraviolet Irradiance Measurements during solar cycle 22, *Sol. Phys.*, 177, 133.
- [99] Yan, M., Sadeghpour, H. R., & Dalgarno, A., 1998. Photoionization cross sections of He and H₂, *Astrophys. J.*, 496, 1044.
- [100] Yelle, R. V., 1991. Non-LTE models of Titan's upper atmosphere, *Astrophys. J.*, 383, 380, doi:10.1086/170796.
- [101] Yelle, R. V., Borggren, N., De La Haye, V., Kasprzak, W. T., Niemann, H. B., Müller-Wodarg, I. C. F., & Waite, J. H., Jr., 2006. The vertical structure of Titan's upper atmosphere from Cassini Ion Neutral Mass Spectrometer measurements, *Icarus*, 182, 567, doi:10.1016/j.icarus.2005.10.029.
- [102] Yelle, R. V., Cui, J., Müller-Wodarg, I. C. F., 2008. Eddy diffusion and methane escape from Titan's atmosphere, *J. Geophys. Res.*, in press.
- [103] Yung, Y. L., Allen, M., & Pinto, J. P., 1984. Photochemistry of the atmosphere of Titan: Comparison between model and observations, *Astrophys. J. Suppl.*, 55, 465, doi:10.1086/190963.